Optimisation of transition metal dichalcogenide devices for measurement of spin-Hall voltages generated by optical spin orientation

Submitted for the degree of Masters by Research in Physics

Kyle Conder

January 2018

Declaration

Submitted by Kyle Conder, to the University of Exeter as a thesis for the degree of Masters by Research in Physics, January 2018.

This thesis is available for Library use on the understanding that it is copyright material and that no quotation from the thesis may be published without proper acknowledgement.

I certify that all material in this thesis which is not my own work has been identified and that no material has previously been submitted and approved for the award of a degree by this or any other University.

(Signature) .....

Abstract

Here we propose a design to optimise measurement of the transverse spin voltage resulting from the spin Hall effect (SHE) generated by shining circularly polarised light on a transition metal dichalcogenide (TMD) monolayer. There is currently a lot of interest in trying to create ohmic contacts to single layer TMDs due to the inherent Schottky barriers present at the metal to semiconductor interface, but the more successful methods either cover the entire flake or rely on a temporary doping with a low half-life. We propose using graphene as an intermediary contact with top gates only over the contacted regions leaving a central area of the TMD flake exposed so that the laser can reach it unimpeded. To maximise the SHE, the strength of the spin-orbit coupling of the atmospherically-stable TMDs have been reviewed. Armed with this information, and given that WSe_2 is an intrinsically p-type TMD, it was found to be the best candidate for investigating the SHE in such two-dimensional materials.

We have successfully both exfoliated and used Raman spectroscopy to characterise graphene and TMD flakes, using photoluminescence (PL) spectroscopy for the characterisation of the latter as well: whereas Raman spectroscopy has proven to be very effective in determining the layer number of the graphene and WSe_2 flakes, in the case of MoS_2, PL spectra can be more definitive in distinguishing monolayer from multilayer flakes. We unexpectedly, as WSe_2 is thought to be atmospherically stable, observed a change in the visibility of WSe_2 over a matter of four weeks, even when stored in a vacuum. The corresponding PL spectrum was also found to be heavily suppressed. Here we also report out attempts at stacking graphene onto TMD flakes to produce ohmic contacts.

Acknowledgements

There are a lot of people I would like to thank for all of their support and help during my Master's by Research. Firstly, my supervisors Dr. Annette Plaut and Prof. Saverio Russo at the University of Exeter. Annette was incredibly engaging as a supervisor and we had weekly meetings when we discussed progress had been made over the week and set goals for the upcoming one. Saverio was very approachable and always provided answers very quickly when I've asked. Mark Heath was a brilliant clean room technician who was very knowledgeable about the exfoliation of graphene and a great teacher when it came to the operation of the reactive ion etcher, the scanning electron microscope and the rest of the clean room equipment. I would also like to say thank you to Alan Usher and Jens Martin who always had a good insight into the physics of my work and guided me throughout these years.

I would like to thank the students of the university that have provided friendship and good discussions about physics and otherwise. In particular, I would like to thank Gregor McQuade, Tobias Octon, Freddie Withers and Thomas Collier. Tobias built the first stacking station in the physics building and was very happy to exchange ideas about mechanical exfoliation. Freddie has provided an incredible level of expertise in both stacking and exfoliating flakes whilst also having a great knowledge on transition metal dichalcogenides. Gregor was a fantastic colleague who was great to talk to about physics and I greatly enjoyed sharing our appreciation of gaming and movies.

Finally, I would like to express my gratitude to my girlfriend Sophie and my mother Karen, who truly made this possible. Without her I would not have made it to University, let alone a Master's degree.

Kyle Conder, January 2nd, 2018, Exeter

List of Figures

List of Tables

List of symbols and constants

$\boldsymbol{a_n}$ Lattice vectors of graphene

A Interatomic distance

$\boldsymbol{\delta_n}$ Nearest-neighbour vectors

$\boldsymbol{b_n}$ Reciprocal lattice vectors

ϕ_n Bloch wave functions

N_c Number of atoms in lattice

$\boldsymbol{R_n}$ Position of other atoms in the lattice

$\mathbf{r}$ Position of atom at origin

$\mathbf{k}$ Quasi-momentum of the electron

$\mathbf{K(')}$

Dirac points

$a_{1(2)n}$

Annihilation (creation) operators of electrons of n spin on the A sublattice

$b_{1(n)n}$

Annihilation (creation) operators of electrons of n spin on the B sublattice

t Nearest neighbour hopping parameter

v_F Fermi velocity

τ Valley index

σ_i Pauli matrices

$\boldsymbol{\mu_s}$ Magnetic dipole moment of an electron

μ_0 permeability of free space

$\mathbf{c}$ Speed of light in a vacuum

g gyromagnetic factor

e Charge of an elecron

$\boldsymbol{s}$ Spin angular momentum

m Mass of an electron

$\mathbf{p}$ Momentum

$\mathbf{B}$ Magnetic field

$\mathbf{E}$ Electric field

$\mathbf{F}$ Force

$e^e(h)_s(v)$

Spin (valley) Hall conductivities for electrons (holes)

λ Half spin-splitting of the valence bands

μ Fermi-level measured from the conduction band minimum

Δ Band gap

Contents

Chapter 1

Introduction

Although graphene has been studied theoretically since 1946 [1], it was only in 2004 that the first monolayer samples of graphene were experimentally isolated [2]. Due to its unique properties (discussed below) and single atomic thickness, graphene has been heavily investigated since its discovery [3].

Some of the most impressive properties of graphene are mechanical: The breaking strength of graphene has been shown to be 42 Nm^{-1} which corresponds to a bulk value of 130 GPa [4], compared to the breaking strength of steel which ranges between 450 and 1970 MPa [5]. This world-breaking strength comes combined with a high level of flexibility [6].

Beyond these mechanical properties, the electronic properties have been the main research interest: the valance and conduction bands cross at points in reciprocal space known as Dirac (K and K') points making it a gapless semiconductor [6]. Near these points the energy bands have a linear dispersion [6] such that the charge carriers behave like relativistic particles with a velocity of around $c/300$ (with c being the speed of light) [7].

Despite the fascinating properties of graphene, the fact that it does not have an inherent band gap means that it is not a suitable replacement for silicon in today's electronic devices. Two-dimensional (2D) materials that do have a band gap are the transition metal dichalcogenides (TMDs). TMDs are another class of layered mate-

rials that, like graphite, the bulk material consists of single layers held together by Van der Waals forces [8], can be mechanically cleaved to produce monolayers. The most commonly studied TMDs, when monolayers, are direct band gap semiconductors, which means they are of great interest for optoelectronic devices [8]. At cryogenic temperatures, the electron mobility of suspended graphene however has reached 230 000 $cm^2V^{-1}s^{-1}$ [9] which is much higher than that of TMDs which experimentally have only shown mobilities under 1000 cm^2V^{-1} [10]. It seems like the applicability of all of the TMDs and graphene will cover different niches.

The well-known Moore's law [11] means the speed and size of charge-based processors are ultimately limited, as the minimum number of electrons required to turn on a transistor cannot be reduced below one. By exploiting another property of charge carriers known as spin, a further degree of freedom can be utilised in devices [12]. The field that exploits the spin of the charge carriers is known as spintronics. Due to the large size of the transition metal atom and that TMDs have broken crystal inversion symmetry [13] their resulting spin-orbit coupling (SOC) makes them good candidates for spintronic devices [13]. Graphene, on the other hand, is insignificant due to the inversion symmetry of its atomic lattice and the smallness of carbon atoms themselves [14].

Spintronics could be one way of achieving quantum computing in the future overcoming the speed and size limitations of conventional electronic computers. One of the main advantages of using spintronic-based devices is that less energy is required to manipulate the spin of a particle compared to that required to manipulate its charge [15].

There are many different spin effects currently being investigated such as the circular photogalvanic effect [16], the anomalous Hall effect (AHE) [17] and a photoinduced anomalous Hall effect [18]. The investigations described in this thesis are aimed towards optimising TMDs for measuring the spin Hall effect (SHE) [19]. Previous similar experiments on TMDs, were either limited to imaging the spin distribution in a TMD sample [20] and/or where they did extract a voltage out of the device the results were attributed to the valley Hall effect (VHE) rather than the SHE [21]. Contacting has

been a big challenge in investigations of TMDs, as Schottky barriers have been present in nearly all contacts [22]. This investigation proposes a method of creating ohmic contacts to gated TMDs without the need to completely cover the TMD flake with a top gate.

While the investigations described here only had enough time to generate a marginal contribution to knowledge, this thesis demonstrates working at the current limits of understanding in the research field, as required for a Masters by Research degree. Chapter 2 explains the background physics and research into TMDs and the SHE, both theoretical and experimental, and finishes with a review of the progress made up to the present in creating ohmic contacts to TMD flakes. Chapter 3 contains the experimental details of the equipment and methodology used for exfoliation, characterisation and fabrication of monolayer graphene and TMD devices. Chapter 4 relates and discusses the results obtained here and at the end of the chapter proposes a contact design for future investigations. The final chapter of this thesis summarises the results and suggests proposals for future work.

Chapter 2

Background

2.1 Introduction

In 2004 monolayer graphene was isolated for the first time [2]. The hexagonal two-dimensional (2D) atomic structure of monolayer graphene can be stacked one monolayer on top of another to form graphite. The atomic structure of transition metal dichalcogenides (TMDs) on the other hand is also hexagonal but follows a X-M-X format, with X being a chalcogen (e.g. sulphur or selenium) and M the transition metal [8]. The key difference between monolayer graphene and a monolayer of a TMD is that in a monolayer of a TMD there is a trilayer of atoms arranged such that the metal layer lies between the two chalcogen layers.

This chapter discusses the background physics and previous research on such 2D materials relevant to our experiments: Firstly, the physics of graphene and that of the TMDs. Secondly, the spin Hall effect is described and how spin currents have been induced in non-magnetic semiconducting materials. With both the technique and material properties explained, these are then brought together to explain how the most appropriate TMD for our measurements was decided. Next, the difficulty in creating reliable ohmic contacts to TMD samples is discussed. Finally, this section describes the main non-destructive methods used to characterise such 2D materials, Raman spectroscopy and photoluminescence (PL) spectroscopy. This is followed by a

very brief review of strain in graphene.

2.2 Physics of graphene

The atomic lattice of graphene consists of a unit cell made up of two carbon atoms [23]. The atomic structure thus consists of two triangular atomic sublattices, commonly labelled as A and B, which are interwoven together [23]. As shown in Figure 2.1, each of the atoms of sublattice A (B) is surrounded by three atoms from the B (A) sublattice, this is known as a bipartite sublattice [23]. The nearest neighbour carbon atoms are therefore distributed evenly at 120° from each other at a distance of 0.142 nm [24].

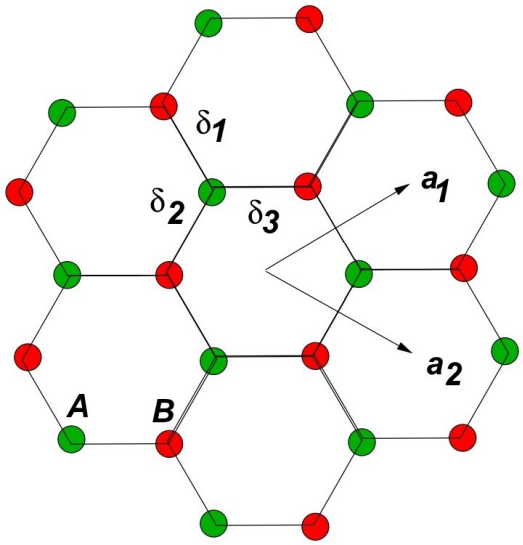

Figure 2.1: The two sublattices of monolayer graphene, green for A and red for B, showing the lattice vectors $\boldsymbol{a_1}$ and $\boldsymbol{a_2}$ and the nearest neighbour vectors ($\boldsymbol{\delta_{1,2,3}}$) [23].

The lattice vectors of monolayer graphene are given by [25]

$$\boldsymbol{a_1} = \frac{A}{2}(3, \sqrt{3}), \tag{2.1}$$

$$\boldsymbol{a_2} = \frac{A}{2}(3, -\sqrt{3}), \tag{2.2}$$

with A being the interatomic distance. The nearest-neighbour vectors for monolayer graphene are given by [25]

$$\boldsymbol{\delta_1} = \frac{A}{2}(1, \sqrt{3}), \tag{2.3}$$

$$\boldsymbol{\delta_2} = \frac{A}{2}(1, -\sqrt{3}), \tag{2.4}$$

$$\boldsymbol{\delta_3} = A(-1, 0). \tag{2.5}$$

There are three electronic orbitals in which the six electrons of carbon are accommodated – $1s^2$, $2s^2$, $2p^2$ [24]. The 2s and 2p electrons form three hybridized sp^2 covalent bonds between the adjacent carbon atoms resulting in the hexagonal structure of graphene which explains its mechanical strength. The remaining p_z electronic orbitals form π bonds parallel to the plane of this hexagonal ring of carbon atoms [23]. Only electrons in this p_z orbital contribute to the electrical conductivity of graphene.

The reciprocal lattice of graphene is shown in Figure 2.2 The reciprocal lattice vectors are given by [23]

$$\boldsymbol{b_1} = \frac{2\pi}{3A}(1, \sqrt{3}), \tag{2.6}$$

$$\boldsymbol{b_2} = \frac{2\pi}{3A}(1, -\sqrt{3}). \tag{2.7}$$

The first Brillouin zone of graphene is also hexagonal, the corners of which are known as Dirac points [24]. These Dirac points are of great interest as it is at these points that the maximum of the valence band and the minimum of the conduction band are located [23]. In fact, they touch at the Dirac points and in addition the energy dispersion of the electronic band structure around these points is linear [23].

By taking into account nearest and next-nearest neighbour hopping, Castro Neto *et al.* [23] demonstrated this linear dispersion relation in graphene near the Dirac points. They calculated the energy band structure of the electrons in graphene using the tight-binding approximation [26]. In the following, we will only take into account nearest neighbour hopping, with the transfer of electrons between sublattices having a hopping amplitude of t. Using an atomic orbital ($X_v(r)$) it is possible to calculate the interaction with other atoms in the lattice by using a suitable Bloch wave function. In this case

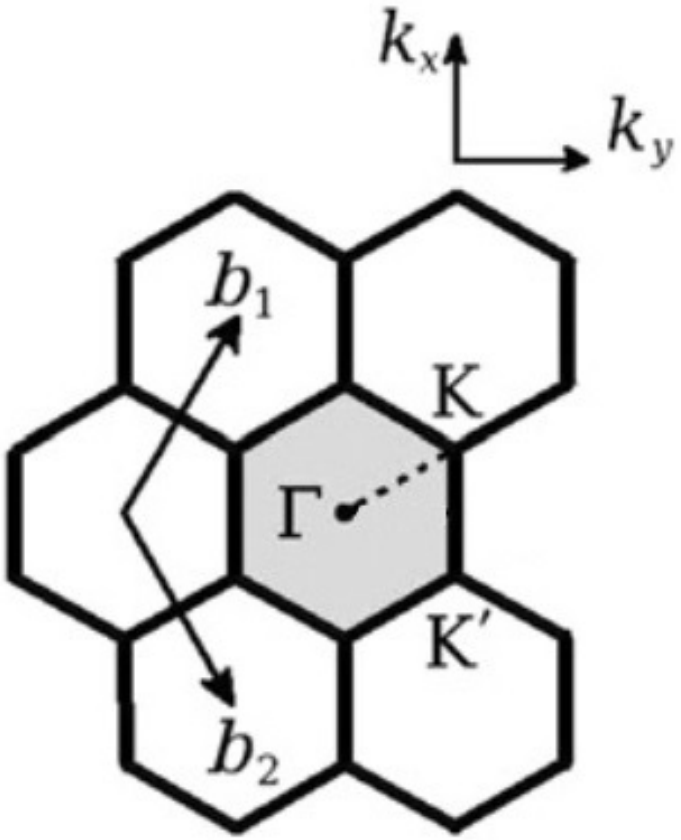

Figure 2.2: The reciprocal lattice of graphene, with the reciprocal lattice vectors ($\boldsymbol{b_{1,2}}$) and the high-symmetry points (Γ , K, K') indicated [24]

the Bloch wave function takes the form [27]

$$\phi_k(x) = \frac{1}{\sqrt{N_c}} \sum_{n=1}^{N_c} e^{i\boldsymbol{k}\cdot\boldsymbol{R_n}} X_v(\boldsymbol{r} - \boldsymbol{R_n}), \tag{2.8}$$

where N_c is the number of atoms in the lattice, $\boldsymbol{R_n}$ is the position of the other atoms in the lattice and $\boldsymbol{r}$ is the position of the atom located at the origin whilst $\boldsymbol{k}$ is the quasi-momentum of the electron. Due to Graphene being a bipartite lattice, the electons of the sublattices A and B have inequivalent wavefunctions as the environment of each of them is different. Each atom in sublattice A has two atoms on the left and one one the right whilst the atoms in sublattice B have one atom on the left and two on the right (See Figure 2.1). Assuming that the Fermi energy of the undoped graphene lies at the Dirac points [23], by expanding the Fourier sum of eqn. 2.8 the wavefunctions can be

calculated. The resulting $\phi_{A,B}$ wavefunctions are then given by [23]:

$$\phi_A = exp(-i\boldsymbol{K}\cdot\boldsymbol{R_n})a_{1,n} + exp(-i\boldsymbol{K'}\cdot\boldsymbol{R_n})a_{2,n}, \tag{2.9}$$

$$\phi_B = exp(-i\boldsymbol{K}\cdot\boldsymbol{R_n})b_{1,n} + exp(-i\boldsymbol{K'}\cdot\boldsymbol{R_n})b_{2,n}, \tag{2.10}$$

where K and K' are the Dirac points shown in Figure 2.2 and $a_{1(2),n}$ is the annihilation (creation) operator of electrons with spin n on the A sublattice, whilst $b_{1(2),n}$ denotes the same operator for electrons on the B sublattice. These two new wavefunctions are assumed to vary slowly over the unit cell [25]. The resulting Bloch wave function of the graphene lattice is then given by combining the Bloch functions of both of the sublattices[28]:

$$\psi = \phi_A + \lambda\phi_B, \tag{2.11}$$

with $\phi_{A,B}$ being the Bloch functions of the electron orbitals in their respective sublattices summed over all of the lattice points within that sublattice, taking the overlap of the p_z wavefunctions centred on different atoms to be zero [28]. The Hamiltonian for graphene including the nearest neighbour hopping takes the form of a 2×2 matrix [25]:

$$\hat{H}(\boldsymbol{k}) = \begin{pmatrix} 0 & tS(\boldsymbol{k}) \\ tS^*(\boldsymbol{k}) & 0 \end{pmatrix}, \tag{2.12}$$

where

$$S(\boldsymbol{k}) = 2exp\left(\frac{-ik_x a}{2}\right) cos\left(\frac{k_y a\sqrt{3}}{2}\right) + exp(-ik_x a) \tag{2.13}$$

and k_x and k_y are the quasi-momenta of the electron in the x and y directions respectively and a denotes the lattice constant of graphene. When this Hamiltonian operates on the wave function of eqn. 2.11 it results in the energy eigenvalue [25]

$$E(\boldsymbol{k}) = \pm t|S(\boldsymbol{k})| = \pm t\sqrt{3 + f(\boldsymbol{k})}, \tag{2.14}$$

where

$$f(\boldsymbol{k}) = 2cos(\sqrt{3}k_y a) + 4cos\left(\frac{\sqrt{3}k_y a}{2}\right) cos\left(\frac{3k_x a}{2}\right) \tag{2.15}$$

which can be calculated to be [29]

$$E(\boldsymbol{k}) = \pm t\sqrt{1 + 4cos\left(\frac{\sqrt{3}k_y a}{2}\right) cos\left(\frac{k_x a}{2}\right) + 4cos^2\left(\frac{k_x a}{2}\right)}. \tag{2.16}$$

This results in $S(\boldsymbol{K}) = S(\boldsymbol{K'}) = 0$, showing that there is a crossing of the bands at the Dirac points K and K' [29].

With knowledge of the nearest-neighbour hopping parameter ($t = -2.97\ eV$ [23]) and the lattice constant (a = 2.46 Å [30]), the Fermi velocity ($v = 3a|t|/2$ [23]) can be found $v_F = 1 \times 10^6\ ms^{-1}$ [23]. The Hamiltonian of eqn. 2.12 is the same as that of the Dirac equation for relativistic particles [25]. Thus, close to the Dirac points, the electrons behave like massless relativistic particles (Dirac fermions) having the linear energy dispersion, shown in Figure 2.3. The key difference created from taking into account the next-nearest neighbour hopping, is that the conduction band has a much higher maximum whilst the valence band minimum remains relatively consistent with that calculated from only the nearest neighbour approximation. The linear energy dispersion near the Dirac points is present in both approximations. Although no experimental results for the intrinsic case of graphene were found during this investigation, the electron energy dispersion around the Dirac points has been experimentally determined to indeed be linear for low doping, using angle-resolved photoemission spectroscopy [29].

It is relatively simple to extend this approach to bilayer and few-layer graphene [23]. In the case of bilayer graphene this results in two sets of parabolic bands [23]. One pair is given by $E_{k,\pm} \approx \pm v_F^2 k^2 / t_\perp$, where $t_\perp$ is the interlayer hopping amplitude, which again touch at the Dirac points, while the other pair have their closest approach at the Dirac points, but are separated in energy by $E = \pm t_\perp$ as shown in Figure 2.4 [23]. However, bilayer and few-layer graphene are beyond the scope of this thesis.

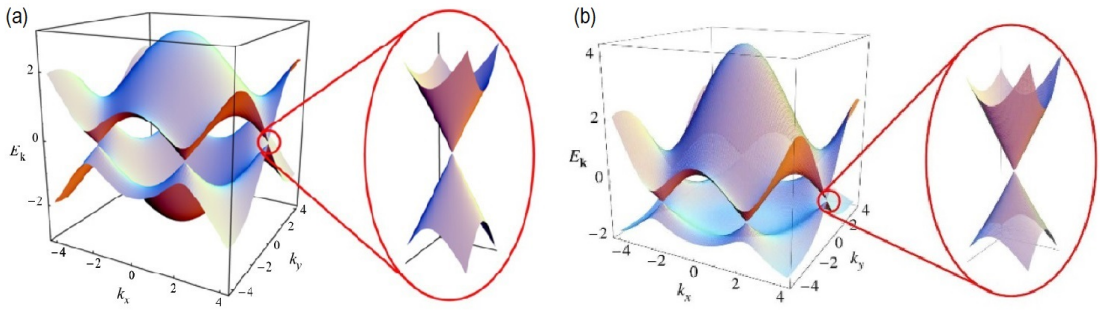

Figure 2.3: The dispersion relation of electrons in graphene across the first Brillouin zone: (a) using the nearest-neighbour approximation [31] whilst the (b) using next-nearest neighbour approximation [23]. Both include expanded views of the energy dispersion around the Dirac points.

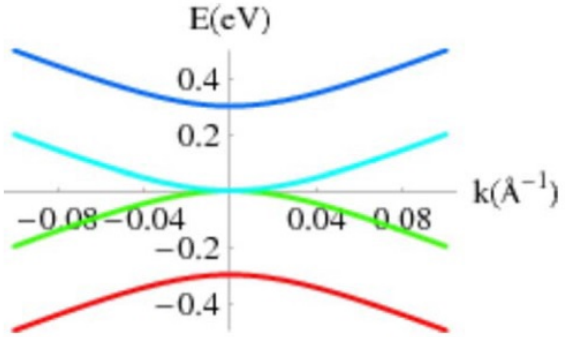

Figure 2.4: The band structure of bilayer graphene around a single Dirac point [23].

2.3 Physics of transition metal dichalcogenides

The atomic structure of monolayer molybdenum disulphide (MoS_2) and its unit cell are shown in Figure 2.5 and its first Brillouin zone in Figure 2.6. Here we will largely concentrate on MoS_2 as an example of a typical TMD. From the left side of Figure 2.5, the similarity between the hexagonal structures of graphene and the TMDs is evident, with the two types of atoms in TMDs appearing to form a similar structure as the two sublattices of graphene when viewed from above. The right side of Figure 2.5 shows the key difference between graphene and TMDs lattices, the chalcogens (sulphur) are offset above and below the transition metal (molybdenum), also there are twice the number of chalcogen atoms compared to the transition metal atoms. The partially filled d bands are the main contributors to the band structure around the Dirac points in MoS_2 [13]. One of the most obvious differences between the band structure of graphene and the

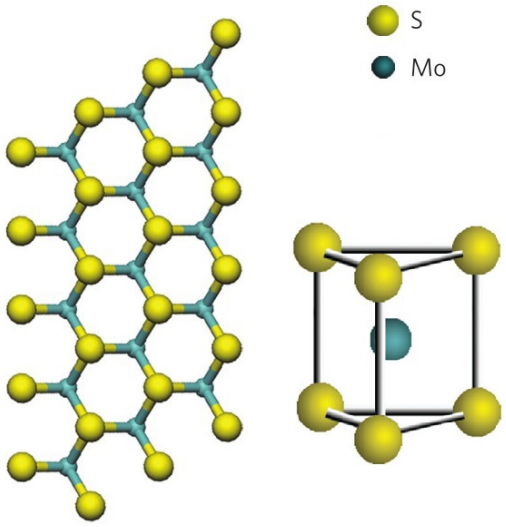

Figure 2.5: Left: A top view of the atomic structure of monolayer molybdenum disulphide. Right: A side view of its unit cell [32].

TMDs is that for the TMDs there is a bandgap at all wavenumbers [13]. The basis wave functions at the TMD band edges which are located at the K (K') points are [13]

$$|\phi_c\rangle = |d_{z^2}\rangle\,, \tag{2.17}$$

$$|\phi_v^\tau\rangle = \frac{1}{\sqrt{2}}(|d_{x^2-y^2}\rangle + i\tau\,|d_{xy}\rangle), \tag{2.18}$$

where the valley index is denoted by $\tau = \pm 1$ and the band which the wave function describes is denoted by the subscript c or v for conduction and valence bands, respectively. The spin-orbit coupling (SOC) of the d orbitals of the metal atoms is another major difference between these two 2D systems [13]. SOC is discussed in detail in Section 2.4. The SOC is the reason for the valence bands being spin split, as shown in Figure 2.6. While, in the first order of k, the Hamiltonian has the form [13]

$$\hat{H}_0 = at(\tau k_x \hat{\sigma}_x + k_y \hat{\sigma}_y) + \frac{\Delta}{2}\hat{\sigma}_z, \tag{2.19}$$

where Δ is the energy gap and a is the lattice constant of MoS_2 and $\hat{\sigma}_x$,$\hat{\sigma}_y$ and $\hat{\sigma}_z$ are the Pauli matrices [25]

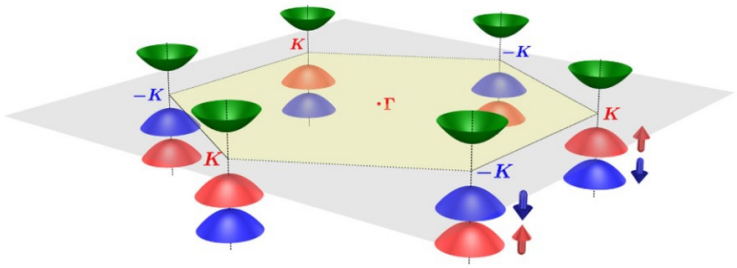

Figure 2.6: The first Brillouin zone (yellow) of MoS_2, showing the two spin-split valence bands (red and blue) and conduction bands (green) near the K and K' (denoted as $-K$) points [13].

$$\hat{\sigma}_x = \begin{pmatrix} 0 & 1 \\ 1 & 0 \end{pmatrix}, \tag{2.20}$$

$$\hat{\sigma}_y = \begin{pmatrix} 0 & -i \\ i & 0 \end{pmatrix} \tag{2.21}$$

$$\hat{\sigma}_z = \begin{pmatrix} 1 & 0 \\ 0 & -1 \end{pmatrix} \tag{2.22}$$

There are definite similarities between the Hamiltonians of graphene and the TMDs: trilayer graphene with a staggered sublattice potential across the layers can equally be described by the TMD Hamiltonian of eqn. 2.19 [13]. This is a result of the similar symmetry properties of these two types of 2D materials.

Most of the band structures of the TMDs are quite similar [33]. Generally, molybdenum and tungsten based TMDs are semiconducting [34]. The calculated band structures of bulk, monolayer and few-layer MoS_2 are shown Figure 2.7 [33]. As can be seen in Figure 2.7 the bandgap changes from indirect to direct when going from bilayer to monolayer.

Wang [34] attributes this change to a direct bandgap for monolayer TMDs to quantum confinement and the changing hybridization between p_z orbitals of the sulphur atoms and the d orbitals of the molybdenum atoms. As Figure 2.7 shows the electronic states near the K points are relatively unchanged as the layer number is reduced [33].

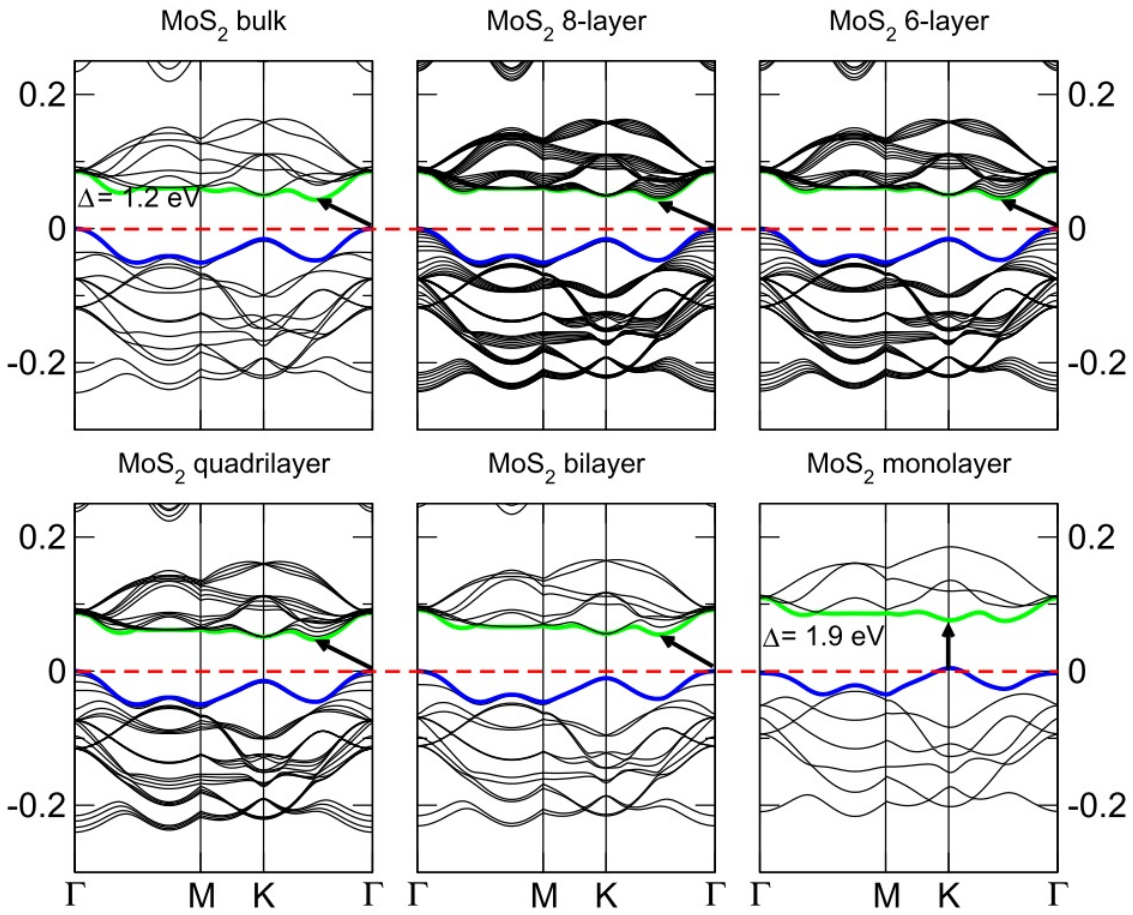

Figure 2.7: Calculated band structures of bulk and few- to monolayer MoS_2 flakes. The arrows highlight the band gap [33].

This is in contrast to the band gap at the Γ point which is larger for monolayer than in the bulk. It is this change at the Γ point which is responsible for the change in band gap from indirect to direct in monolayer TMDs. This indirect to direct transition has been experimentally confirmed [35].

2.4 Spin-orbit coupling

The d_{z^2} orbitals of the TMD conduction band are nearly spin degenerate at the Dirac points compared to the spin-split energy levels of the TMD valence band edge [13] as can be seen in Figure 2.8. SOC is the cause of this large spin-splitting at the valence band edge. SOC is when an electron changes both its angular momentum and its spin at the same time [25]. This mixing of the spin and orbital motion of the electron is a

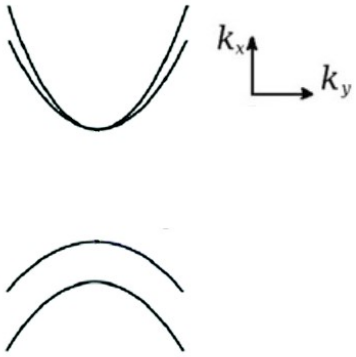

Figure 2.8: Conduction band minimum and valence band maximum at the Dirac point in TMDs

phenomenon which arises from the quantum electrodynamic Dirac equation. It takes the form of [36]

$$\Delta E_{SO} = -\boldsymbol{\mu}_s \cdot \boldsymbol{B} = \frac{e}{m^2 c^2} \boldsymbol{s} \cdot (\boldsymbol{E} \times \boldsymbol{p}), \tag{2.23}$$

where

$$\boldsymbol{\mu}_s = \mu_0 \frac{ge}{2m} \boldsymbol{s} \cdot (\boldsymbol{E} \times \boldsymbol{p}), \tag{2.24}$$

and

$$\boldsymbol{B} = \boldsymbol{v} \times \frac{\boldsymbol{E}}{c^2}, \tag{2.25}$$

Therefore

$$\Delta E_{SO} = \frac{-ge\mu_0}{4m^2} \boldsymbol{s} \cdot (\boldsymbol{E} \times \boldsymbol{p}), \tag{2.26}$$

where $\boldsymbol{\mu}_s$ is the magnetic dipole moment of an electron, $\boldsymbol{s}$ is the spin angular momentum and g its gyromagnetic factor ($g \approx 2$) of an electron. $\boldsymbol{B}$ is the effective magnetic field of the nuclei due to the electric field $\boldsymbol{E}$ of the nuclei, $\boldsymbol{p}$ the momentum of an electron, e the charge of an electron, the mass of an electron m, c the speed of light in a vacuum, $\boldsymbol{v}$ the velocity of an electron and the μ_0 the permeability of free space and Eqn. 2.26 demonstrates the interaction of the spin of the electron with the magnetic field that is experienced by the moving electron. Such spin-orbital mixing is large for heavy ions where the velocity of the electron is higher [23]. As carbon is a light atom the SOC is expected to be weak in graphene [23]. From the known SOC for carbon it is possible

to deduce the magnitude of the SOC in graphene: the intrinsic SOC of graphene has been calculated to be in the range of 0.01 - 0.02 K [23]. This is a very small quantity when compared to other energy scales in the electronic system of graphene [23].

In contrast, due to the size of the transition metal atom in TMDs, combined with their crystal inversion asymmetry, TMDs exhibit strong SOC [13]. The various contributions to the SOC have been denoted as Dresselhaus and Rashba: the intrinsic contribution of broken inversion symmetry of the lattice to the SOC is called the Dresselhaus term [37]. Other contributions to the SOC which are of extrinsic origin, such as fields being applied, are known as Rashba contributions [38].

2.5 Discovery of new Hall effects

The classical Hall effect [39] occurs when a current is passed through a conductor in a perpendicular magnetic field. Under such conditions the charge carriers experience a Lorentz force given by [27]

$$\boldsymbol{F} = e(\boldsymbol{E} + \boldsymbol{v} \times \boldsymbol{B}) \tag{2.27}$$

However, both spin up and spin down charge carriers experience the same Lorentz force and are thus pushed in the same direction. In the recently discovered spin Hall effect (SHE) [40, 42] on the other hand no magnetic field is involved, instead the SOC causes charge carriers with opposite spin to experience a force which pushes these carriers to opposite sides of the sample through which a current is being passed [40]. This force arises from the effective magnetic field of eqn. 2.26. Thus, an equal number of spin up charge carriers end up on one side of the sample to spin down charge carriers on the opposite side meaning that there is no potential difference between the two sides and so electrical measurements of this effect are not possible. Figure 2.9 is a Kerr microscopy image of bulk n-type GaAs which clearly shows the SHE.

In the case of ferromagnets however where there is an imbalance in the number of charge carriers of each spin, it is possible for a potential difference across the sample to

be measured [40]. This is known as the anomalous Hall effect [41]. This is known as the AHE which was first measured by Hall himself in 1880 [41].

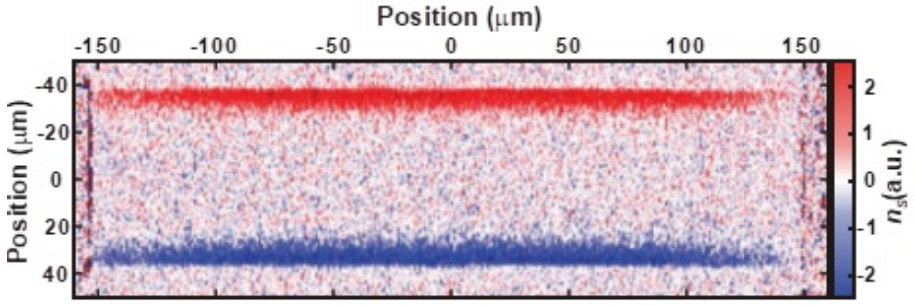

Figure 2.9: Kerr microscopy of bulk n-type GaAs, with red and blue denoting charge carriers with opposite spin [42].

In the case of non-ferromagnetic semiconductors, a spin imbalance can be created by using circularly polarised light to illuminate the sample. Although an extrinsic spin-Hall voltage caused by spin-dependent scattering by impurities had been measured [42], in 2015 Vasyukov *et al.* reported the first measurements of an intrinsic spin-Hall voltage in GaAs quantum wells [18]. Vasyukov *et al.* found that the resultant transverse spin voltage had a linear dependence on the mobility (Figure 2.10), which indicates that the spin-Hall effect which generated that transverse spin voltage was intrinsic and thus due to Dresselhaus contributions to the SOC rather than extrinsic, i.e. caused by spin dependent scattering at defects. The experimental set up planned in the work reported in this thesis is based on that of Vasyukov *et al.*.

2.6 Spin and valley Hall effects in two dimensional materials

Charge carriers in 2D materials with a honeycomb atomic structure such as graphene and group VI TMDs, possess an extra valley degree of freedom in addition to charge and spin [23, 21]. This valley degree of freedom in TMDs results in the different valleys (K and K') experiencing, as a result of broken inversion symmetry in the crystal structure of

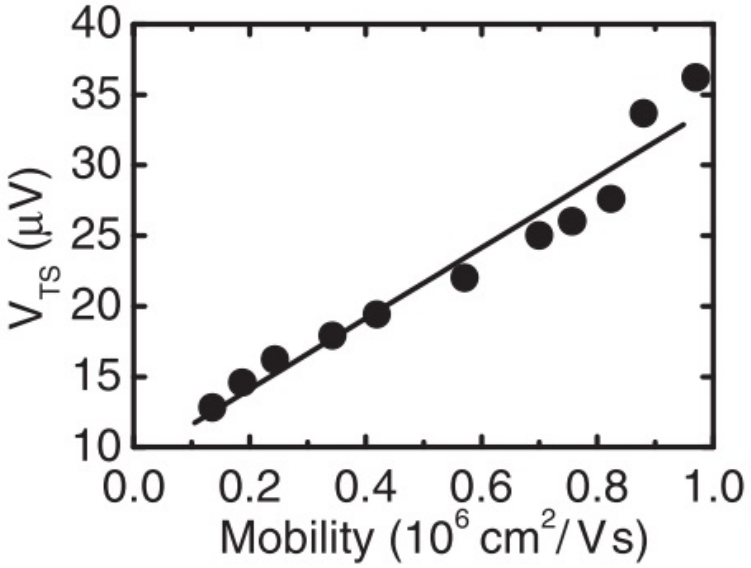

Figure 2.10: Plot of the resultant transverse voltage (V_{TS}) vs the charge carrier mobility, in a sample of p-type GaAs [18]

TMDs, the same effective magnetic fields but with opposite sign [21]. This gives rise to the valley Hall effect (VHE) which is caused by the orbital motion of the charge carriers being coupled to the valley degree of freedom [21]. This is analogous to the SHE where the orbital motion of the charge carriers is coupled instead to the charge carrier spin [21]. Dyakonov and Perel were the first theorists who proposed the SHE [40], where, in the presence of an electron experiences an effective magnetic field which is directionally dependent on its spin leading to a transverse spin current but no charge current [43]. Thus Mak *et al.* [21], on passing a current through a heavily n-type MoS_2 monolayer under illumination with circularly-polarised light, measured at transverse voltage which they identified to be due to the VHE [21]. Their experimental set up [21] was similar in design to that of Vasyukov *et al.* [18] and is shown in Figure 2.11. In Figure 2.11a the VHE is shown schematically where the photoexcited electron and hole are pushed to opposite sides of the sample due to the presence of a net valley polarisation. The Hall voltage (V_H) was measured between contacts A and B in Figure 2.11b whilst a bias voltage (V_x) was applied which drove a current perpendicularly (I_x). This enabled the calculation of the the Hall resistance ($R_H = V_H/I_x$). The laser photon energy used to photoexcite the charge carriers was centred at 1.9 eV in order to be reseonant with

an excitonic transition.

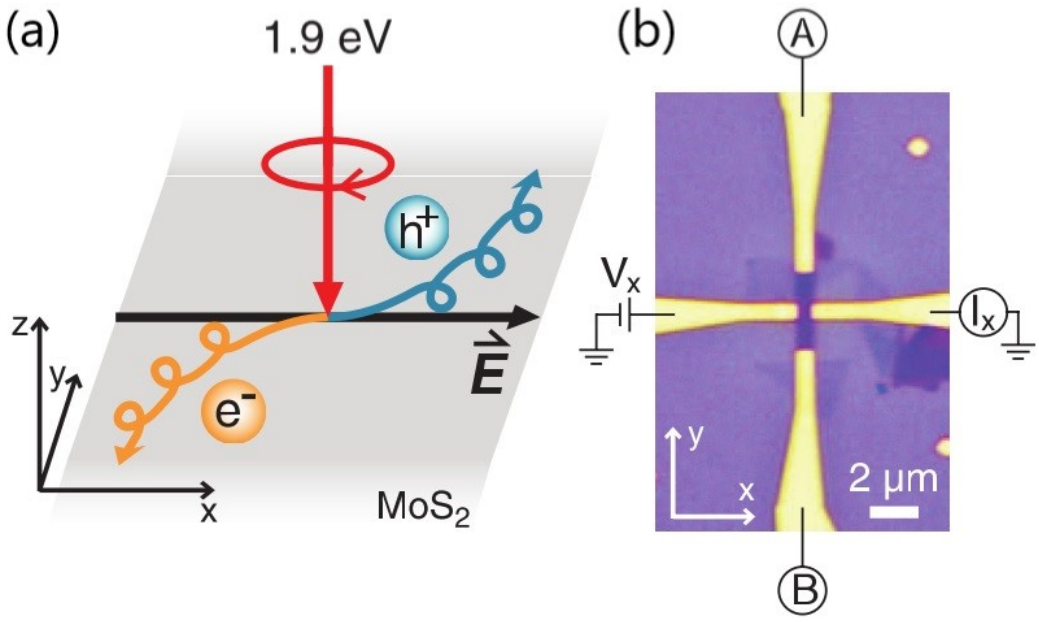

Figure 2.11: Left: Schematic of the photoinduced VHE in MoS_2 using circularly-polarised light of photon energy 1.9 eV. Right: An optical image of the MoS_2 Hall bar used by Mak *et al.* A and B denote the contacts across which the transverse voltage was measured [21].

The circular polarisation dependence of R_H is demonstrated in Figure 2.12. The angle of incidence of the linearly polarised light to the fast axis of the modulator is denoted by θ. The sinusoidal dependence of R_H with respect to θ is exactly what one would expect for the VHE as under quarter wave modulation, the circular polarisation of the resultant light is maximised when θ is 45° [21]. Another key point of Mak *et al.*'s work [21] is that in bilayer samples the R_H is less than 10% of that measured in monolayer samples. This drop in R_H is claimed to be caused by the inversion symmetry being restored in bilayer samples [21].

It is noticeable that the results of Mak *et al.* [21] have not been follow by a flourishing of reports of similar results. The MoS_2 sample of Mak *et al.*'s work was extremely n-type which may have enabled the authors to create their claimed near ohmic contacts [21]. There has been a lot of research into how to contact to monolayer TMDs due to the almost inevitable presence of Schottky barriers causing difficulties when trying to

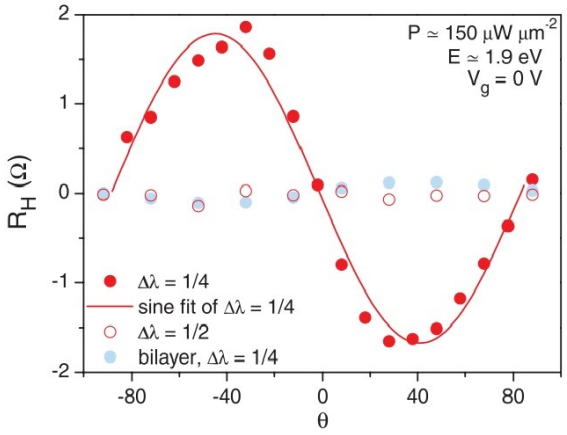

Figure 2.12: The anomalous Hall resistance of the monolayer device as a function of the incidence angle θ under quarter-wave ($\Delta\ \lambda = 1/4$, solid red circles) and half-wave ($\Delta\ \lambda = 1/2$, open red circles) modulations. Results for the bilayer device under quarter-wave modulation are also shown (blue circles) [21].

measure low voltages [22]. This could be why no other similar VHE results in TMDs have so far been published, whilst on the other hand there has been a lot of research reported on how to create better electrical contacts to the TMDs [22]. This will be discussed in more detail in Section 2.9.

More recently the VHE in bilayer MoS_2 has been shown to be gate voltage tuneable [20]. The inversion symmetry, which reduced the VHE in measured bilayer samples in Mak *et al.*'s work can be broken by applying an electric field perpendicular to the plane of the layers. Although in Lee *et al*'s work the lack of spin imbalance of the charge carriers, due to the laser exciting spin up (down) electrons in the top (bottom) layers, prevented a Hall voltage being measured, Kerr rotation microscopy was used instead [20].

The claim of Mak *et al.* that the VHE was the main contributor to their measured transverse voltage [21], agrees with the theoretical predictions of Xiao *et al.* [13]. Xiao *et al.* stated that the ratio of strength of the SHE and VHE is dependent on the doping of the TMD [13]. In the case of a negatively doped TMD, as in Mak *et al.*'s case of naturally n-type doped MoS_2, the magnitude of the VHE electron conductivity is given by [13]

$$\sigma_v^e = \frac{1}{\pi}\frac{\Delta}{\Delta^2 - \lambda^2}\mu, \tag{2.28}$$

where λ is half the spin-splitting of the valence bands, μ is the Fermi-level measured from the conduction band minimum and Δ is the band gap. At this same doping the SHE electron conductivity in a TMD is given by [13]

$$\sigma_s^e = \frac{1}{\pi}\frac{\lambda}{\Delta^2 - \lambda^2}\mu. \tag{2.29}$$

The relation between the SHE and VHE electron conductivities in such an n-type doped TMD can be thus expressed as [13]

$$\frac{\sigma_s^e}{\sigma_v^e} = \frac{\lambda}{\Delta}. \tag{2.30}$$

On the other hand, the maximum SHE contribution to the TMDs conductivity occurs when the Fermi level of the TMD lies between the spin split valence bands [13]. Then the SHE and VHE hole conductivities turn out to be equal, both being given by [13]

$$\sigma_s^h = \sigma_v^h = \frac{1}{\pi}\frac{\mu}{\Delta - \lambda}. \tag{2.31}$$

Thus a TMD most suitable for measuring the SHE, rather than the VHE, needs to be positively doped so that the Fermi level lies exactly between the spin-split valence bands at the K points. In the case of greater p-type doping, i.e. with the Fermi level deep in the valence band, the magnitude of the SHE hole conductivity in TMDs is the same as when the TMD is n-type; the only difference being a change in sign [44]. It thus is again smaller in magnitude than the VHE conductivity.

The valley Hall effect therefore tends to dominate over the SHE in TMDs. An indication of the strength of the SHE conductivity in TMDs is given by the size of the valence band splitting as this is directly related to the size of the SOC in the material [13]. Tungsten based TMDs such a WS_2 and WSe_2 have relatively large spin splittings in their valence band compared to molybdenum based TMDs – see Table 2.1 and thus could be good candidates for measuring the SHE in TMDs

2.7 Valley-spin locking in transition metal dichalcogenides

The interaction of the d orbitals in TMDs leads to the strong coupling of the spin and valley degrees of freedom [13]. The spin splittings of the valence and conduction bands of TMDs result in only certain optical transitions between the valence and conduction bands being optically active (bright), other transitions are spin-forbidden (dark), meaning that they cannot be excited via a single photon [45, 46]. For sulphur and selenium TMDs, the allowed transitions depend on whether the TMD is molybdenum or tungsten based [47]. In molybdenum TMDs the allowed (bright) transition from the upper spin-split valence band is to the lower spin-split conduction band, A-exciton; whilst from the lower spin-split valence band the bright transition is to the upper spin-split conduction band, B-exciton, as is shown in Figure 2.13. For tungsten based TMDs, the bright and dark exciton transitions are the opposite way around due to the splitting of conduction band being reversed [47]. Figure 2.13 shows the K_+ valley, it should be noted at the spins are reversed in the K_- valley [47].

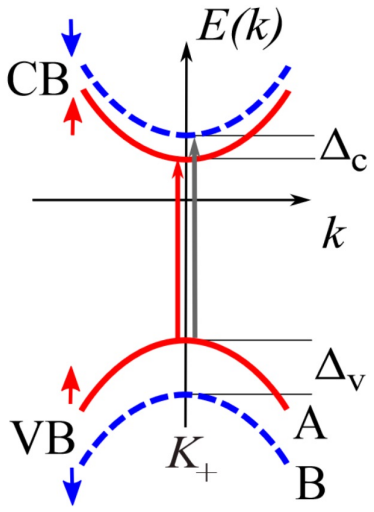

Figure 2.13: Single particle energy band diagram showing the bright and dark exciton transitions in monolayer molybdenum based TMDs at the K valley (denoted as K_+) with the $\Delta_{c(v)}$ denoting the spin splitting of the conduction (valence) bands, respectively [45].

In terms of reciprocal space, the two valleys are widely spaced meaning that scat-

tering between the valleys is highly suppressed, leading in general to a high valley polarisation [47]. Due to this valley-spin locking, valley polarisation hence plays a large role in the generation of transverse spin/valley voltages in TMDs because if the valley polarisation is too low then it is impossible to generate a spin imbalance. With the degree of valley polarisation of TMDs being dependent on the lowest energy exciton being either bright or dark, tungsten TMDs appear to be favourable as in tungsten TMDs the dark exciton has the lowest energy [47]: Only bright excitons can be photoexcited and then can be scattered either to the dark exciton state or the other valley. In tungsten TMDs, due to the dark exciton being the ground state, scattering to the dark exciton state is highly efficient compared to intervalley scattering leading to a build up of valley polarisation [47]. In MoS_2 and $MoSe_2$ on the other hand, the intervalley scattering is much more prominent leading to their valley polarisation being much lower [47].

2.8 Choice of transition metal dichalcogenides

TMD	Bandgap (eV)	Spin splitting at valence band (eV)	Ratio between spin splitting and bandgap
MoS_2	1.9 [35]	0.15 [13]	0.08
$MoSe_2$	1.63 [48]	0.18 [13]	0.11
WS_2	1.60 [13]	0.425 [13]	0.27
WSe_2	1.65 [49]	0.513 [13]	0.31

Table 2.1: The optical band gaps along with the valence band spin splitting for the atmospherically stable TMDs along with the ratios between the Bandgaps and the respective spin splittings of the valence bands

In Table 2.1 the ratios of the different TMDs are given. In WSe_2 the ratio between the valence band spin splitting and its band gap is one of the highest out of all the TMDs [48]. Thus WSe_2 is an excellent candidate for a SHE measurement as it therefore should have, from eqn. 2.30, one of the highest SHE hole conductivities of all the TMDs. Furthermore, as can be seen in Table 2.1 the tungsten TMDs have larger spin splittings in the valence bands than the molybdenum TMDs. This large spin splitting means

that it would be comparatively easier to tune the Fermi level to the desired position between the spin-split valence bands. To tune the Fermi level to lie between the spin-split valence bands, a naturally p-type TMD has an obvious advantage over a naturally n-type TMD as the Fermi level does not then need to be made to cross the band gap. WSe_2 happens to be the only stable naturally p-type TMD. Molybdenum diteleride and 2D black phosphurus are also meant to be naturally p-type but are unstable in ambient conditions [50]. The Fermi level itself would need to be adjusted via voltages being applied to gates. Although top gates are unsuitable for an experiment involving an optically induced spin imbalance, as a top gate would interfere with the optical excitation. Taking into account all the above considerations it seems clear that WSe_2 is the most appropriate TMD for a SHE measurement.

2.9 Contacting to the transition metal dichalcogenides

As discussed in Section 2.8, this work has deemed WSe_2 the most appropriate TMD for the SHE measurements. Thus here we will focus on progress towards creating ohmic contacts to WSe_2. Furthermore, due to WSe_2 being naturally p-type , we will concentrate on making p-type contacts to TMDs. Although there has been some work on n-type contacts to WSe_2, this is beyond the scope of this thesis [51].

Creating ohmic electrical contacts to 2D TMDs is still an ongoing challenge. When a metal contacts to a semiconductor there can be a potential barrier known as a Schottky barrier formed by the misalignment between the work function of the metal and the charge carrier affinity within the semiconductor [52]. Figure 2.14 depicts the differing Schottky barrier heights (ϕ_{Bp}) between palladium and titanium when contacting directly to WSe_2. For p-type contact, the Schottky barrier height is determined by the difference between the valence band maximum and the work function of the metal [53].

From Figure 2.15 it can be seen that of all the metals surveyed, palladium creates the lowest p-type Schottky barriers to WSe_2. Although even when using palladium there is still a small Schottky barrier present as shown in both Figure 2.14 and Figure 2.15.

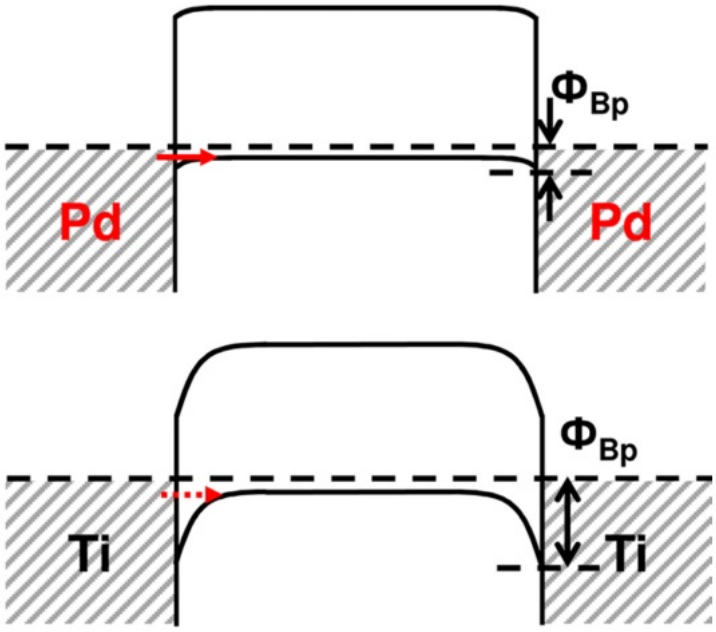

Figure 2.14: Schematic of the Schottky barriers of palladium (top) and titanium (bottom) contacting to WSe_2. ϕ_{Bp} denotes the height of the resultant Schottky barrier potential [53].

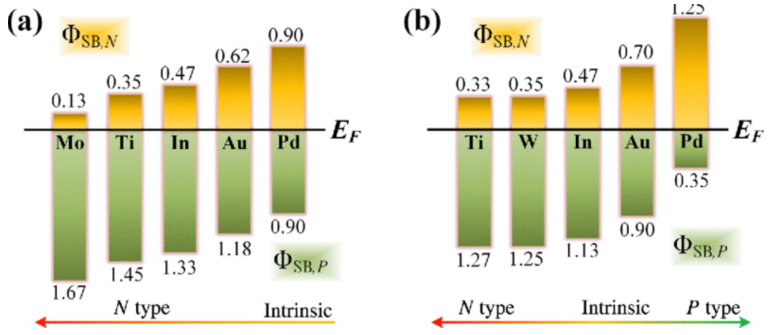

Figure 2.15: Calculated Schottky barrier heights, $\Phi_{SB,N(P)}$ in eV, of different metals contacted to WSe_2 [54].

There have been a number of studies which employ graphene as an intermediary material to reduce the Schottky barrier between a metal and a TMD [22, 55, 56]. The graphene serves to smooth the transition between the metal and the TMD. A number of different approaches have been used to reduce the Schottky barrier using graphene but mainly the focus has been to dope the graphene in order to align the Fermi level in the graphene with, in the case of p-type WSe_2, that in the valence band of the semiconductor, as depicted in Figure 2.16).

One of the most successful methods to dope graphene contacts has been to use an

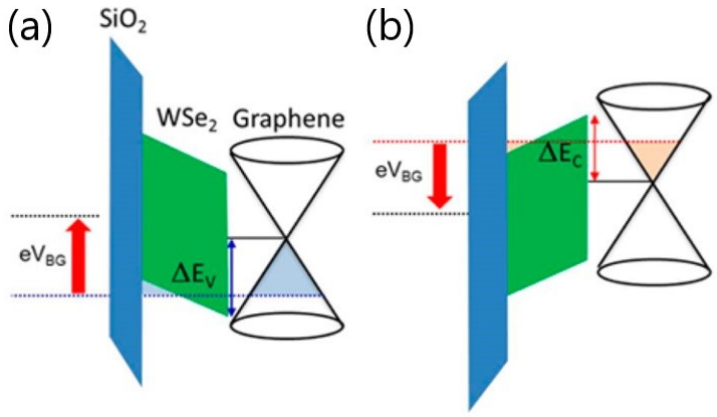

Figure 2.16: Band diagrams (left) of Si02 (blue) and WSe2 (green) depicting the alignment of the Fermi level of graphene, shown on its bandstructure diagram (right), to that of both (a) the valence band edge and (b) the conduction band edge of WSe2. ΔE_V denotes the energy separation between the graphene Dirac neutrality point and the WSe2 valence (a) and conduction (b) band edges, while eV_{BG} denotes the back gate bias [55].

ionic liquid top gate as shown in Figure 2.17 [56].

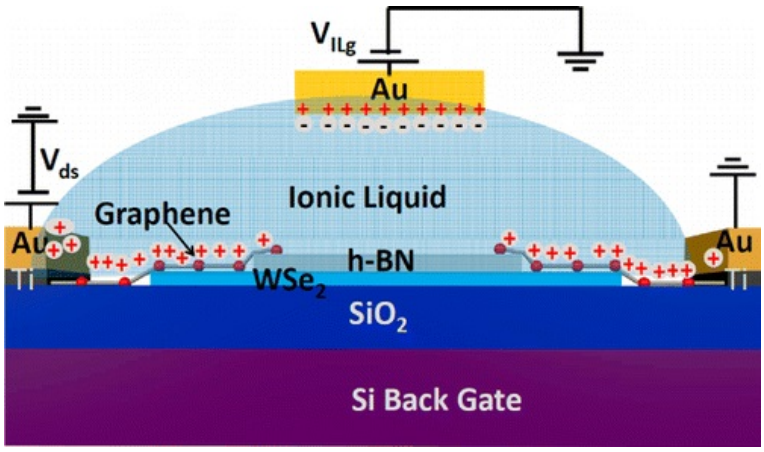

Figure 2.17: Diagram of the device design of the highly doped graphene contacts to WSe_2 [56].

In Figure 2.17 the hexagonal boron nitride (h-BN) isolates the WSe_2 from the ionic liquid contact which thereby acts as a top gate. Despite the effectiveness of this method, it is however unsuitable for investigations involving optical excitation of the WSe_2 by a laser. as such a top gate would prevent the laser light accessing the semiconductor itself.

Other approaches to dope the graphene have been attempted: One approach has been to layer h-BN underneath the graphene and then to shine white light on them

whilst applying a negative gate voltage across both the h-BN and graphene layers [57]. The resulting n-type doping [57] occurs from the defect states within the bulk h-BN flake. There are trapped electrons within the h-BN which are then transferred to the graphene on white light illumination in the presence of a negative gate voltage, as shown in Figure 2.18.

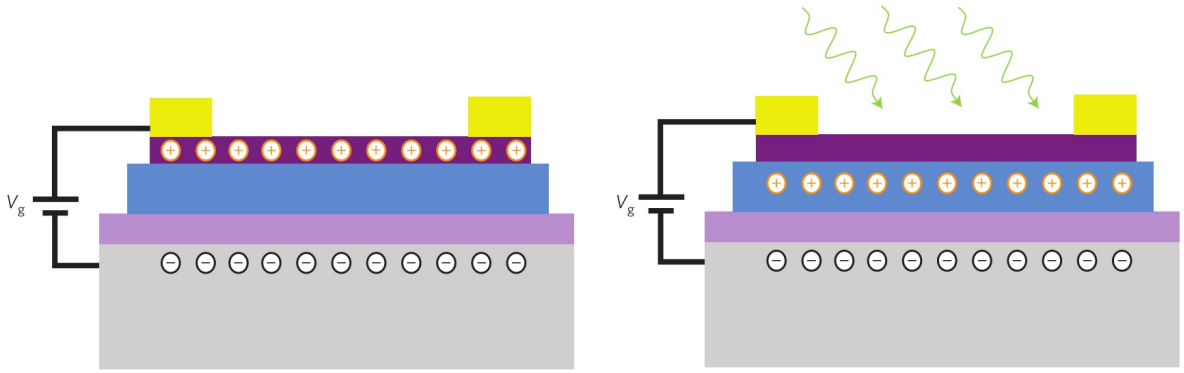

Figure 2.18: Schematics of the device design showing how the graphene becomes n-type doped from the h-BN layered underneath. With the chrome/gold electrodes denoted in yellow, the Silicon denoted in grey, the SiO_2 in lilac, h-BN in light blue and the graphene in purple. The holes (electrons) are denoted by circles with plus (minus) symbols inside whilst the green arrows denote the incoming photons [57].

This n-type doping effect also occurs between SiO_2 and graphene but it is 1000 times stronger from h-BN than from SiO_2 [57]. By using this method, the doping of the graphene is highly tunable and the n-type doping can be restricted to very specific regions. The n-type doping was found to last for many days at room temperature but only as long as the device is kept in a dark environment. N-type doping of up to 3 $\times$ 10^{12} cm^{-2} in the graphene was achieved with the electron mobility remaining stable over the whole charge density range. P-type doping was also observed under white light illumination in the presence of a positive gate voltage although the p-type doping dynamics were orders of magnitude slower [57] This photoinduced doping technique has yet to be used on graphene in TMD contacts. Unfortunately as this is an optically-induced effect it is not applicable to an SHE experiment.

A number of other approaches have been taken to make ohmic contacts to the TMDs that do not employ graphene as an intermediary: one approach has been to

create van der Waals heterostructures with $NbSe_2$ as the intermediary contact for the p- type contact to WSe_2 [58]. The design of these devices is shown schematically in Figure 2.19.

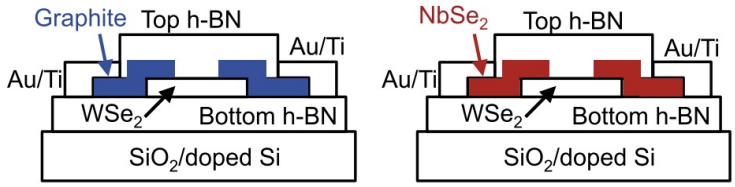

Figure 2.19: Schematic of the device design of the van der Waals p-type $NbSe_2$ contacts to WSe_2 [58].

These van der Waals $NbSe_2$ p-type contacts produced a Schottky barrier height of 50 meV to the WSe_2[58]. This Schottky barrier height is far lower than that of using just a metal contact such as palladium 350 meV [54]. Electrical contact to the $NbSe_2$ was made using titanium/gold [58].

Another device design which has been previously implemented to optimise electrical contact to WSe_2 was to chemically dope regions by exposing just the contact regions of the WSe_2 to nitrogen dioxide (NO_2) gas [53]. Although they give no numerical results for the Schottky barrier height or contact resistance of the device, the paper states that the NO_2 treatment reduces both of these. One drawback of using this technique is that the lifetime of this chemical doping is very low: It is shown that once the device is no longer exposed to the NO_2 gas, NO_2 starts to desorb with the contacts reverting to their original undoped behaviour over time. Within just one minute of being in ambient air there is already change in the device source-drain current of $\sim$35%. Another drawback of this design is that it uses a palladium top gate which also acts as a patterned mask to restrict the NO_2 doping to the contact regions. This would also prevent the laser beam reaching the sample. Furthermore, as the NO_2 doping the WSe_2 contacts saturates after 10 minutes of NO_2 exposure, this combined with the instability of the doping, means that controling the contact resistance is difficult. Fang *et al.*'s work also suggests no means to tune the Fermi energy of the metalic $NbSe_2$ [53].

2.10 Raman and photoluminescence of two dimensional materials

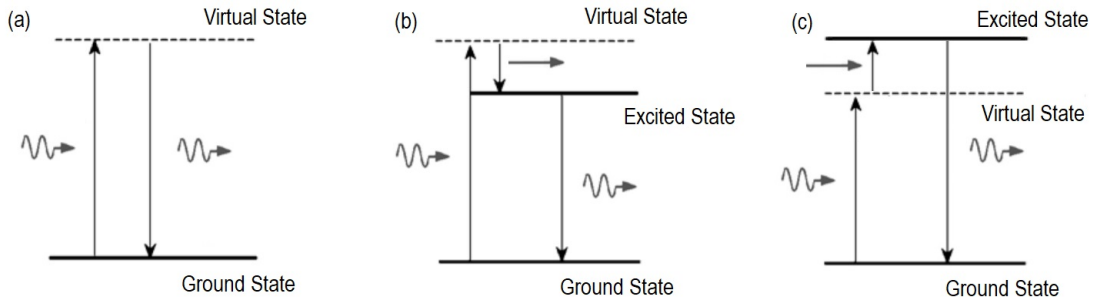

Figure 2.20: Diagrams showing the transitions involved in (a) Rayleigh scatterin, (b) Stokes and (c) anti-Stokes Raman scattering.

Characterising the thickness of TMD and graphene flakes is essential to this research. Raman spectroscopy is a rapid, non-destructive characterisation technique. The basic principle of Raman spectroscopy involves several types of scattering that occur when the electrons are excited in energy by an incoming photon. An electron absorbs the incoming photon leading to it being excited into either a virtual or a real state and then eventually it emits a photon as it drops back down into the ground state; the difference in energies of the incident and scattered photons is what is measured in Raman spectroscopy [59]. In Rayleigh scattering, the incident and scattered photons have the same energy and frequency, shown in Figure 2.20a. In Figure 2.20b, Stokes scattering is displayed: the final photon has a lower energy than the incident photon due to energy being released from the electron in the form of a phonon. Anti-Stokes scattering is where the outgoing photon has a higher energy than that of the incoming photon, Figure 2.20c, this energy is gained by absorbing an incoming phonon. Resonant Raman scattering is where one the excited states is a real state. If this electron is scattered into two real excited states it is known as double-resonant [8].

2.10.1 Raman of graphene

The most prominent characterising features of the Raman spectrum of monolayer graphene are the G line and the G' line (also known as the 2D [60]), the G line appears at a Raman shift of ~ 1582 cm^{-1} and the G' at a Raman shift of ~ 2700 cm^{-1} [61]. The D line, which is a disorder-induced peak, occurs at a Raman shift of ~ 1350 cm^{-1}. The G line is present for all sp^2 bonded carbon systems, it is doubly-degenerate and corresponds to the carbon to carbon stretching mode [62] (Figure 2.21a). The D line is due to the breathing mode within graphene which is also associated, at twice the frequency, with the G' line, as shown in Figure 2.21b.

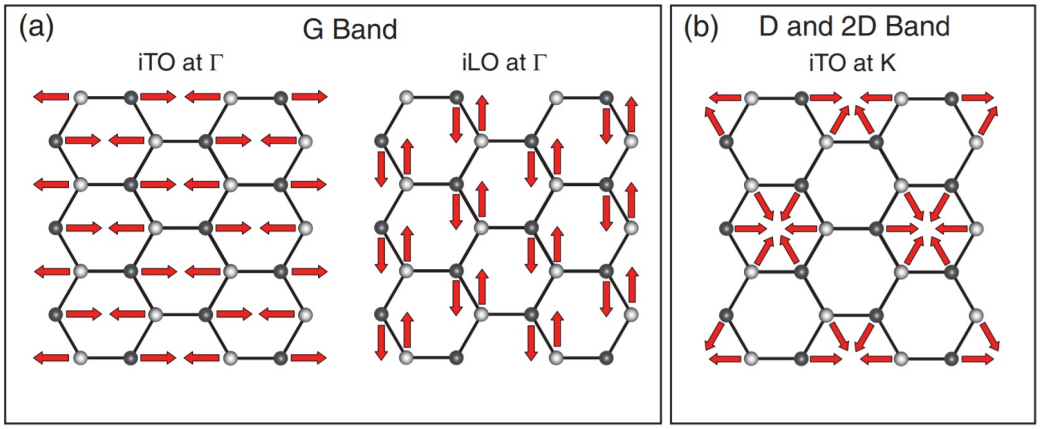

Figure 2.21: Schematic of the phonon vibrations contributing to the main Raman bands in graphene: (a) G band vibration modes for the iTO and iLO phonons at the Γ point. (b) D and G' (2D) vibration modes for the iTO phonon at the K-point [62].

Phonon dispersion is key to understanding the Raman spectroscopy of graphene: In graphene, there are six phonon branches equally divided between optical and acoustic modes. Figure 2.22 shows the six phonon dispersion curves along the high symmetry directions. The D Raman line and the G' Raman line are related to the in-plane transverse optical (iTO) phonon near the K point [61], whereas the G line is associated with both the iTO and in-plane longitudinal optical (iLO) phonon modes which are degenerate at the Γ point.

All electron transitions involved in the Raman processes in graphene are doubly-resonant, where the electron transition starts and ends at real energy states. These are

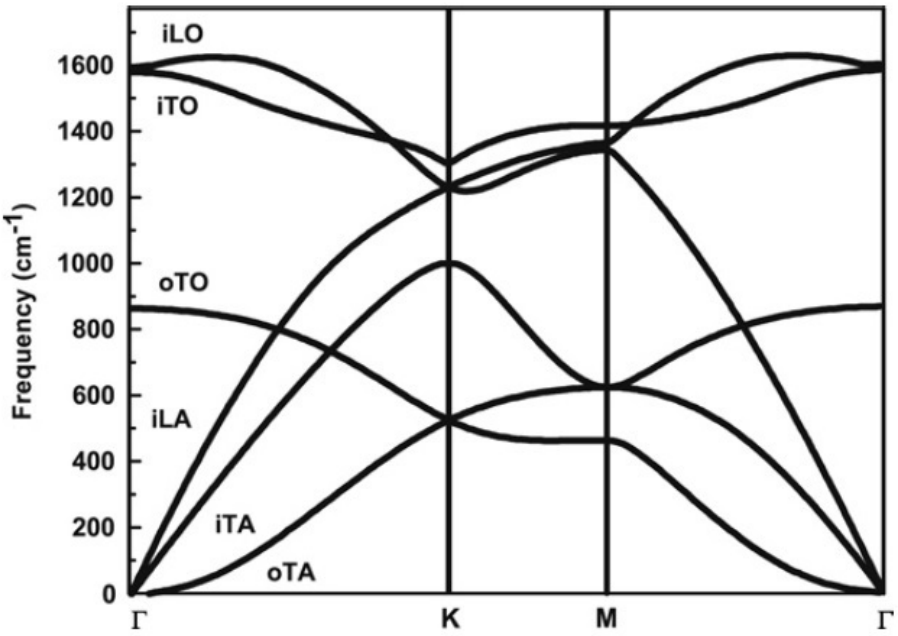

Figure 2.22: Calculated phonon dispersion of monolayer graphene, i denotes in-plane, o denotes out-of-plane, A denotes acoustic, O optic, L longitudinal and T denotes transverse [61].

demonstrated in Figure 2.23. The G mode derives from phonons at the central Γ point of the first Brillouin zone. Figure 2.23 illustrates the path of the electron absorbing an incoming photon, then releasing an iTO (or iLO) phonon which removes energy from the electron which then recombines with its hole, while releasing a photon with lower energy than the incident photon [61]. The D mode occurs when an electron near a K point of graphene absorbs a photon and is then elastically scattered by a defect to a K' point. After inelastically scattering back to its original K points by emitting a phonon it recombines with a hole and emits a photon [61]. Thus, the D mode consists of two scattering processes: one elastic caused by defects of the crystal and one inelastic caused by the emission of a photon [61]. There are two inelastic scattering processes involved in the G' mode involving two phonons, similar to the D mode apart from the initial scattering process is also inelastic, caused by another iTO phonon instead of a defect within the crystal, as shown in Figure 2.23.

The D peak is generally not present in the Raman spectra of monolayer exfoliated flakes of graphene due to the high quality of the graphene and because measurements

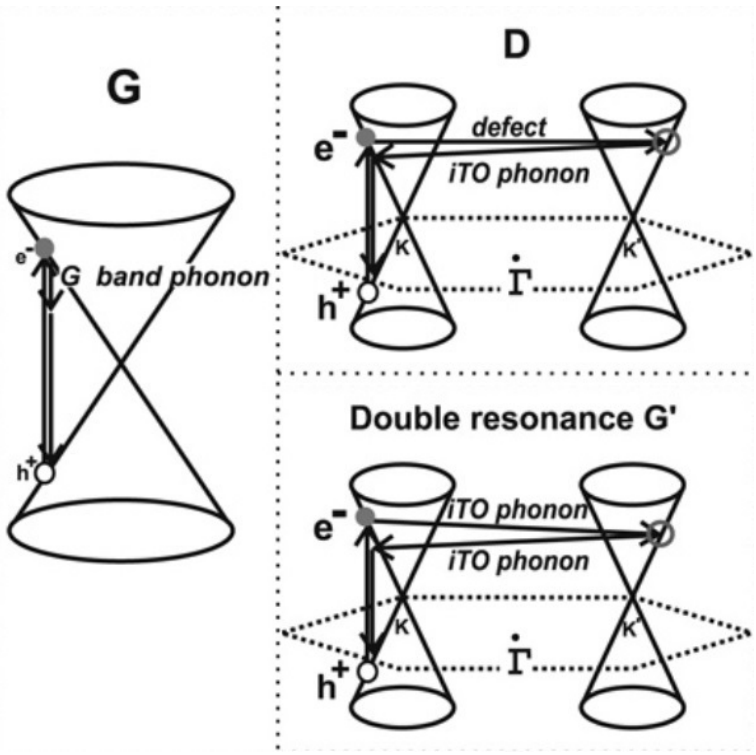

Figure 2.23: The different electron transitions involved in the Raman active modes in graphene [61].

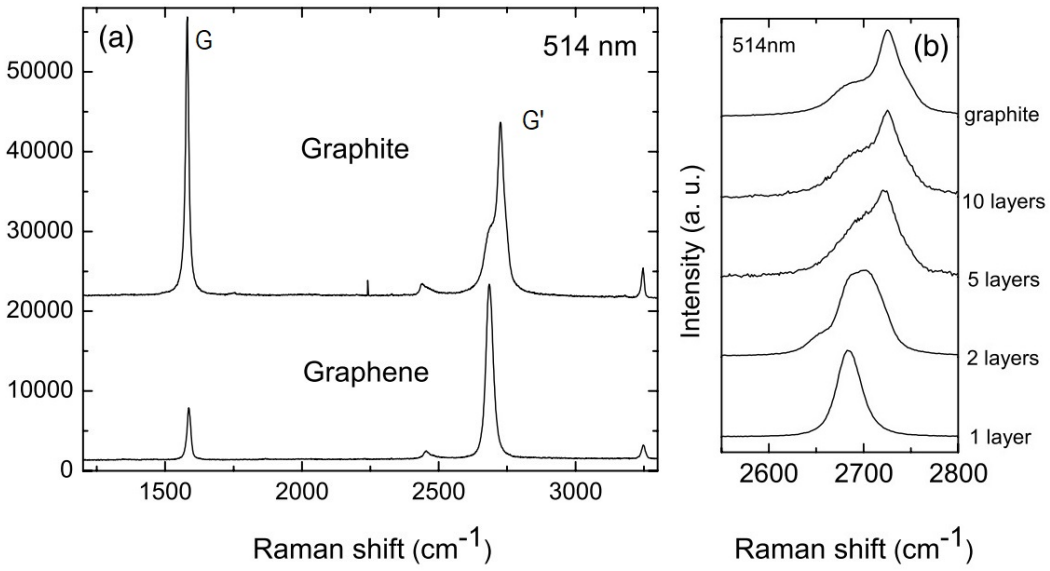

Figure 2.24: (a) Raman spectra of graphite and graphene normalised to the height of the G' peaks. (b) Raman spectra of the G' line for different thicknesses of graphene [60].

are taken away from the edges of the flake [60]. Figure 2.24a shows the Raman spectra of both monolayer graphene and graphite. In monolayer graphene, the intensity of the G' peak is much larger than the G peak and a single Lorentzian. In the bulk graphite,

not only has the G peak grown much more intense than the G' peak, but the G' peak has become much broader with a shoulder to slightly lower energy. Figure 2.24b demonstrates that when the number of layers of graphene is increased the G' peak both broadens and decreases in intensity [60]. Once five layers have been reached there is not much distinguishing the G' line from that of the G' line in bulk graphite. Thus, Raman is an immensely useful tool in determining the number of layers in graphene flakes [60].

2.10.2 Raman of the transition metal dichalcogenides

Raman of MoS_2

Due to the TMDs having six atoms per unit cell instead of two for graphene they have 18 phonon modes: three acoustic and 15 optical modes [8]. Their dispersions are shown in Figure 2.25

For bulk TMDs there are three peaks in the Raman spectrum labelled A_{1g}, E_{1g} and E_{2g} according to their point group symmetry irreducible representations [8]. These correspond to the phonon vibrations depicted in Figure 2.26. In the bulk MoS_2 Raman spectrum they are observed at Raman shifts of: $A_{1g} \sim$ 408.7 cm^{-1}, $E^1_{2g} \sim 383.6$ cm^{-1} and E^2_{2g} at ~ 33.5 cm^{-1} [8]. The frequencies of the corresponding monolayer and few-layer MoS_2 depend on the layer number, with the Raman frequencies of the A_{1g}, E^1_{2g} peak positions being the key characteristic for the determination of layer number [63].

The separation of the E^1_{2g} and A_{1g} peaks is particularly sensitive to layer number, as shown in Figure 2.27. H. Li *et al.* [63] found that the E^1_{2g} peak read-shifts while the A_{1g} peak blue shifts as layer number increases. It is becoming accepted that a peak separation of 18 cm^{-1} between the E^1_{2g} and A_{1g} modes is the most reliable way to characterise single-layer MoS_2 when using Raman spectroscopy [63, 64, 65]. The peak separation of these two Raman lines in bulk MoS_2 is 25.2 cm^{-1} [65]. This separation remains relatively constant until the layer number is reduced below four when this peak separation begins to drop dramatically as can be seen in Figures 2.27 and 2.28.

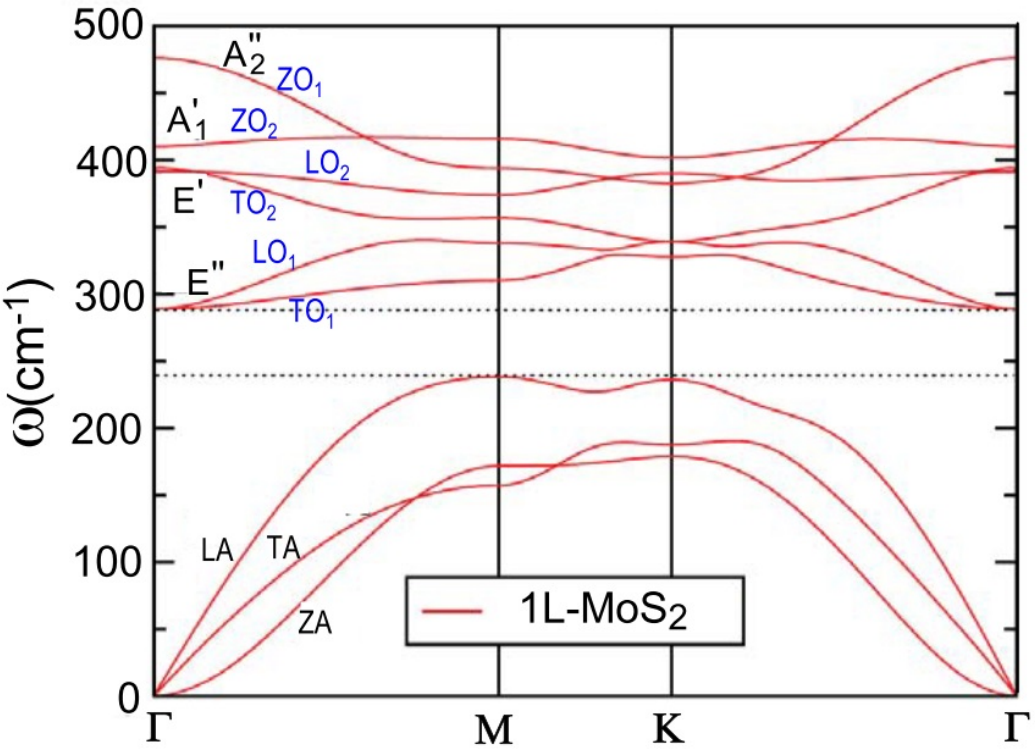

Figure 2.25: Calculated phonon dispersion curves of monolayer MoS_2, Z denotes phonons which are out-of-plane, L denotes longitudinal phonons and T denotes transverse phonons. The two main branches of phonons are denoted by A and O for acoustic and optical, respectively. Mode are labelled according to their point group symmetry irreducible representations. See discussions of these labels in the text [8].

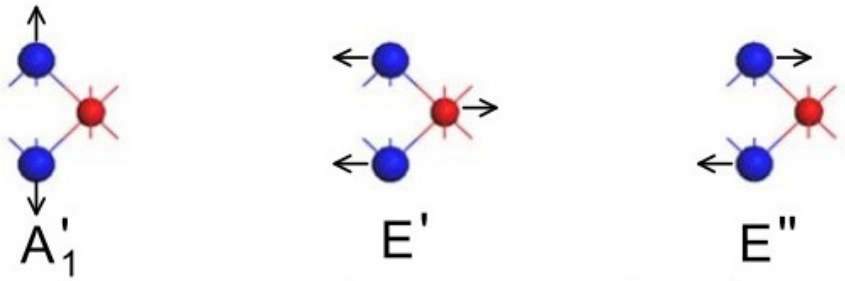

Figure 2.26: Displacements of the Raman-active optical vibration modes for monolayer MX_2. Red denotes the metal atom and blue the chalcogen atoms[8].

Raman of WSe_2

In bulk WSe_2 the single main Raman peak sits at a Raman shift of ~ 250 cm^{-1} and corresponds to the almost degenerate A_{1g} and E^1_{2g} [66]. It has a feature slightly higher in wavenumber, as shown in Figure 2.29. This feature is attributed to the second order Raman mode due to longitudinal acoustic phonons at the M point of the Brillouin zone (2LA(M))[66]. This 2LA(M) feature becomes much less prominent as layer number is

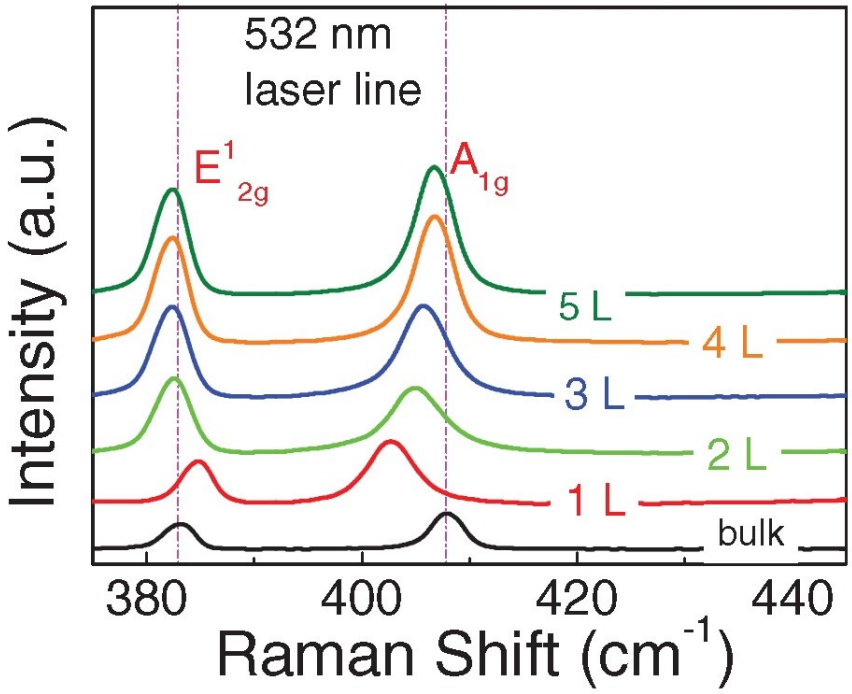

Figure 2.27: Raman spectrum for few-layer MoS_2 and for the bulk material with vertically dashed lines denoting the peak positions of the bulk [63]

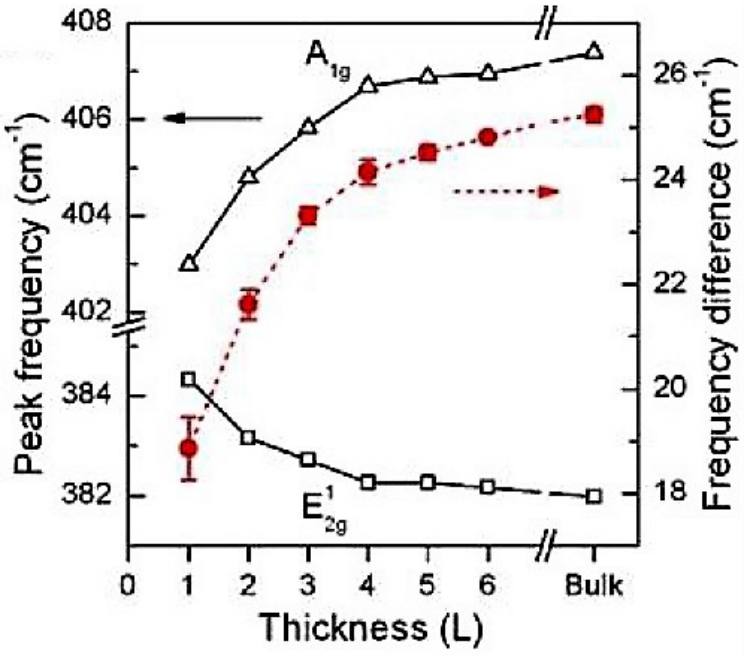

Figure 2.28: Peak frequencies of the E^1_{2g} and A_{1g} and their peak separation for few-layer and bulk MoS_2 as a function of layer number [65].

reduced as can be seen in Figure 2.29. Due to the near degeneracy of the A_{1g} and E^1_{2g} modes in WSe_2 and their small shift in frequency with increasing layer number, this

main peak is not reliable to characterise precisely the number of layers in few-layer WSe_2 flakes. Another Raman peak located around 310 cm^{-1} however, is not present in the Raman spectrum of WSe_2 but can be seen in Raman spectra of few-layer and bulk WSe_2 as is shown in Figure 2.29. Due to the definitive nature of this peak either being apparent or not, it has become the most reliable method to distinguish between few-layer and monolayer WSe_2 [66].

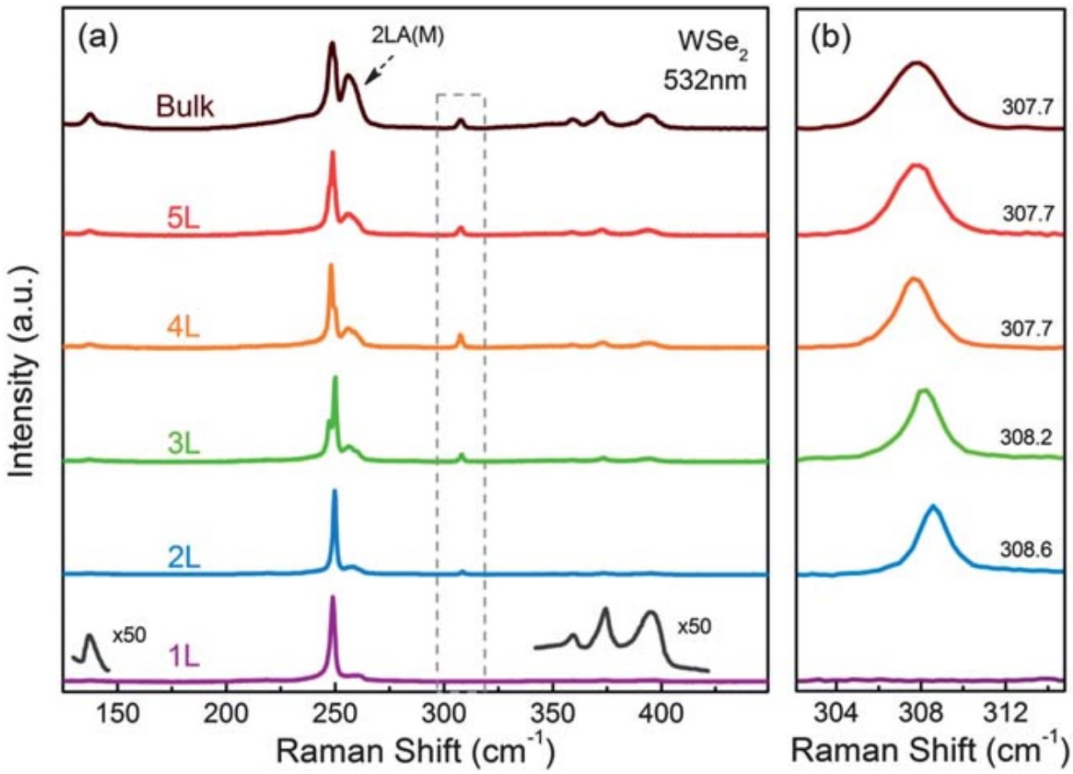

Figure 2.29: (a) Raman spectra of few-layer and bulk WSe_2 normalised with respect to the A_{1g} line (b) Zoomed in section of the spectra which is outlined in (a) by a dashed grey line with the Raman shift labelled [66].

2.10.3 Photoluminescence of transition metal dichalcogenides

As discussed in Section 2.3, one of the most characteristic electronic properties of many TMDs is that their bandgap changes from indirect to direct as the number of layers is reduced to one [35]. One of the key differences between monolayer TMDs and graphene is that the TMDs exhibit photoluminescence (PL) due to their large band gaps. With the presence of a band gap, once the energy of the exciting photon exceeds that of

the band gap, as the electron de-excites, photons can be emitted which will always have energy equal to at least that of the band gap of the material. As the incoming photon excites the electron from the valence band into a real state in the conduction band, depending on the incoming photon energy compared to the band gap, acoustic and sometimes also optical phonons can be released to relax the electron back to the minimum energy state of the conduction band. The electron then emits a photon to recombine with the hole in the valence band, as shown in Figure 2.30. The emitted photons can have various energies due to spin splitting of both the valence and conduction bands but the electron transitions are only allowed between real states of the electronic system.

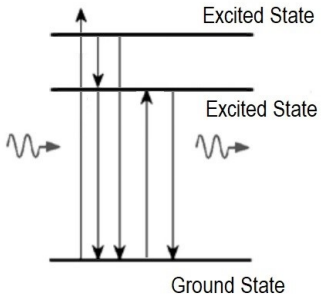

Figure 2.30: Diagram demonstrating the incoming photons exciting an electron above the upper conduction band and then the electron recombining with the hole of the valence band in either one or two steps with photons of different set energies being emitted

Photoluminescence of MoS_2

In bulk MoS_2 due to the indirect nature of its bandgap, there is a very low quantum yield when it comes to PL, but as the number of layers is reduced to just a few layers, the PL becomes noticeable, whilst monolayer MoS_2 gives a relatively strong PL signal [35]. Mak *et al.* [35] compared monolayer MoS_2 PL to that from bilayer MoS_2 and found the difference to be very significant. Bilayer, few-layer and bulk MoS_2 have two emission peaks, A and B, corresponding to direct-gap excitonic PL to the two spin-split valence bands, as described in Section 2.7 [35]. The I line, shown in Figure 2.31, corresponds to the indirect band gap transition between the K and Γ points and therefore

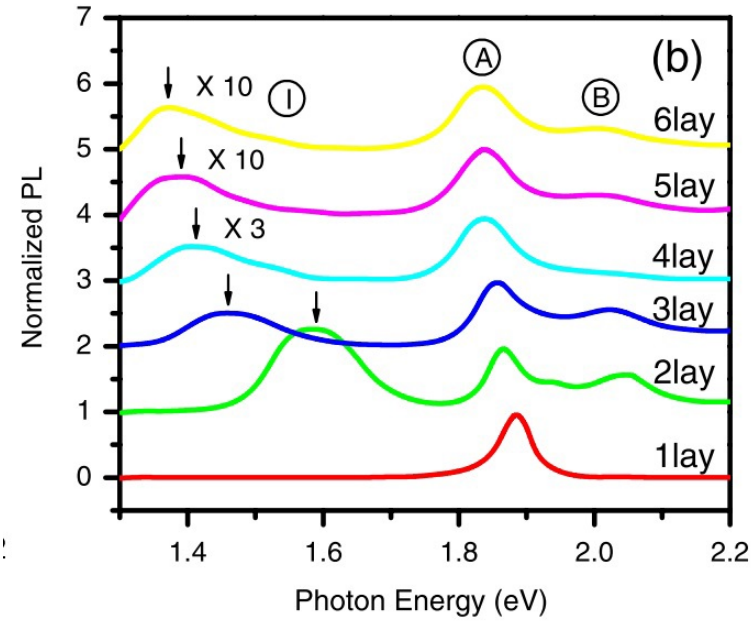

Figure 2.31: The effect of the number of layers of MoS_2 on its photoluminescence [35].

is only observed in the PL spectra of bilayer graphene and thicker. This broad feature systematically shifts to lower energy and reduces in intensity until it approaches the bulk MoS_2 band gap of 1.29 eV [35]. The energy position and intensity of the I line is thus a reliable means to determine the number of MoS_2 layers present.

Photoluminescence of WSe_2

WSe_2 shows similar behaviour to MoS_2: Bulk WSe_2 has an indirect band gap of 1.2 eV in the near-infrared [67], whereas the direct A exciton in monolayer WSe_2 PL peak has been located at 1.65 eV [49]. On reducing from bilayer to monolayer WSe_2, the PL intensity increases by an order of magnitude, as shown in Figure 2.32, which agrees with WSe_2 transitioning from an indirect semiconductor to a direct band gap semiconductor as the layer number reduces to one.

Figure 2.32, shows the PL spectra of monolayer, few-layer and bulk WSe_2. Again, the I peak, which relates to the indirect transition between the K and Γ points [49] increases in intensity and drops in energy (Figure 2.32c) as the layer number increases, with the peak disappearing entirely in the PL spectrum for monolayer WSe_2. Once

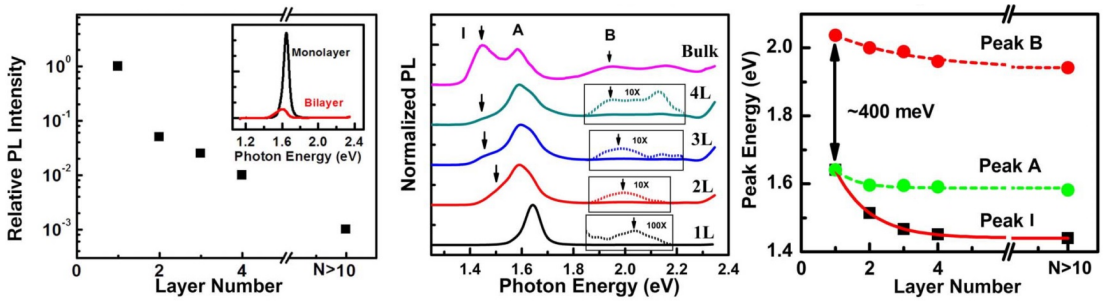

Figure 2.32: (a) Relative intensities of the PL of WSe_2 with respect to layer number (normalised to the PL intensity of monolayer) with the inset displaying the PL of mono- and bilayer WSe_2. (b) PL of mono- few-layer and bulk WSe_2 PL (all offset and normalised for clarity). (c) The energy positions of the PL peaks as a function of the layer number [49].

again this I peak is thus a useful signature of the number of layers present. Another feature of these spectra is the much weaker B exciton PL peak compared to that of the A exciton, which relates to transitions to the lower spin-split valence band. As layer number increases, the energy separation between the A and B PL peaks is shown in Figure 2.32c to be constant at 400 meV [49].

Thus, from these Raman and PL techniques characterisation of graphene, MoS_2 and WSe_2 flakes can be achieved.

2.11 Strain effects in graphene

The graphene device fabricated during this project is to be used to measure strain effects in graphene so a brief introduction of how the Raman spectrum of graphene changes under thermally induced strain effects will be given here.

The Raman G and G' transitions both soften and the G peak splits under tensile strain [68]. Graphene has a negative thermal expansion coefficient which depends heavily on the temperature, at room temperature its value is -8.0 $\pm$ 0.7 $\times$ 10^{-6} K^{-1} [69]. When the flakes are on a SiO_2 substrate and the temperature is varied between 4.2-475 K, the differences between the thermal coefficient of the SiO_2 and the graphene flakes leads to a strain being applied to the graphene, which can be shown via the Raman spectra, as shown in Figure 2.33.

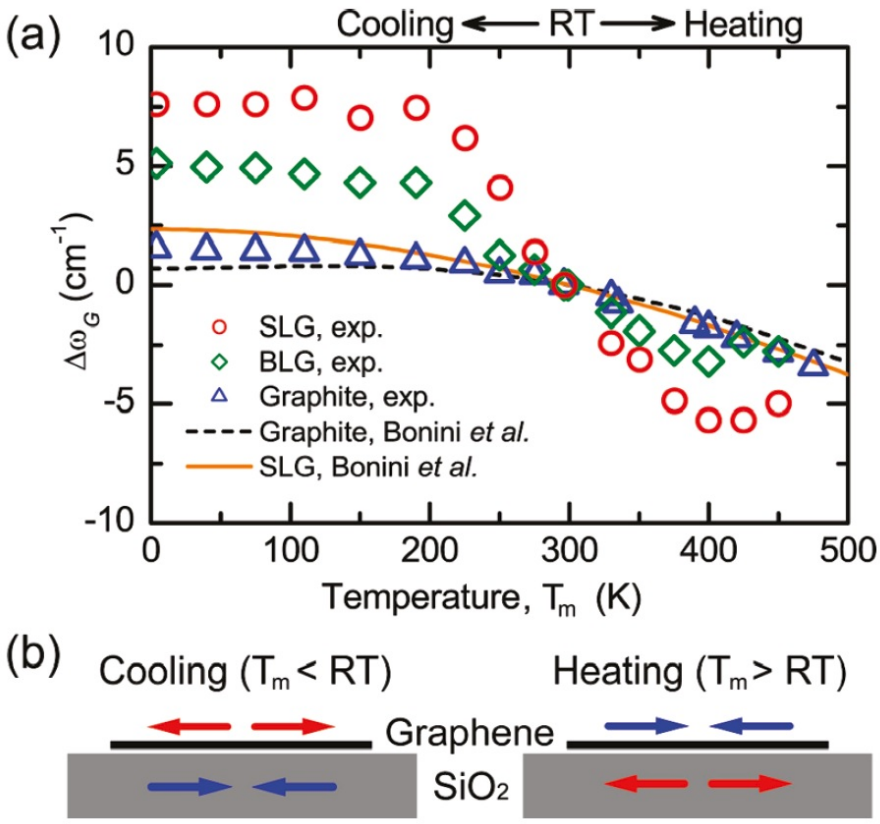

Figure 2.33: (a) The G line Raman frequency shifts of mono- (SLG), bilayer graphene (BLG) and bulk graphite as a function of temperature. The solid and dashed lines are theoretical results. (b) Schematic showing how the thermal expansion and contraction of the flakes and substrates interact when heating and cooling the sample. [69].

Although strain experiments have been done before on graphene, slipping has been a potential issue when it comes to measuring higher strains [69]. The slipping is denoted by the saturation behaviour exhibited in the temperature dependence of the G Raman peak position in Figure 2.33. By pinning the flakes to the substrate using the contacts, slipping should be prevented. This device was not the focus of this project and therefore further discussion of these experiments is beyond the scope of this thesis.

2.12 Summary and conclusion

This chapter has covered the background physics behind both graphene and the TMDs. The theory behind spin-orbit coupling has been covered along with a description of some of the new types of Hall effects that have been discovered. This chapter has reviewed

previous work on the SHE and VHE in 2D materials while on combining these fields with the hurdle of contacting to TMDs in order to minimise the associated Schottky barriers. Next, this chapter has covered the factors and properties which have led to WSe_2 being chosen as the most appropriate TMD for measuring the photoinduced transverse voltage resulting from the SHE. Raman and PL spectroscopy have been described and how they have been applied to both graphene and the TMDs. Finally a very brief overview of strain in graphene has been given.

Chapter 3

Experimental Details

3.1 Introduction

In this chapter, the processes and equipment used within this investigation are discussed. Firstly, the methods will be explained starting with the fabrication and characterisation of the graphene and transition metal dichalcogenide (TMD) flakes, after which the processes used to shape the flakes and fabricate contacts on the flakes will be described. Lastly the choice of TMD is discussed with respect to the experimental facilities available and the differences in the properties of the more stable and conventionally used TMDs.

The second part of this chapter explains the equipment used to fabricate, characterise and probe the properties of the TMD/graphene devices.

3.2 Experimental Methods

3.2.1 Introduction

This section explains the different techniques used in this project. Firstly, the steps taken to exfoliate the few layer flakes will be described as well as the differences in the exfoliation technique for the various 2D materials. Next, how the few layer flakes are

characterised is explained. Finally, the device design will be discussed.

3.2.2 Exfoliation

This section describes the exfoliation techniques for exfoliating both the graphene and TMD flakes. Although the concept is similar, the exfoliation techniques for graphene and for the TMDs differ in the details of the materials and techniques employed.

The substrates that were used in this project were the same for both graphene and the TMDs. Silicon substrates of 1 cm $\times$ 1 cm area have a silicon dioxide (SiO_2) layer on top which has a thickness of 290 nm. The top surface of the Si/SiO_2 substrates are prepatterned with gold alignment markers which are numbered like a grid and are used as co-ordinates when subsequently locating flakes deposited on their top surface. These substrates are cleaned in acetone and then sonicated at 37 Hz for 10 minutes. The substrates are then placed in propan-2-ol (iso-propylalcohol - IPA) to remove any residues of the acetone. After these cleaning processes, the substrate is placed in an oxygen plasma in the reactive ion etcher (30 sccm O_2, 30 mT, 30 W, 30 seconds) (see Section 3.3.5 for a description of the reactive ion etcher), to remove any remaining polymer residues on its surface. The final step to prepare the substrates is to place them on a hotplate at 100°C to evaporate any water left on their surface.

Exfoliating graphene

Blue adhesive tape is pressed onto the graphite and slowly peeled off. After inspecting this tape for flakes, the tape is then pressed onto another piece of tape and again peeled back. This pressing and peeling of the two pieces of tape is repeated between 10-15 times, until 1 cm^2 of the tape has a distribution of flakes in it. This tape is then pressed with a moderate amount of force onto the substrates at a temperature of 100°C for one minute.

Exfoliating transition metal dichalcogenides

Blue adhesive tape is pressed onto bulk TMD similar to the procedure described in Section 3.2.2. Only between 3-5 peels between the two tapes however are required with these TMD materials. Also, a greater level of care is taken to make sure that the areas of tape covered with TMD flakes are always pressed onto clean areas of the tape. The tape is then pressed onto a layer of polydimethylsiloxane (PDMS) firmly for one minute. This PDMS is then placed on top of the Si/Sio_2 substrate, which again is prepatterned with alignment markers. A clear colour change indicates when good contact is made and then the PDMS is pressed down firmly with care given to not exerting any perpendicular or twisting force on the PDMS.

3.2.3 Optical contrast

After removing the adhesive tape, the Si/SiO_2 substrate is inspected under an optical microscope. Searching row by row, under 200× magnification means that any few-layer flakes of useful (minimum of $8\mu m^2$)size can be spotted. Once a potential flake has been found, it is centred on the microscope and then the magnification is increased to 500× for more detailed pictures to be used in the AutoCAD design file (description given in Section 3.3.3). By scanning across the substrate row by row, the entire substrate is searched thoroughly, any flakes too small for 200× magnification would not be suitable for this investigation.

To find flakes on the substrate, look for slightly darker regions (as shown in Figure 3.1). Due to its single atomic thickness, graphene is very difficult to see optically and it only becomes relatively easy to notice these regions when looking at flakes of two or more layers. The difference between the intensities of the reflected light in the regions with or without graphene is what we call the optical contrast [70]. To improve its optical contrast, a green filter is used when searching for graphene monolayer and few-layer flakes [70]. As shown in Figure 3.2 which has been calculated using Fresnel's Law. To maximise the contrast of graphene under green light (533 nm) a SiO_2 thickness

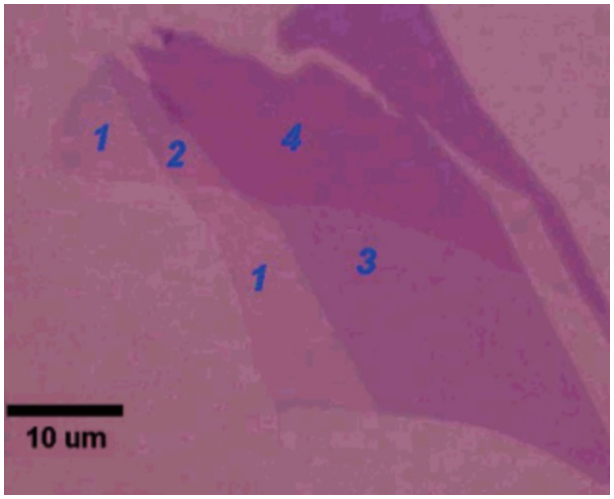

Figure 3.1: Optical micrograph of a graphene flake with a thickness ranging from 1 to 4 layers [71]).

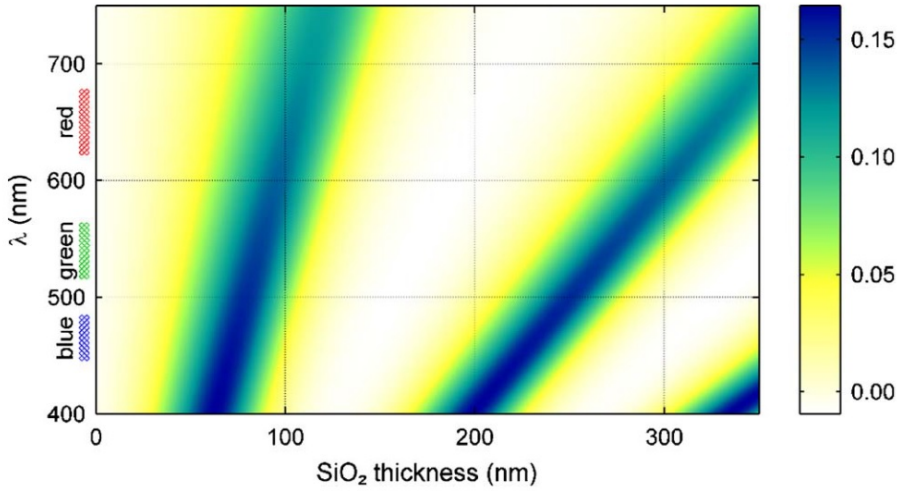

Figure 3.2: Calculated changes in the optical contrast of monolayer graphene on Si/SiO_2 substrates as a function of the wavelength of incident light and the thickness of the SiO_2 layer with the colour scale on the right depicting the expected contrast [70]).

of 290 nm is ideal. Although a SiO_2 thickness of 90 nm would also have a near equal optical contrast, we used 290 nm – thick SiO_2 on our substrates.

The calculations of Figure 3.2 have been supported with experimental practice and now searching for graphene monolayer and few-layer flakes on ≈290 nm thick SiO_2 on Si using green light has become common practice. Under light with a wavelength of 550 nm, graphene flakes have optical contrasts of 0.09 ± 0.005, 0.175 ± 0.005 and 0.255 ± 0.01 for mono-, bi- and trilayer respectively [71]. There are however variations when observing these flakes under different conditions and the ability to spot and identify

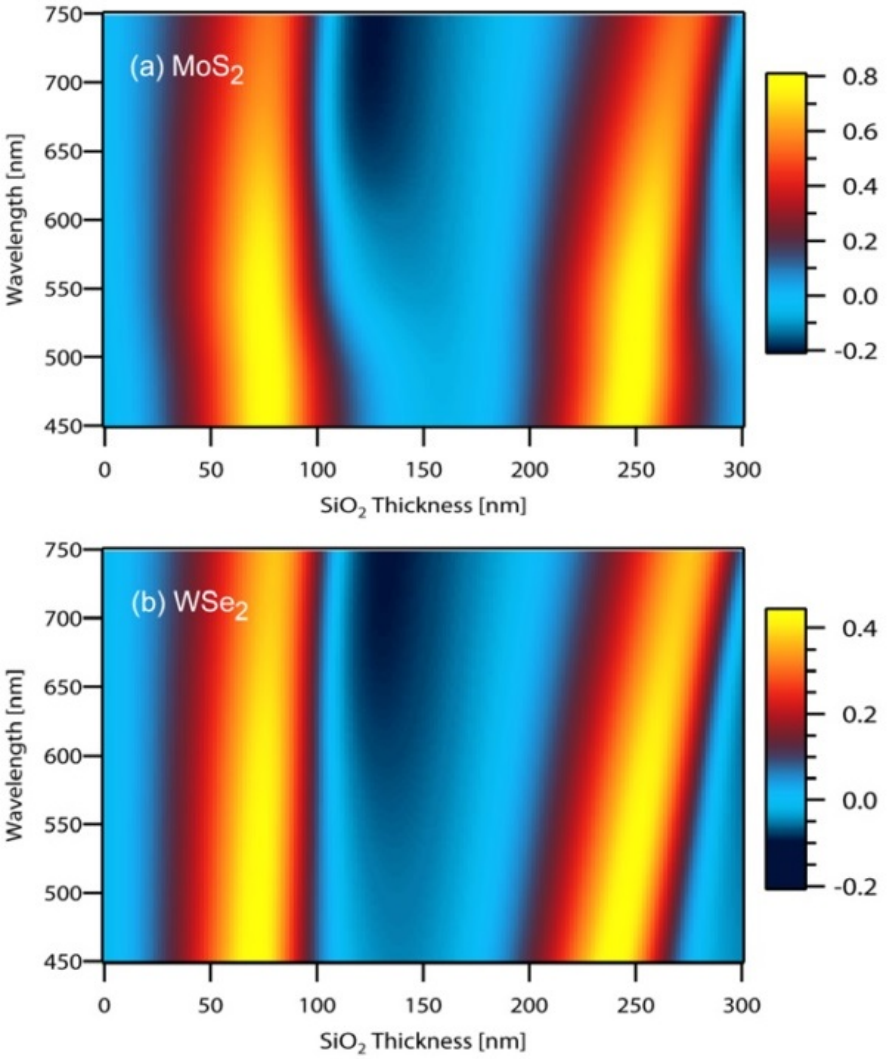

Figure 3.3: Calculated changes in the optical contrast of monolayer (a) MoS_2 and (b) WSe_2 on Si/SiO_2 substrates as a function of the incident light wavelength and the SiO_2 layer thickness, with the colour scale on the right depicting the expected contrast [72].

the flakes does depend on the experience of the observer [71]. In Figure 3.1 a flake of multiple thicknesses is shown in order to display how the contrast changes through monolayer to up to 4-layer-thick flakes.

As substrates used for the graphene exfoliation had SiO_2 layers of 290 nm thickness, it was decided to keep using substrates with this thickness even though it is possible to attain higher optical contrast for the TMDs by using a SiO_2 thickness of 250 nm thickness as the optical contrast of TMDs is much higher than that of graphene. For these TMD monolayer and few-layer flakes, red light has the highest contrast on our

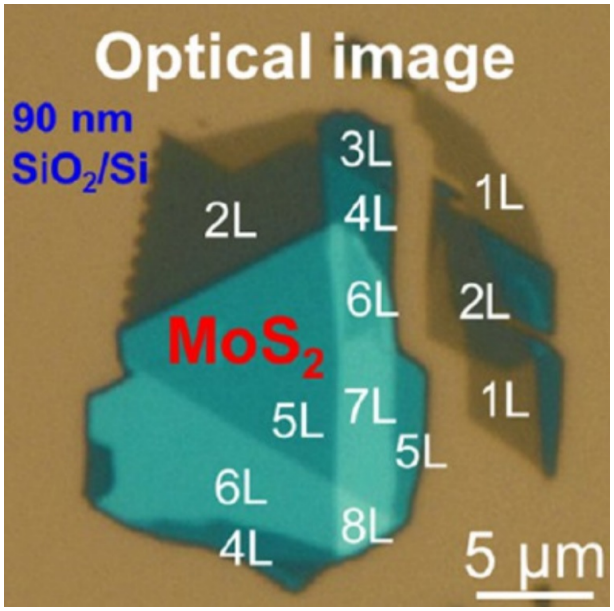

Figure 3.4: Optical micrograph of a MoS_2 flake with a thickness ranging between 1 and 8 layers [73]).

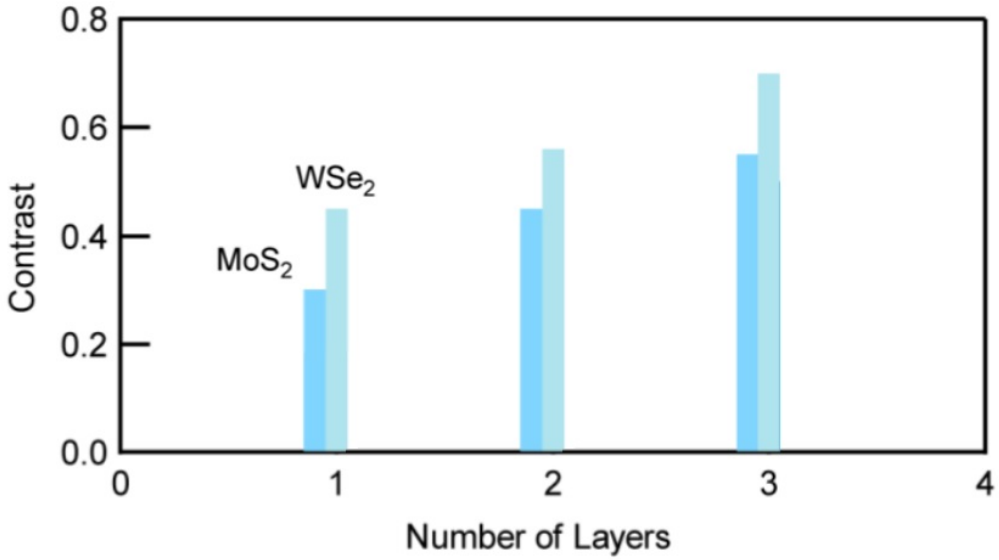

Figure 3.5: Contrast of MoS_2 and WSe_2 on 270 nm SiO_2 topped substrates [72].

substrates with 290 nm-thick SiO_2 layer according to Fresnel's Law, as can be seen in Figure 3.3. To truly maximise the contrast when searching for TMD flakes, the substrates should have a SiO_2 layer $\approx$ 250 nm thick, where the optical contrast for monolayer MoS_2 is $\approx$80% and for WSe_2 is around 40% under 550 nm light [72]. Due to the experience gathered searching for graphene flakes, the lower contrast of using 290 nm thickness of SiO_2 did not cause much of a problem as the contrast is still much

higher than that of graphene as can be seen by comparing shown in Figures 3.2 and 3.3. Although there is an increase in the optical contrast as layer number increases, as depicted in Figures 3.4 and 3.5, this contrast change is not significant enough to definitively characterise the number of layers in a TMD flake even on substrates with the optimised 250 nm thickness of SiO_2 due to changes in the lighting conditions of the laboratory leading to even larger changes in contrast.

3.2.4 Raman and photoluminescence

Once few layer flakes have been located by detecting changes in the optical contrast under an optical microscope, a further step is required to more definitively verify the thickness of the flakes. Raman spectroscopy is used for both graphene and TMD flakes. Photoluminescence (PL) is also used when characterising TMD flakes. Monolayer graphene has no band gap [23], therefore PL is not used for the characterisation of graphene flakes. In this section, how the Raman microscope is employed for both Raman and PL spectroscopy will be described. The Renishaw Raman microscope itself is described in Section 3.3.2.

The Raman microscope incorporates a 49 mW laser with a wavelength of 532 nm and a 2400 grooves/mm diffraction grating. The Raman microscope is controlled by a software programme called 'Wire 2.0'.

To characterise graphene flakes Raman spectra are taken at a laser power of 3 mW, to protect the flakes. Typical spectra are shown in Figure 2.24. The D peak lies at 1350 cm^{-1}, the G peak at 1600 cm^{-1} and the 2D peak at 2700 cm^{-1}. Discussion of the Raman spectra of graphite and graphene samples is given in Section 2.10

Raman spectra of TMD flakes are collected in a similar manner to those from graphene flakes. The peaks of monolayer MoS_2 normally lie around 380 cm^{-1} for the $E^1{}_{2g}$ peak and 410 cm^{-1} for the A_{1g} peak [63] (Figure 2.27). In Raman spectra for monolayer WSe_2 the $E^1{}_{2g}$ and A_{1g} peaks are degenerate at around 249 cm^{-1}. An additional Raman peak appears only for multilayer WSe_2 flakes at 310 cm^{-1} [66], as

shown in Figure 2.29. This is discussed in detail in Section 2.10.

The PL of WSe_2 peaks at 1.65 eV [74] and that of MoS_2 at 1.85 eV as shown in Figures 2.31 and 2.32. A discussion of the PL spectra of TMDs is given in Section 2.10.

3.2.5 Design of the graphene flake and its metal contacts

Once the flakes have been characterised using optical contrast (Section 3.2.3), Raman and PL spectroscopy (Section 3.2.4), the next stage of the fabrication process is the design of the shape of the graphene flake shape and to add electrical contacts to the graphene flake. The graphene devices were designed using a computer-aided design programme called AutoCAD (see Section 3.3.3). AutoCAD enables the design of the shape of the flake as it is used to produce the pattern which the electron beam follows and thereby also the subsequent reactive ion etch (see Section 3.2.6 for a description of these two techniques).

Gold electrical contacts to the flake are also designed via AutoCAD. We ensure that the innermost edges of these gold contacts on opposite sides of the graphene flake were parallel to one another to ensure a uniform electric field across the flake. In order to minimise the contact resistance, the contacted area of the flake was maximised whilst also leaving sufficient space for a laser beam spot between the contacts. The outermost edges of the gold contacts were aligned with the edge of the final shape of the graphene flake.

Because this graphene device was destined for strain measurements, AutoCAD was once again employed, this time to add additional 'pins' to the gold contacts. The 'pins' were 300 nm across and spread along the innermost edges of the gold contacts at intervals of 1.6 μm. To fabricate the holes for these 'pins' the etching recipe used to shape the flake (see Section 3.2.6) was designed also to etch into the silicon dioxide layer of the substrate. This ensures that the 'pins' passed through the graphene and into the SiO_2.

Next the metal wires connecting the gold contacts on the graphene to the contact

pads are designed also in AutoCAD. The contact pads themselves were 200 μm by 200 μm squares. This is actually four times more area than is required, but in case there are any difficulties in bonding gold wires to these contact pads then this allows there is space for multiple bonding attempts.

3.2.6 Lithography and reactive ion etching

Here we describe the two main processes used to shape the graphene flake: electron beam lithography (EBL) (Section 3.3.4) and reactive ion etching (Section 3.3.5).

The first step is to prepare the substrates for EBL ((a) of Figure 3.6). The substrates are spin coated with a 350 nm layer of polymethylmethacrylate (PMMA, 6% dissolved in anisole) using a spin speed of 3500 RPM whilst the substrate is held in place on the spinner by a vacuum. Once the PMMA resist is spun the substrates are baked for 10 minutes at 160°C. The point of the resist is that electron beam exposure monomerises the PMMA which makes the exposed areas of the positive resist soluble in the developer whilst the unexposed areas of the PMMA do not dissolve in the developer. The thickness of the PMMA is decided by balancing the required resolution, where a thicker layer reduces the resolution, against the flakes having a better level of protection during the reactive ion etching process. 350 nm thickness was the decided value.

The developer used was propan-2-ol, 4-methyl-pentan-2-one and methyl ethyl ketone at respective ratios of 15:5:1

The spin-coated substrate is loaded into the scanning electron-beam microscope (SEM). The SEM sample chamber is then pumped down to 10^{-8} mbar. The electron beam is set to 1 nA with an acceleration voltage of 80 KeV. The PMMA resist then has the etch mask written into it, following the patterns laid out in the AutoCAD design file, as shown in figure 3.6 (c).

Once the substrate is removed from the SEM it is put in the developer for 15 seconds. The developer used was propan-2-ol, 4-methyl-pentan-2-one and methyl ethyl ketone at respective ratios of 15:5:1. The developer removes the areas of PMMA exposed to

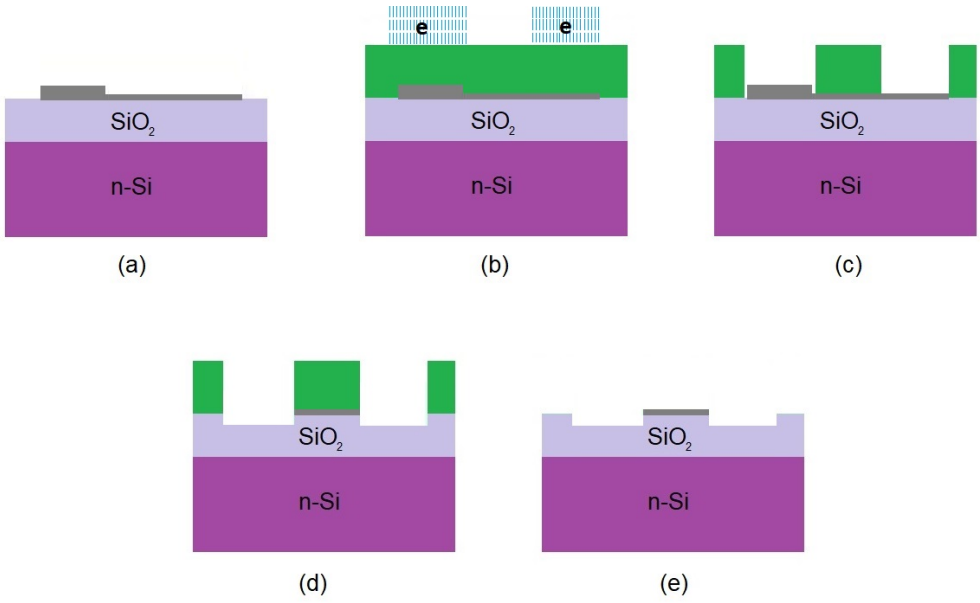

Figure 3.6: Schematics of each of the steps of electron beam lithography and reactive ion etching: (a) The substrate with an exfoliated flake on top (graphene flake denoted in grey), (b) The PMMA (green) spin-coated substrate with the electron beam paths shown. (c) The resulting etch mask after EBL and subsequent PMMA development. (d) Etched graphene showing the partial removal of the flake, (e) Sample after removal of the PMMA.

the electron beam. The substrates are then cleaned in IPA for 45 seconds. Once this development step has been completed, only the areas of PMMA remain that were not exposed to the electron beam (Figure 3.6c).

Next comes the dry etch: firstly, the reactive ion etcher (RIE) is cleaned to remove any potential contaminants from the chamber. The substrate with its PMMA etch mask is then inserted into the RIE. Argon gas is used to etch the graphene - 30 sccm (standard cubic centimetres per minute) at a pressure of 30 mT, and a power of 10 W for 50 sec. Once the sample has been etched it is removed and placed in warm acetone to wash off the remaining PMMA etch mask and then in IPA to remove any residues from the acetone. The substrates are then blow dried in nitrogen.

3.2.7 Metallisation

After the electron beam lithography and reactive ion etching stages have shaped the graphene flake, metallisation is the next stage. Here the process of fabricating the electrical contacts will be described. For operation of the metal evaporator see Section 3.3.6. Gold adheres well to graphene and so is used for electrical contacts to the flakes themselves. As gold, does not adhere well to SiO_2, chromium is used as a "glue" between the gold and the SiO_2. Thus, the chromium slightly overlaps the gold contacts on the flakes to ensure continuous electrical conductivity between the flakes electrical contacts, along the wires, to the electrical contact pads situated somewhat away from the flake displayed in Section 4.4.

To fabricate metal contacts on the graphene flake, the samples go through another couple of rounds of EBL. Similarly, to Section 3.2.6, the sample is spin coated again with PMMA. It undergoes EBL following the AutoCAD design (Sections 3.2.5 and 3.3.3) and then the resist is developed. However, now the partially PMMA coated sample is inserted into the metal evaporator. In this first round of, gold is evaporated to form metal contacts to the flakes (Figure 3.7). Once the rate of deposition reaches 1 Å per second the shutter is removed and the deposition counter is reset to zero to ensure the an accurate reading of the thickness of the gold deposited. Once the gold has reached a thickness of 50 nm, the deposition is stopped and the sample is removed from the evaporator.

With the gold contacts in place, the sample goes through another round of EBL involving spin-coating in PMMA, EBL according to the AutoCAD design (Sections 3.2.5 and 3.3.3) followed by resist development. It is then placed inside the evaporator once again for the creation of chromium wires and contact pads. 5 nm of chromium is deposited (Figure 3.7c). Finally, the chromium boats in the evaporator are replaced with ones containing gold which is deposited on top of the chromium. 100 nm of gold is then deposited (Figure 3.7d). Finally the remaining PMMA is dissolved away in acetone by lightly swirling the acetone with the substrate, as the PMMA dissolves the

metal not in direct contact with the substrate or flake is removed leaving the device on the substrate (see Figure 3.7).

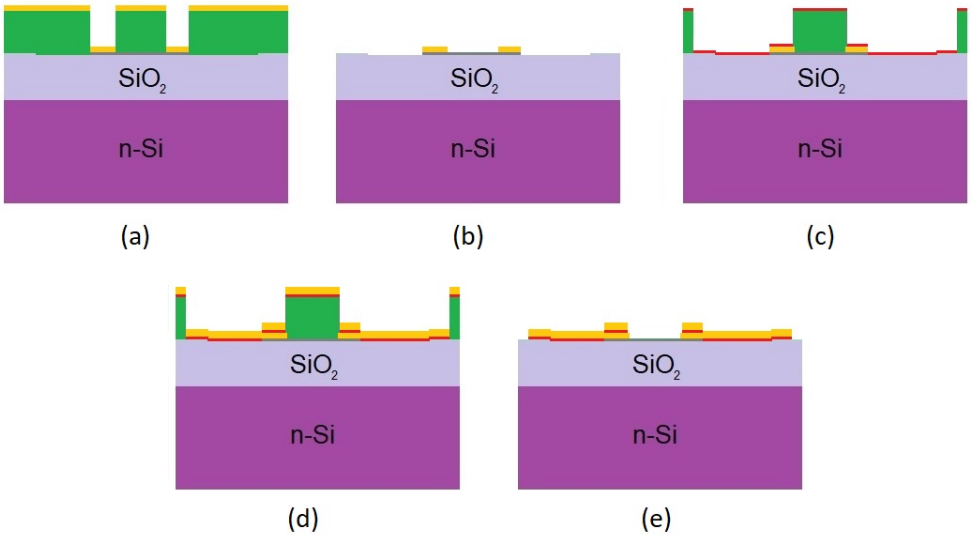

Figure 3.7: Schematics of each stage of the metallisation process (a) PMMA (green) coated sample graphene (denoted in grey) with the first layer of gold on top (b) After the first lift off showing the gold remaining on the graphene flake (c) The second PMMA mask with chromium (red) on top (d) Gold applied on top of the chromium (e) After the second lift off with the contacts, wires and contact pads left on the substrate.

3.2.8 Flake stacking

In order to optimise the electrical contact to the TMD flake it was decided (see Section 2.9 for more detail) that intermediary graphene contacts would be required between the metal and the TMD. Such graphene contacts are produced by stacking the graphene flakes on top of the TMD flake. We employed the PDMS technique described in Section 3.3.7.

Firstly, graphene is exfoliated but instead of depositing the resulting graphene flakes directly onto the Si/SiO_2 substrate, the graphene flakes are deposited onto a PDMS layer. A search using an optical microscope is then undertaken for few layer flakes. It is difficult to distinguish the exact number of graphene layers at this stage due to their contrast on PDMS not being as good as when they are deposited on Si/SiO_2 due to the single-layer nature of the PDMS prohibiting contrast enhancement by interference

(see Section 3.2.3). A stacking station is used to execute the stacking of the flakes, the steps taken to operate this equipment is described in Section 3.3.7.

It would be optimal to have multiple few-layer graphene flakes on the PDMS in the perfect arrangement and each of the correct shape as this would allow these multiple few-layer graphene flakes to be deposited on the TMD flake altogether in one stacking attempt. However, it would be very difficult to etch the few-layer graphene flakes into the correct size and distance from each other to form the ideal arrangement on the PDMS as the PDMS is both not flat enough and it is too soft a material for EBL processing and etching. Thus, repeated stacking attempts were made involving individual few-layer graphene flakes each time. Such multiple stacking of individual few-layer graphene flakes increases the risk of the TMD flake being removed at each stacking attempt.

The few-layer graphene flakes are positioned on the TMD flake at the locations where the electrical contacts are to be positioned. The benefits of using graphene as an intermediary contact material are outlined in Section 2.9.

3.2.9 Choice of transition metal dichalcogenide for resonance with laser

Resonant excitation of the TMDs is preferable for spin/valley Hall experiments as explained in Section 2.6. Taking into account lasers available (for a full list of lasers available see Section 3.3.8) a comparison of the TMD band gaps was made (see Table 2.1). With these two pieces of information the only TMD which can be resonantly excited by one of the available lasers was WSe_2 using the Ti-sapphire laser.

3.3 Experimental Equipment

3.3.1 Introduction

As mentioned in Section 3.2 the Raman microscope is used for characterisation of the graphene and TMD flakes. A computer-aided design program has been used to design both the shape of the flakes and their contacts, wires and contact pads. A scanning electron microscope was employed for EBL after which the flakes were reactive ion etched. An evaporator was used to deposit the metal contacts on the flakes. All these different pieces of equipment are described in detail in this section. Lastly, insight is provided on how various lasers available impacted the choice of TMD investigated.

3.3.2 Raman microscope

The Renishaw Raman Microscope RM1000 was used to characterise both the material of the flakes and the number of layers in the exfoliated flakes.

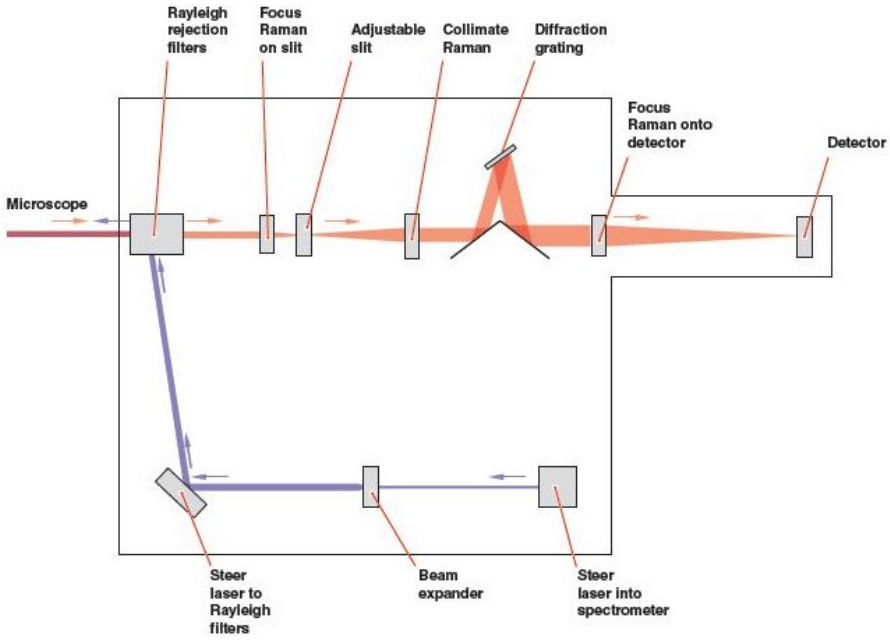

Figure 3.8: Schematic of the Renishaw RM1000 Raman microscope showing the path of the laser beam going to and from the microscope [courtesy of Renishaw].

The Raman microscope contains a series of mirrors and filters which act on the laser beam: once the laser beam has entered the spectrometer, as depicted in the bottom

right corner of Figure 3.8, it is reflected off a mirror. This laser beam then passes through a beam expander to expand the width of the laser beam. The laser beam is then reflected up by another couple of mirrors shown on the bottom left and top right of Figure 3.8 into the microscope where the laser beam is focused onto the sample. This laser excitation causes both elastic (Rayleigh) and inelastic (Raman) scattering in the sample. The photons generated in the sample by Raman scattering are collected by the microscope, passed through the Rayleigh rejection filter (a 532 nm edge filter) and are then be focused into the spectrometer itself. By rotating the diffraction grating, the intensity of the different scattered wavelengths are sent to the detector (Shown in the top right corner of Figure 3.8) to be measured. The programme used to control the Raman microscope is called "Wire 2.0". The laser in the Raman microscope has a wavelength of 532 nm and a power of 49 mW. The energy difference between the scattered light and that of the initial laser light is plotted by "Wire 2.0" to produce Raman spectra. For photoluminescence spectra, the same system is used as for the Raman spectra although the intensity is directly plotted against wavelength by "Wire 2.0".

By illuminating the sample with white light within the microscope the sample can be located at the position of the focused laser beam. The settings for the Raman spectral acquisition depend on the sample being investigated: Firstly, the laser power is reduced to 10% of full power (4.9 mW) in order to protect few-layer samples. The length of the energy shift scan is also sample dependent, but can be up to many hundreds of wavenumbers. And, the exposure time can be increased in the case of few-layer samples to maximise the signal to noise ratio. For typical Raman and PL spectra refer to Section 2.10

3.3.3 Computer-aided design

Once the samples have been characterised in the Raman microscope then the next stages depend on the state of the sample: whether or not a few-layer flake is connected

to thicker regions of the same material. If the flake is connected to thicker material, EBL (Section 3.3.4) will be required to isolate the flake. To explain this process, a graphene example will be used.

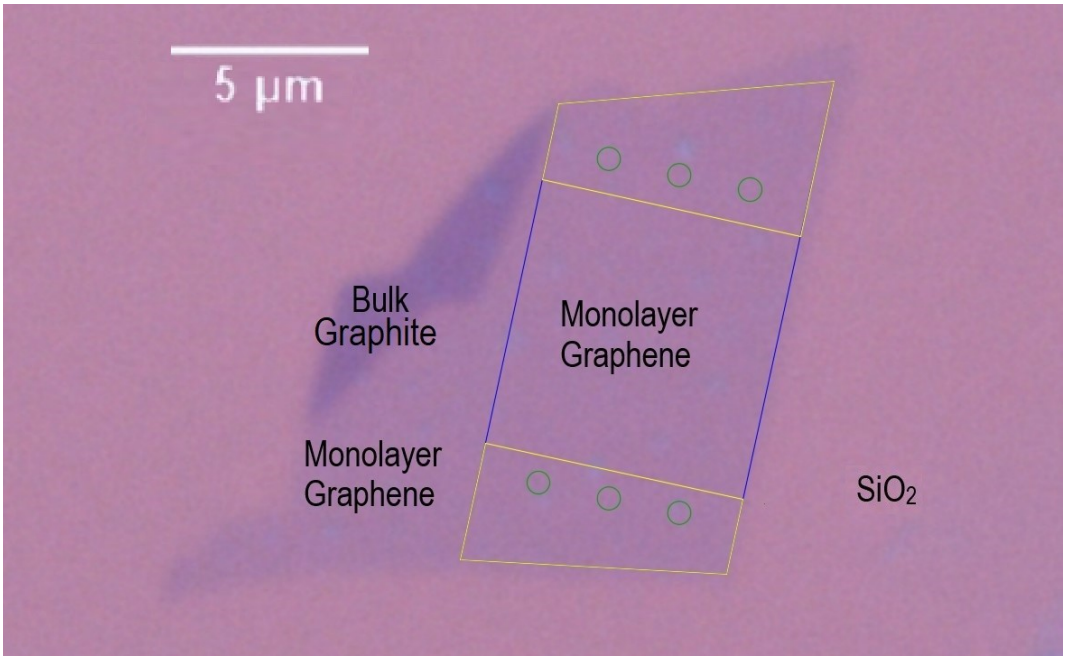

Figure 3.9: Cropped AutoCAD micrograph with active layers: protect (blue), metal (yellow) and pins (green).

To control the EBL a computer-aided design programme called "AutoCAD" is used to determine the exact shape of the final sample. This programme is also used to design the electrical contacts which are fabricated by the metallisation process, as explained in this Section 3.3.6. Firstly, micrographs of the sample are uploaded into AutoCAD. These micrographs are unlikely to be aligned and scaled correctly to the virtual template of orientation crosses on a virtual substrate, so an add-on called "autopicimport" has to be implemented. This aligns the micrographs to the virtual template by aligning the orientation crosses on the virtual substrate with those on the micrographs. Once these two images are aligned, a protect layer around the desired piece of sample is put in place (see Figure 3.9). This protected layer will remain after etching. With this protect layer it is normal to etch away the surrounding area to isolate the sample and clear the surrounding area of any debris left over from the exfoliation. The electrical contacts are then added into the design both at the edges of the sample (yellow in

Figure 3.9) and as contact pads away from the sample itself (red in Figure 3.10). There are two micrographs used at different magnifications to achieve the required precision on the sample layers (Figure 3.9) and to maintain a view of the surrounding areas for the electrical contact pads (Figure 3.10).

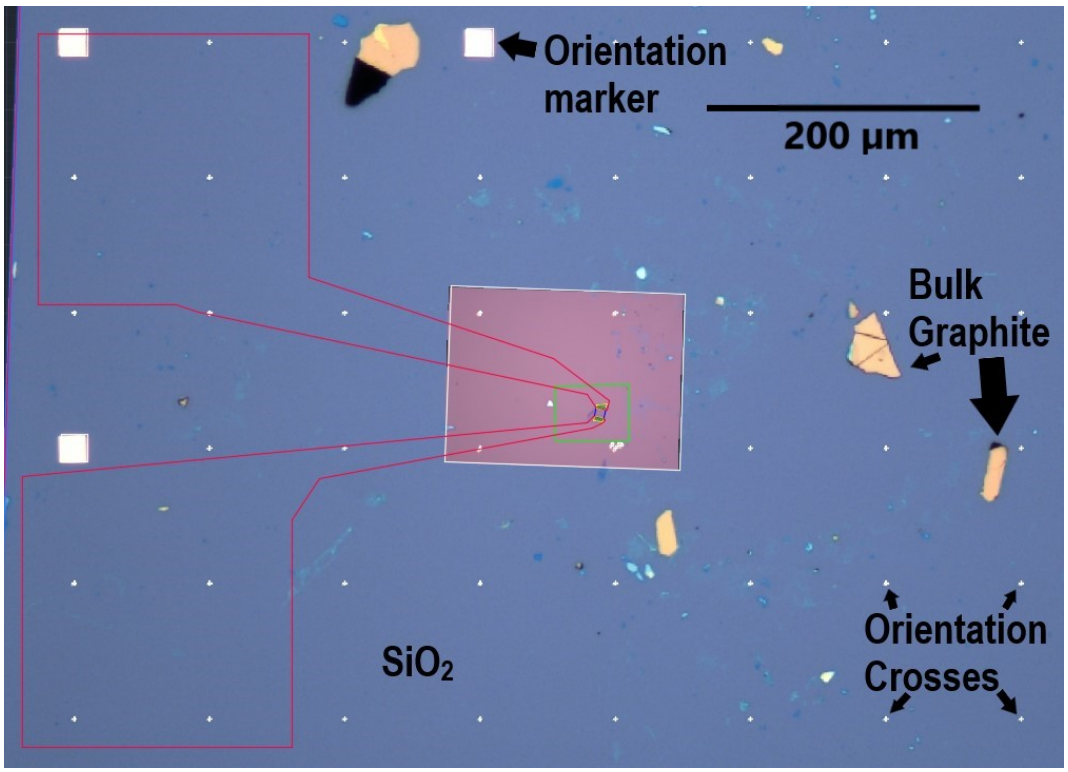

Figure 3.10: AutoCAD micrograph with the all layers active: protect (blue), etch (green), metal 1 (yellow), metal 2 (red). The pink area is that part of the image taken at a higher magnification, shown in Figure 3.9.

3.3.4 Electron-beam Lithography

The purpose of the EBL is discussed in Sections 3.2.6 and 3.2.7. An SEM consists of an electron gun, focussing lenses and electron beam deflection coils (Figure 3.11). The focused electron beam passes through the beam deflection coils which direct the beam onto the sample according to the required patterns of the AutoCAD design.

To prepare the substrates for EBL, the substrate is spin coated with PMMA as described in Section 3.2.6. The PMMA-coated sample is then loaded into the SEM (NanoBeam NB4 Electron Beam System).

The SEM system contains an electron optics control system consisting of a thermal field emission electron gun, a 100kV electron accelerator, a series of beam axis alignment coils, blanking electrodes and apertures (see figure 3.11). The thermal field emission electron gun (Fig. 3.11 (1)) is made up of a single tungsten crystal with the tip having a curvature radius of around 1 μm, the voltage of the gun is around 3 kV to stimulate the field emission. The next stage is the acceleration system (Fig. 3.11 (2)), where the electron beam is accelerated by up to 100 kV in order to create more precise designs. The beam then passes through three sets of alignment coils (Fig. 3.11 (4) and electromagnetic lenses (Fig. 3.11 (3)), each of the alignment coils consists of two coils generating a perpendicular magnetic field compared to the electron beam path. The alignment coils slightly deflect the electron beam due to the Lorentz force in order to correct the deviation between the lenses. The electromagnetic lenses focus the electron beam in a similar fashion to how optical lenses work, although it is achieved via magnetic fields generated through coils instead of using a transparent material of a certain refractive index. The blanking electrodes (Fig. 3.11 (5)) avoid accidental drawing of the beam across the sample whilst it is being turned off and on by having a set of deflectors above and below an aperture which produce the same electric field simultaneously which bend the beam equal amounts leading to a virtual electron optical source meaning that the beam is shifted with no lag. Penultimately the beam passes through the astigmatism corrector which consists of a pair of coils. Both coils contain 4 poles and are placed at 45° from each other. These poles can correct any astigmatism of the electron beam at this stage via a magnetic field which shifts the beam into the desired shape. Finally, two more electrostatic deflectors and another electromagnetic lens are employed. The two deflectors shift the beam in opposite directions in order to align the axis of the beam and the centre of the objective lens. With all these steps completed the beam will then reach the sample.

The SEM requires a job file (Figure 3.12). This job file consists of 4 parts: global, block, pattern and write. The global section of the job file contains the positions of

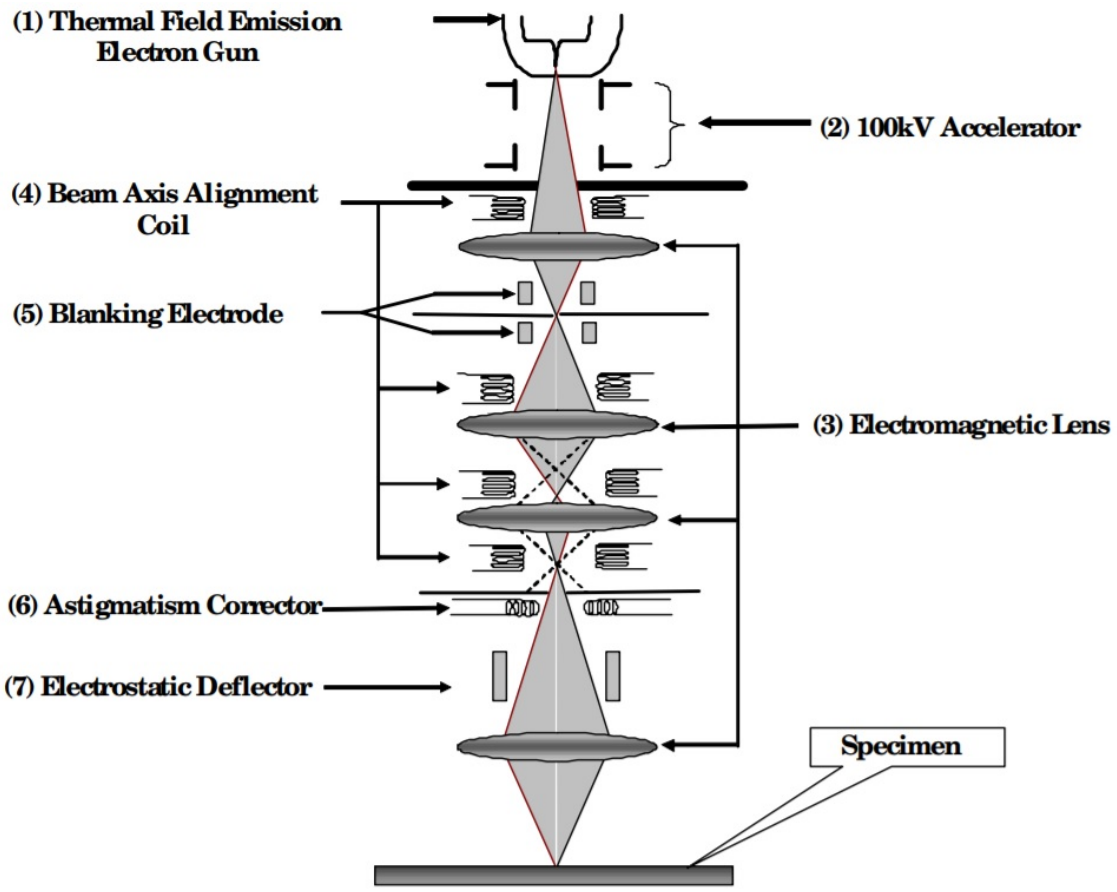

Figure 3.11: Schematic showing the main components of an SEM [75].

the allocated orientation markers (registration), the focusing procedure (in this case "map") and orientation mark shapes ("mark type"). The block section contains the EBL pattern. Any changes to orientation mark shape or registration can be made in this block section. Thirdly there is the pattern section which contains all the required information about the pattern itself. The write section contains any information related to the actual writing of the pattern, for instance the beam current. To focus the beam on the sample the SEM has a metal block known as a datum step which adjusts the height of the electron beam above the sample. Datum 1 is for the thickest samples and datum 11 for the thinnest. In this investigation datum 6 was chosen.

Once the sample is loaded into the SEM and is precisely positioned, electrons are fired at the sample in the pattern created within AutoCAD.

Once the job has been written on the sample, the sample is removed from the SEM

```
run nbwrite da250/Kyle_C/TMD_pattern_REG_NEW -1=kyle:kc1bl -2=kyle:kc1br
#-2=kyle:kc1br
#
# datum 6
#

.global
marktype sqr20
focus map
registration (0, 8 800 000) (8 800 000, 8 800 000)
registration (0, 0) (8 800 000, 0)
.end

.block
origin (0,0)
marktype sqr20
focus global_map
registration apply_global_reg
base_dose 2
pattern TMD 1 (0,0)
.end

.pattern
id TMD 1
stepsize (400000,400000)
grid (3,5)
dose_increment 0.5
filename Exeter/User/Pattern1.npf
dose 0 1.0000
.end

.write
current auto
.end
```

Figure 3.12: An example of an SEM job file displaying the different sections.

and the pattern is developed as described in Section 3.2.6.

3.3.5 Reactive Ion Etcher

The reactive ion etcher (Figure 3.13 - JLS Designs RIE 80 Etching System) functions by generating a gas of ionised particles within a chamber in which the sample is placed. The chamber is initially pumped down to a pressure of 5 mT and then the process gas is introduced into the chamber. The process gases employed were argon or oxygen. The samples are placed on the base plate which is held at a high voltage. This ionises the gas and the ionised atoms are attracted to the base plate causing a kinetic "sand-blasting" effect on the sample.

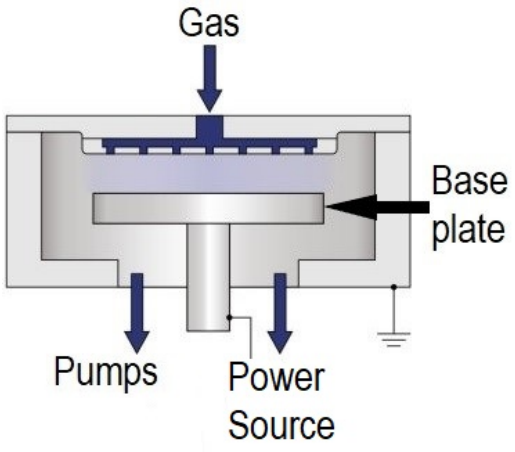

Figure 3.13: Schematic of the main chamber of a reactive ion etcher [courtesy of Oxford Instruments]

As shown in figure 3.13 the base plate is powered to cause the attraction of the charged particles. The ionic gas comes in from above, when in use there is a small window which a slight glow can be observed to make sure the RIE is working.

The RIE has first to be cleaned by running an oxygen process (20 sccm O_2, 50 mT, 50 W, 4 minutes) whilst it is empty. Once the chamber has been cleaned, the chamber is vented to ambient pressure and opened for the samples to be positioned on the base plate. The chamber is then closed again and the desired process is run. Typical process parameters are given in Section 3.2.6 for an argon etch. Finally, the samples are removed by reversing the loading steps.

3.3.6 Metal Evaporator

In order to add electrical contacts to the samples, an evaporator (Auto306 Thermal Evaporator) was used to evaporate metals onto the samples. It consists of three main parts: baseplate, vacuum system and the main control system. The evaporator, shown in Figure 3.14, functions by having metal "boats" inside its vacuum chamber through which a current is passed. These "boats" contain the metal to be evaporated, which melts and eventually evaporates, as a result of the electrical heating produced by the current. Once the metal has evaporated there is an even spread of the metal atoms around the vacuum chamber.

The baseplate hangs from the top of the vacuum chamber. It has a lot of different pins which can hold a variety of different samples in place. Once the sample is securely loaded onto the baseplate and before reclosing the chamber, the boats which contain the metals to be evaporated must be checked and refilled if necessary.

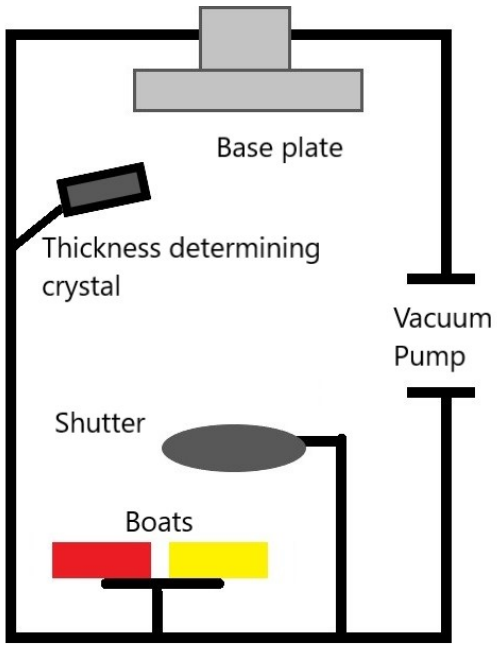

Figure 3.14: Schematic of the evaporator chamber with the gold boat (yellow) in the active position and the chromium boat in reserve with the shutter in the off position.

The chamber pressure is pumped down to around 10^{-6} Torr and the current is slowly increased until the correct rate of deposition is attained. A "Source Shutter" is initially in place to prevent any metal atoms landing on the samples while the metal is still getting to the correct temperature. This shutter is opened once the deposition rate of 1 $\text{Å}\text{s}^{-1}$ is reached. The thickness of metal deposition is monitored via the changing vibrational resonance of a ceramic crystal which is coated in gold in the chamber. The change in the crystals resonant frequency is used to detect the thickness of the deposited metal. Once the desired thickness is reached the shutter is closed again and the power to the metal boats switched off. This process can be repeated if multiple layers of metals are required.

3.3.7 Stacking Station

The two stacking stations were built in-house to facilitate a dry transfer method of a plethora of few-layered flakes [76]. The other method for stacking 2D materials employs an intermediary soft (viscoelastic) substrate made out of PDMS. The various few-layer TMD and/or graphene flakes are exfoliated onto PDMS and then subsequently transferred sequentially from the PDMS onto a Si/SiO_2 substrate. These additional PDMS steps are where the stacking station is employed. Once the few-layer flake has been deposited onto the PDMS, the PDMS is placed upon a glass slide with the flake still on top. This glass slide is then turned upside down and placed in the holder of the stacking station. This holder can be adjusted, not only in the x, y and z directions, but it can also be tilted in order to optimise the chances of successful deposition. A schematic of the stacking station is shown in Figure 3.15a.

As the positioning of the flakes is required to be very precise (on the scale of microns) a microscope is used to align the flakes on the substrates. Fortunately, the PDMS is transparent and as it is on a glass slide the microscope can be used to look through both of these to the substrate beneath. By adjusting the focus of the microscope appropriately, the location of both the flakes and the substrate can be monitored in order to align them correctly. On lowering the PDMS, a flake can be pressed on top of a substrate or on top of a pre-existing flake already located on a substrate. When the PDMS touches the SiO_2 there is a distinct colour change, once this colour change totally encapsulates the target flake then the PDMS is raised up again. Raising the PDMS slowly ensures successful deposition of the flakes whilst if the PDMS is raised too quickly then it grips onto the few-layer flakes and this reduces the chance of successful deposition and increases the risk of tearing one of the flakes or failing to deposit the flake at all. These steps are schematically demonstrated in Figure 3.15b.

Once the PDMS and its associated glass slide has been raised it is normal to check to see if there are any defects (e.g. air pockets) present between the stacked layers. This stacking process can be repeated multiple times to create Van der Waals heterostruc-

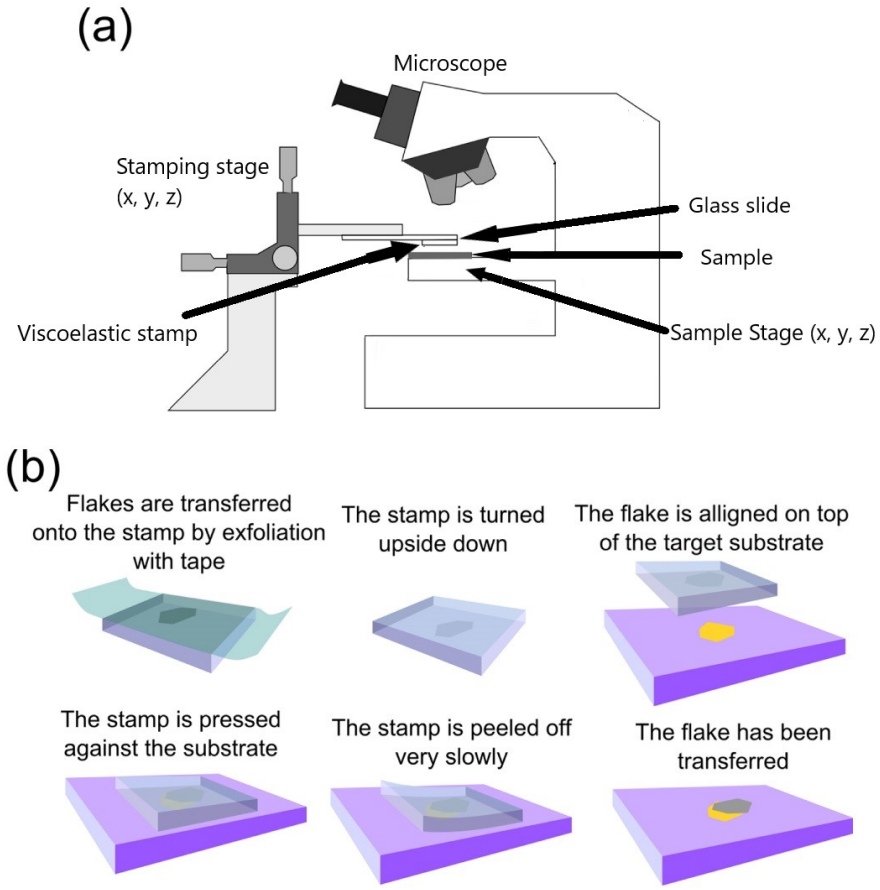

Figure 3.15: (a) Schematic of the stacking station. (b) The series of stages of stacking using the PDMS stamp and glass slide method [76].

tures [76]. One of the major current limitations with the set up used was that the stacking was undertaken in ambient conditions, ideally these stacks would take place in a vaccum chamber. To minimise risk of contamination the flakes were stored in a vacuum chamber and the time out of these storage units was minimised.

3.3.8 Lasers

As our experiments involve laser excitation the choice of TMD is partially determined by the availability of a laser whose photon energy is resonant with the bandgap of the TMD. The lasers available (with their respective wavelengths) are:

gallium arsenide (785 nm)

helium-neon (632.8 nm or 543 nm)

helium cadmium (325 nm)

argon ion (main laser lines: 488 nm or 514.5 nm)

titanium-sapphire laser - tunable between 700-1000 nm.

The Ti:sapphire laser with a photon energy range of 1.24-1.77 eV, was found to match the optical excitonic bandgap of WSe_2 (1.65 eV [74]). Although there are lasers with higher photon energies available, it has been shown that excitation with circularly polarised light with an excess of energy per photon leads to a reduction in charge carrier spin polarisation compared to resonant excitation [77].

3.3.9 Summary

This chapter has covered the techniques employed in this work, beginning with the differences in the exfoliation techniques between graphene and the TMDs, where for the latter PDMS was used as an intermediary substrate. Secondly, it explored the ways in which the thickness of the SiO_2 on the Si substrate affects the optical contrast when searching for the exfoliated flakes. After that, the characterisation techniques of Raman spectroscopy and PL spectroscopy have been discussed along with an explanation of the Raman microscope itself, which led on to a description of the graphene device using a computer aided design programme. Next, descriptions of electron beam lithography and reactive ion etching are outlined alongside the 2-stage metal deposition process onto the flakes to produce the electrical contacts. The penultimate section of this chapter has described the stacking of graphene flakes onto TMD flakes. Finally, this section considered a list of the available lasers and the importance of their wavelengths in choosing the right TMD material for SHE/VHE experiments.

Chapter 4

Results and Discussion

4.1 Introduction

This chapter presents the results of this research project. First, a description of the results of exfoliating flakes of both graphene and the TMDs is given and then the changes in the optical contrast of these flakes on Si/SiO_2 substrates with layer thickness is discussed. As explained Section 3.2.3, characterising few-layer flakes via optical contrast alone is not only difficult but also unreliable. Raman and photoluminescence spectroscopy were thus employed to confirm the layer number assignation. Next the contacted graphene device fabricated for strain measurements is described. With the difficulties in creating good ohmic contacts to the TMDs, we propose a new TMD contact design which still leaves space for a laser beam to access the TMD flake and is thus applicable to the SHE induced voltage measurements. Finally, as this device design includes using graphene as an intermediary contact, we describe our attempts to stack graphene onto a TMD flake.

4.2 Exfoliation and Optical Contrast

My first attempts to mechanically cleave graphene were unsuccessful. This was attributed to not pushing the adhesive tape on which the graphene flakes were adhered

onto the Si/SiO_2 substrate in a uniform manner. Once care was taken to apply a direct uniform force between the tape and substrate, many more few-layer flakes were attained. The flakes were found by systematically searching through an optical microscope, row by row across the substrates. At this stage, the only indication of the thicknesses of the flakes was the optical contrast between the Si/SiO_2 substrate and the flakes, as described in Section 3.2.3. Although the contrast difference is only 9% for monolayers, these are still detectable by eye as can be seen in Figure 4.1), Raman spectroscopy is however, required to confirm definitively the assignation of the number of layers made by optical contrast.

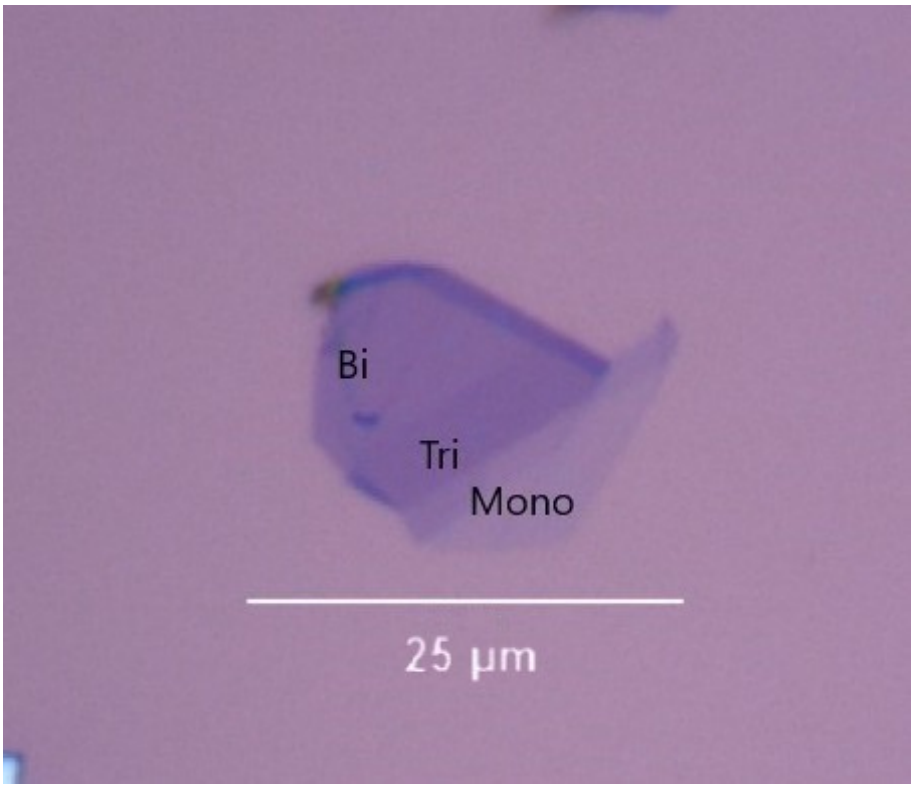

Figure 4.1: Optical micrograph of a graphene flake of multiple thicknesses: monolayer, bilayer and trilayer.

Figure 4.1 shows how the multiple thicknesses of graphene in a single flake are distinguishable by optical contrast. This figure demonstrates the subtlety in the change in contrast as layer number increases. The unlabelled top edge of the flake in Figure 4.1 shows even greater contrast than the rest of the flake indicating that it is clearly even thicker than any of the rest. Once the technique of exfoliating monolayers of graphene

was mastered, a slightly modified version of this technique was then applied to TMDs, just with the number of peels of the adhesive tape reduced from the 10-15 for graphene down to five for TMDs. However, this technique proved unsuccessful with the TMDs as no viable flakes were deposited onto the Si/SiO_2 substrates. Instead the next method as described in Section 3.2.2 of using PDMS as an intermediary substrate to then stamp the flakes onto the SiO_2 proved to be much more successful. WSe_2 was exfoliated successfully, producing high quality flakes, as can be seen in Figure 4.2.

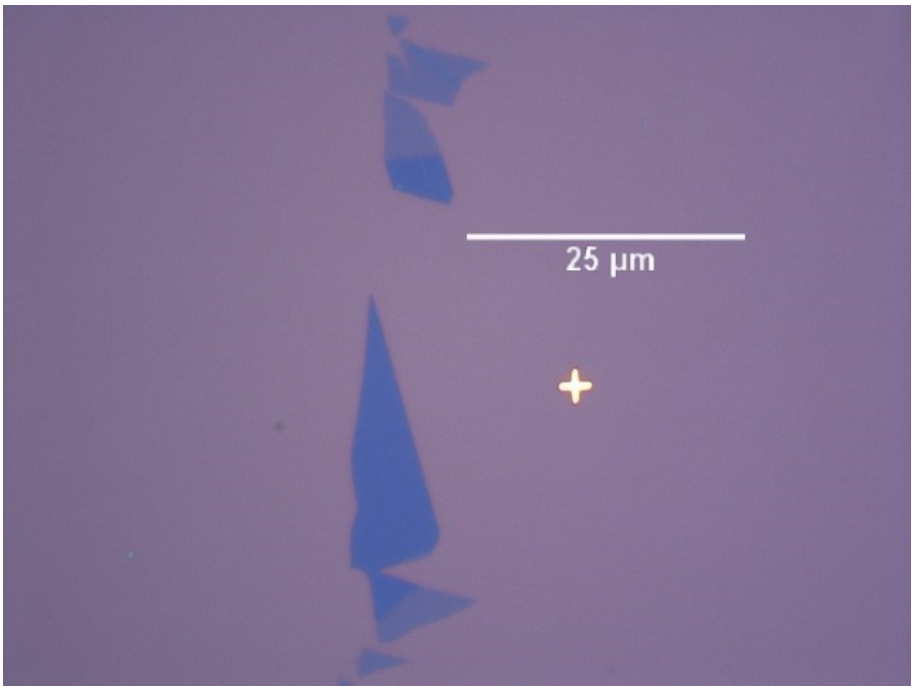

Figure 4.2: Micrograph of two flakes of WSe_2 with both multilayer and monolayer sections.

When flakes such as the lower one shown in Figure 4.2 have a monolayer attached to a multilayer the latter can be etched away as described in Section 3.2.6.

Exfoliating MoS_2 using the same method as WSe_2 proved equally effective: the resulting exfoliated flakes of MoS_2 proved to have the similar optical contrast as WSe_2 as can be seen later in this chapter.

30 days after exfoliation the WSe_2 flakes appear to be disappearing optically. Although this has been reported previously in $MoTe_2$ [50] with the phenomenon being attributed to oxidation, to the best of our knowledge, WSe_2 behaving similarly has not

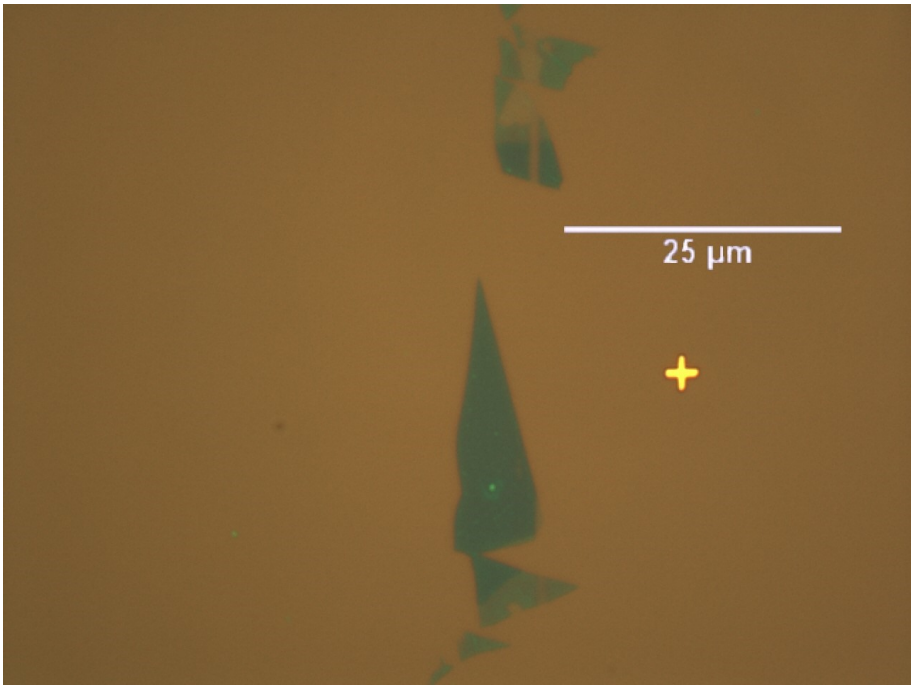

Figure 4.3: Optical micrograph of the WSe_2 flakes 30 days after exfoliation.

been previously reported. This will be discussed further in Section 4.3 of this chapter.

Once these flakes were identified optically, the Raman microscope was used to collect both Raman and photoluminescence (PL) spectra from the flakes to confirm whether or not they are really monolayers.

4.3 Raman and photoluminescence spectra

4.3.1 Raman spectrum of graphene

Raman spectroscopy is a well established technique to identify monolayer graphene flakes. As discussed in Section 2.10 the two main peaks in Figure 4.4 correspond to the G peak (1580 cm^{-1}) and the G' peak (2700 cm^{-1}). In Figure 4.4 the G' peak is 3.49 times more intense than the G peak which agrees with the literature [60] that it is a Raman spectrum of monolayer graphene. Furthermore, the G' peak consists of a single sharp clearly Lorentzian.

Another point to note about the spectrum of Figure 4.4 is that there is no D peak (1350 cm^{-1}). As the D peak arises from defects within graphene [60], its absence

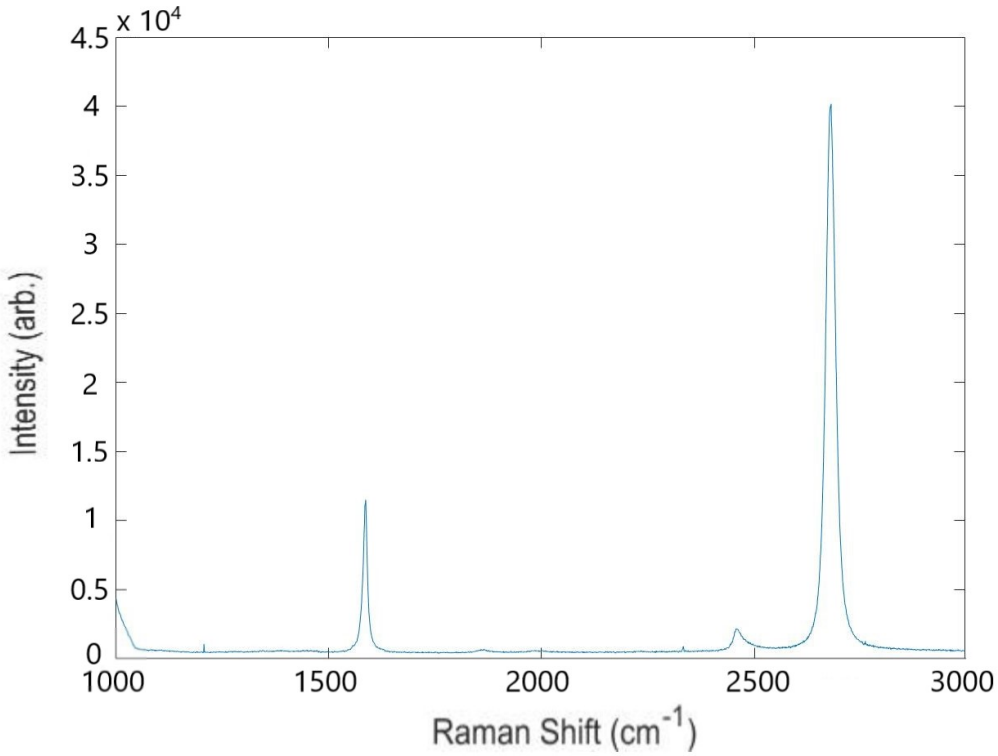

Figure 4.4: Raman spectrum obtained from the graphene flake.

indicates that the monolayer graphene flake is a single defect free crystal.

4.3.2 Raman and photoluminescence of the transition metal dichalcogenides

Raman spectroscopy is also used for characterisation of TMDs:

Molybdenum disulphide

As discussed in Section 2.10 there are two main peaks in the Raman spectrum of MoS_2 – for bulk MoS_2 these E^1_{2g} and A_{1g} peaks are located at 383.5 cm^{-1} and 408.7 cm^{-1}, respectively [63], i.e. they have an energy separation of 25.2 cm^{-1}. As the layer number is decreased these two Raman peaks shift closer together [63].

Table 4.1 gives the energy of the Raman peaks of the MoS_2 flakes measured in this work (Figure 4.5) compared to those in the literature. The Raman spectra were produced using a laser with a wavelength of 532 nm and the MoS_2 flakes were supported

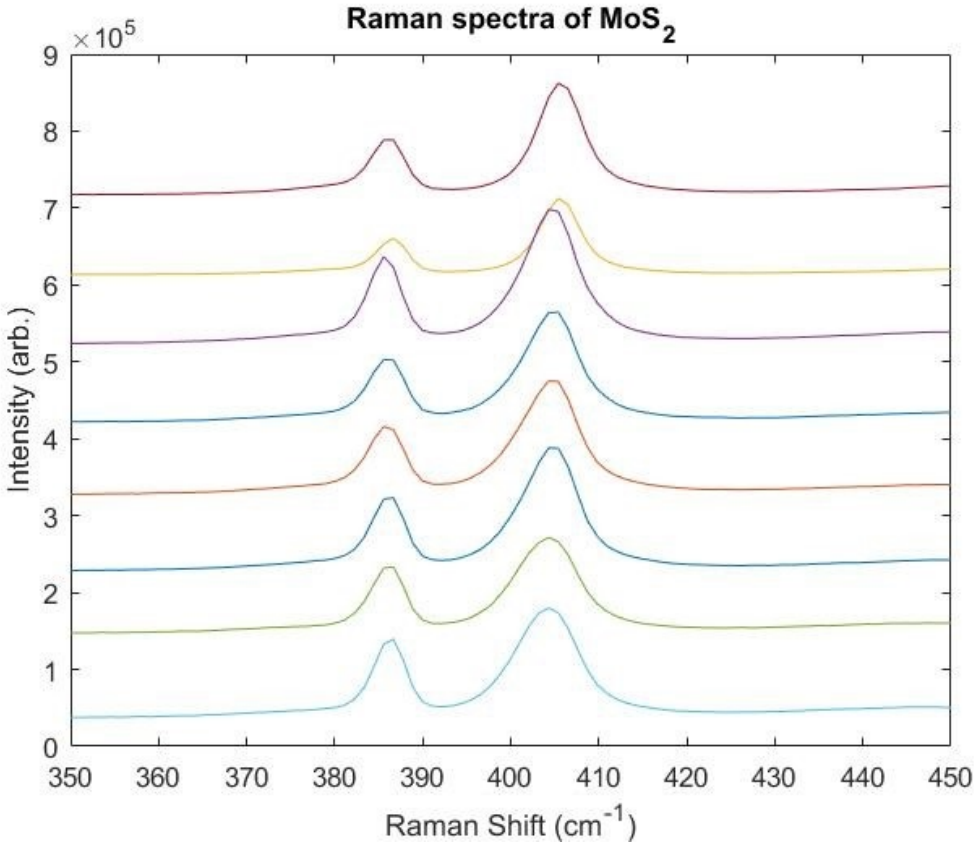

Figure 4.5: Raman spectra of multiple flakes of MoS_2 in order of peak difference, with the lowest peak difference at the bottom (offset for clarity).

MoS_2 sample	E^1_{2g} (cm^{-1})	A_{1g} (cm^{-1})	Difference (cm^{-1})	suspected layer number
Zeng [78]	383.61	401.39	17.78	1
Li [63]	384.7	402.7	18	1
Sample 1*	386.07	404.07	18	1
Sample 2*	385.71	403.71	18	1
Sample 3*	386.21	404.28	18.07	1
Sample 4*	385.45	404.14	18.69	2
Sample 5*	385.67	404.42	18.75	2
Sample 6*	385.52	404.56	19.04	2
Sample 7*	385.33	405.67	19.34	2
Sample 8*	385.93	405.58	19.65	2
Zeng [78]	383.54	404.44	20.9	2

Table 4.1: MoS_2 peak positions and suspected layer number of flakes from this investigation and literature.

on Si/SiO_2 substrates in all cases. Zeng *et al.* [78] claims that if the energy separation of the E^1_{2g} and A_{1g} peaks is between 17.78 - 18.00 cm^{-1} then the flake is a monolayer.

The literature is however, far from unified on this question with values for the peak separation in monolayer MoS_2 ranging between 17.78 cm^{-1} and some reports saying that peak separation of under 20 cm^{-1} is sufficient for the monolayer MoS_2 [63]. Our results show that these criteria may not be enough in themselves to determine definitively whether or not a TMD flake is a monolayer or a bilayer. The separation of the two Raman peaks shown in Figure 4.5 does not vary distinctly enough with layer number. Thus, Raman spectroscopy by itself appears to be much more ambiguous compared to Raman spectroscopy of graphene in distinguishing a monolayer from a bilayer, where for graphene there is a very distinct change in the Raman spectrum [7]. With optical contrast and Raman spectroscopy both inconclusively identifying TMD layer numbers, results, photoluminescence is also required to distinguish definitively the layer number in a TMD flake.

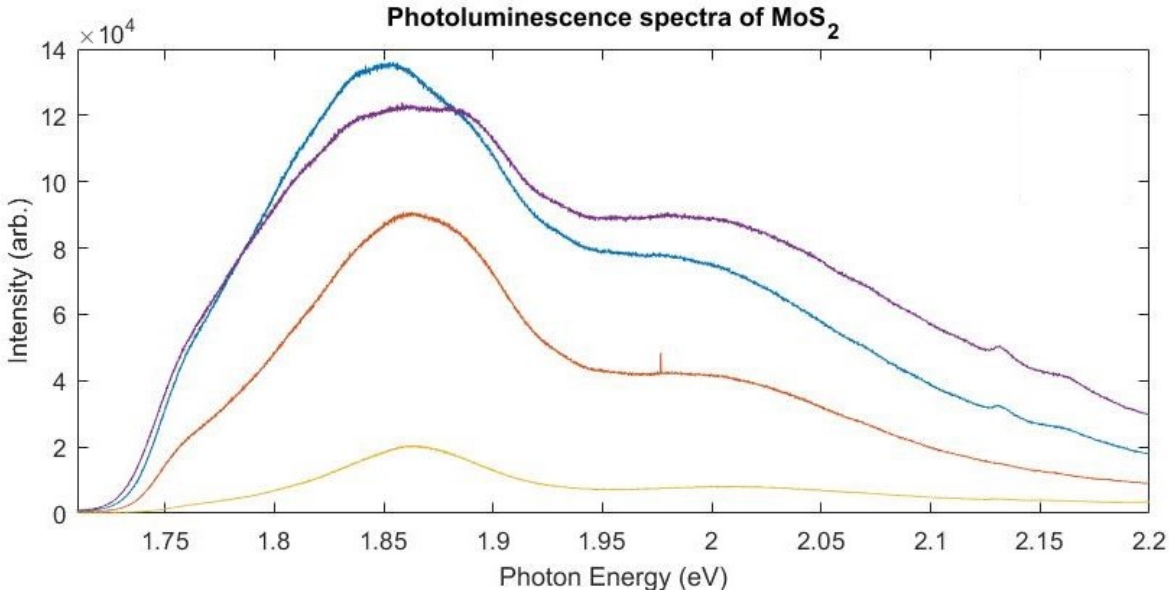

Figure 4.6: Excitonic photoluminescence spectra of MoS_2 flakes, the different curves are for the different flakes measured

As TMDs are reduced in layer number to a monolayer and they become a direct band-gap semiconductors, their PL intensity increases strongly [35]. Figure 4.6 shows PL spectra of MoS_2's A and B excitons (described in Section 2.10)with peaks around 1.85 eV and 2.00 eV, respectively. The B peak is visible in the spectra as the laser used for these measurements (532 nm $\equiv$ 2.3 eV) was quasi-resonant with these excitonic

transitions [79]. Although this does support that the number of layers in the MoS_2 flakes of Table 4.1 are likely to be correctly assigned, further evidence such as an investigation of the intensity and energy position of the indirect I PL transition [35] is needed to confirm the layer number for certain. The I peak is located at 1.59 eV for bilayer MoS_2 [35]. The Raman microscope used in this work unfortunately did not stretch this low in energy and therefore this peak could not be investigated. Other commercial Raman microscopes are able to measure this energy range but one was not available in the time frame of this project.

Tungsten diselenide

The Raman spectrum of a monolayer WSe_2 flake is given in Figure 4.7. The main peak of Figure 4.7 at 250 cm^{-1} is attributed to the degenerate E^1_{2g} and A_{1g} modes [66].

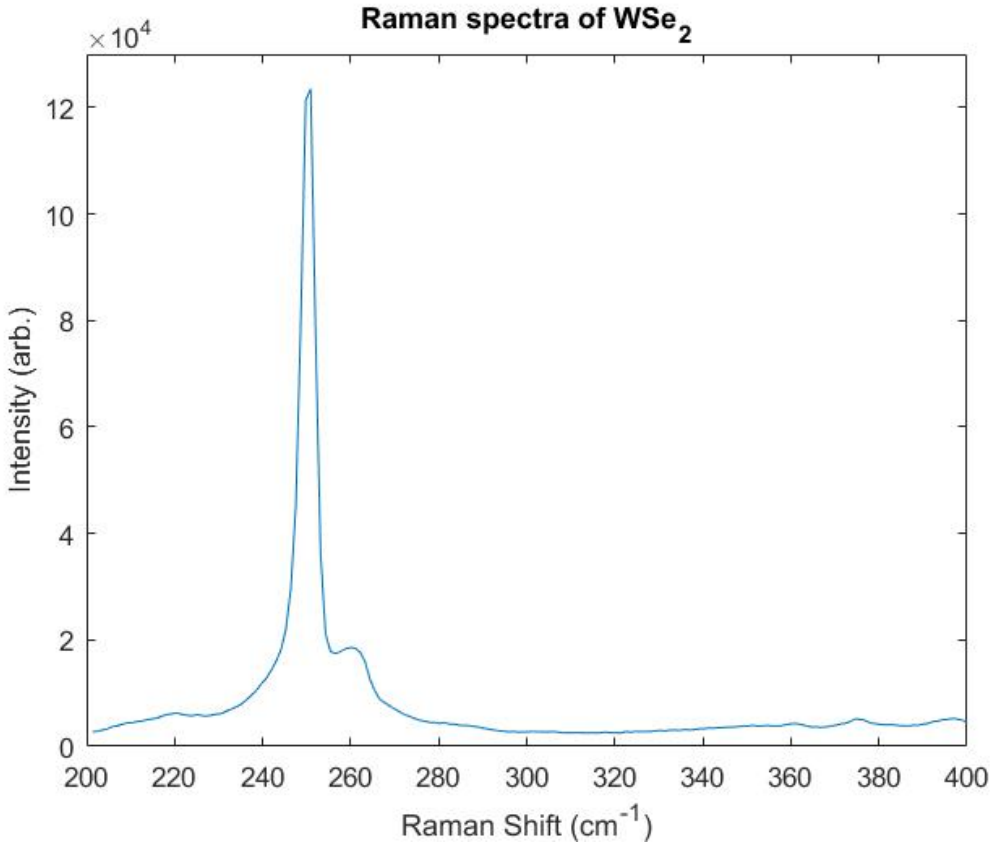

Figure 4.7: Raman spectrum of monolayer WSe_2 Flake A

The spectrum of WSe_2 in Figure 4.7 is lacking the peak located at 310 cm^{-1} which, as

described in Section 2.10, signifies multilayers of WSe_2 [66], thus confirming WSe_2 Flake A a monolayer. In the Raman spectrum in Figure 4.8 although the most-prominent Raman peaks are little changed from those of Figure 4.7 an extra interlayer mode is apparent at 310 cm^{-1}, showing that this WSe_2 flake has at least two layers.

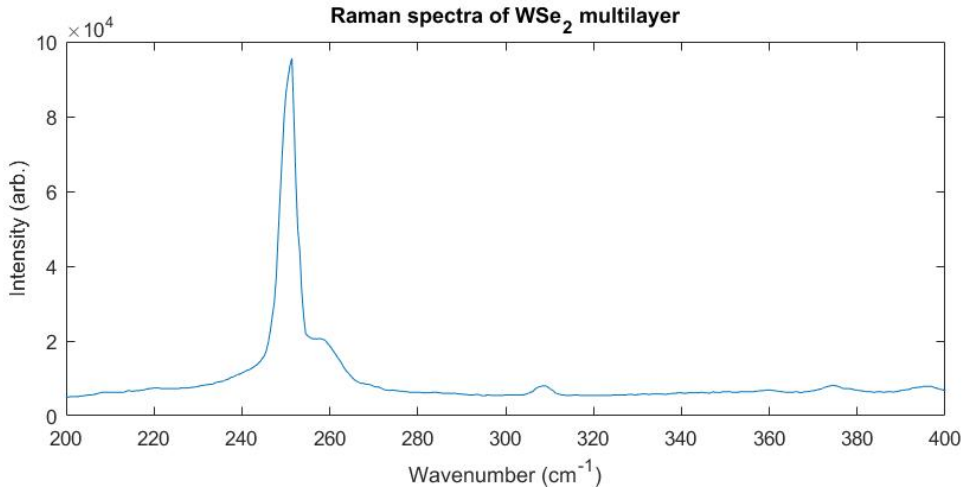

Figure 4.8: Raman spectrum of a multilayer flake of WSe_2

Figure 4.9 the PL spectrum of WSe_2 Flake A: spectrum 1 was taken 12 days of exfoliation, while the PL spectrum 2 was taken 42 days after exfoliation. The intensity of the PL peak has been heavily supressed in spectrum 2. As the same parameters used with the Raman microscope, this change in PL intensity was unexpected. Chen *et al.* [50] have shown the change of $MoTe_2$ due to oxidation by the visibility of the flakes decreasing over time but the Raman spectra remain unchanged. To the best of our knowledge we are unaware of any similar phenomena reported for WSe_2 under ambient conditions.

Yamamoto *et al.* [80] WSe_2 to ozone at temperatures below 100°C causing the selenium atoms to be replaced by oxygen which led to the uppermost layer becoming tungsten oxide. We kept the laser power low 3 mW and minimised exposure times whilst we measured the Raman and PL spectra to reduce any potential oxidation being caused by the laser. Laser induced oxidation would anyway only occur at the laser spot location on the flake rather than throughout the flakes as observed in Figure 4.3. Thus we believe that we have observed, for the first time, WSe_2's environmental (time-

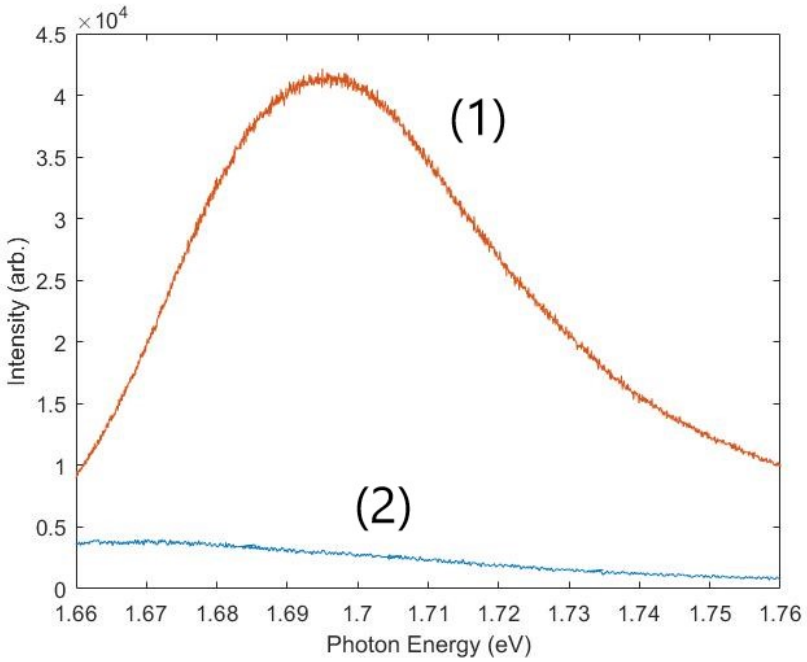

Figure 4.9: PL spectrum of WSe_2 Flake A taken (1) 12 days after exfoliation and (2) 42 days after exfoliation

dependent) instability to oxidation even though WSe_2 Flake A was always stored in a vacuum in a similar manner to that reported for $MoTe_2$

From these results, characterising graphene was quite conclusive whilst in the TMDs there is an uncertainty. In the case of MoS_2 there is another peak in the PL spectra attributed to the indirect transition located at 1.59 eV [35]. The Raman microscope used in the measurements in this thesis did not have the range to go this low in energy and therefore this peak could not be found. Recently another Raman microscope became available at the University of Exeter which has a range that encompasses the I peak but as it was not used in this investigation it is beyond the scope of this thesis although is definitely useful in future research.

4.4 Graphene device for strain measurements

In this section, the fabrication of a contacted graphene device designed for strain measurements will be described.

Monolayer graphene Flake A shown in Figure 4.10 was chosen due to its relatively

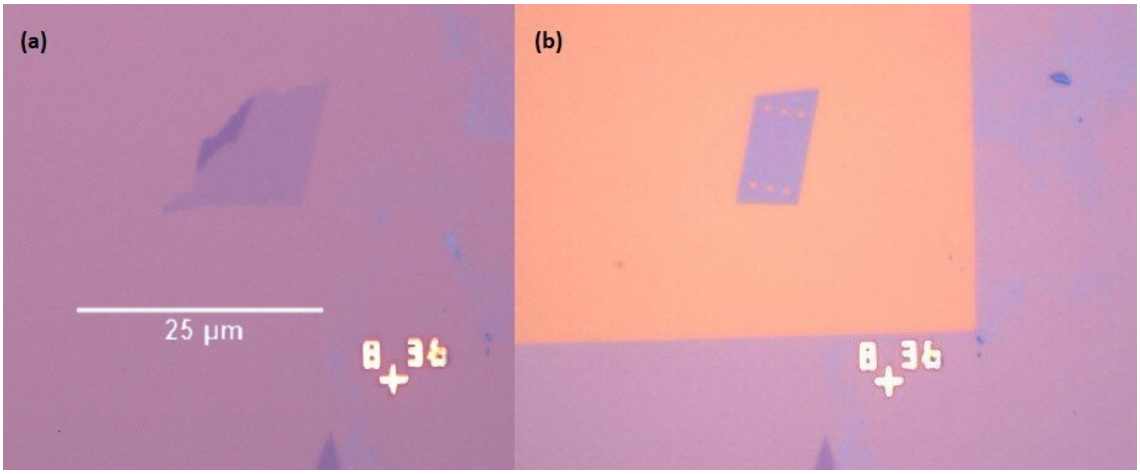

Figure 4.10: (a) Optical micrograph of Graphene Flake A. (b) Graphene Flake A after etching, the lighter region is where the pattern has etched away the SiO_2

large size. The AutoCAD design involving pinned chromium gold contacts is explained and described in Section 3.3.3 and depicted in Figure 3.10. Graphene Flake A was e-beamed as described in Section 3.2.6, etched as described in Section 3.2.6 and metallised as described in Section 3.2.7 The result shown in Figure 4.11. The pins were 300 nm in diameter, they were spaced 1.2 μm apart and located 1.5 μm from the outer contact edge.

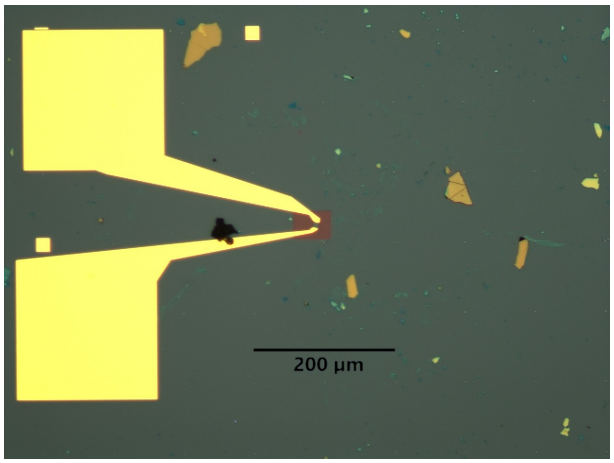

Figure 4.11: Graphene with gold contacts with the wires and contact pads (with chromium underneath)

Once the first gold layer for the graphene contacts had been evaporated, the sample was e-beamed (Section 3.2.6 and metallised (Section 3.2.7) again to create wires and contact pads which can be seen in Figure 4.11. Both wires and pads were first metallised

with chromium as it adheres to the SiO_2 better than gold and then the gold is evaporated on top of the chromium layer. The square contact pads are 200 μm $\times$ 200 μm in size. This graphene device has yet to be employed in strain measurements.

4.5 Transition metal dichalcogenide device design for spin-Hall effect voltage measurements

This section proposes a device design for measuring the transverse voltage produced as a result of the SHE. The main challenge is in creating ohmic contacts to the TMDs as discussed in Section 2.9. With gold having a calculated Schottky barrier height of 0.62 eV to MoS_2 [54], Mak *et al.*'s [21] were very fortunate that the Schottky barriers of their gold contacts did not impede their measurement of the VHE in MoS_2. As the SHE signal is much smaller than that of the VHE, especially in n-type TMDs, reliable ohmic contacts are essential to distinguish the SHE component of the transverse voltage from the VHE component.

The key parameters in designing a device to measure the SHE in TMDs were (i) choose the optimal TMD and (ii) to create ohmic contacts whilst keeping a large part of the TMD flake exposed for the laser beam to reach it unimpeded. The reasons behind choosing WSe_2 are given in Section 2.9. Our proposed contact design is depicted in Figure 4.12.The design consists of a WSe_2 flake with graphene stacked on top at the edges, on the overlapping regions, h-BN is stacked on top then gold is deposited to act as a local top gate, finally palladium contacts will be deposited on the edges of the graphene. We propose using graphene as an intermediary contact as it has been shown to reduce the Schottky barriers of contacts to the TMDs [22, 56, 55]. The Schottky barriers can be further reduced by doping the graphene to smooth the gap between the work function of the contact metal and the charge carrier affinity of the semiconductor [52]. Various approaches have been employed to dope the graphene intermediary. These are reviewed in Section 2.9 The contact design shown in Figure 4.12 uses electric field-

effect doping by top-gating the graphene contacts where they overlap the TMD. This design is based on the gated local contacts described in Wang *et al.*'s work.

Figure 4.12: Schematic of the proposed contact design for contacting to WSe_2. With SiO_2 denoted in purple, WSe_2 denoted in blue, graphene in grey, h-BN in red, gold in green and the yellow denotes palladium.

By implementing field-effect doping of the contact regions, the graphene can be doped very precisely and adjusted to fine tune the Fermi level, retaining this doping indefinitely. Although Sata *et al.* do not report using the same electric field effect doping technique with $NbSe_2$ as an intermediary contact, this could be a potential refinement to our contact design, but due to $NbSe_2$ instability in air this would necessitate encapsulating the whole device in h-BN [58].

4.6 Stacking

For the design proposed in Figure 4.12 to be fabricated, stacking graphene onto TMDs is essential. Here we describe the two different stacking approaches attempted and review some of the difficulties encountered. The equipment used and general stacking technique are described in detail in Sections 3.3.7 and 3.2.8 respectively. The two approaches attempted were (i) to consecutively stack the graphene onto the TMD flake one piece at a time and (ii) to exfoliate graphene multiple times onto PDMS to produce an arrangmeent of graphene flakes of the appropriate size that could be stamped onto the TMD flake in a single deposition step. The TMD flakes chosen for stacking were the largest available in order to facilitate the stacking procedure as much as possible.

A dry stamping which involved exfoliating graphene onto PDMS before stamping it onto a TMD flake on the Si/SiO_2 substrate was employed. The technique attempted

first was the simultaneous stacking of multiple appropriately arranged graphene flakes onto the TMD. This attempt at dry transfer was partially successful in that the graphene released properly from the PDMS, but the positioning of the two graphene flakes relative to the TMD flake was incorrect (Figure 4.13). In Figure 4.13, it can be seen that the graphene flake on the left is taking up too much of the TMD flake while the graphene on the right-hand side of the flake has missed the target TMD flake altogether and is instead stacked on a much smaller adjacent flake.

Figure 4.13: Optical micrographs of the MoS_2 flake through the stages of stacking: (a) pristine MoS_2 flake before stacking, (b) desired stacking positions on the flake marked in red, (c) two graphene flakes stacked onto the MoS_2 flake.

This dry stamping technique involves the PDMS being lowered at a slight angle compared to the Si/SiO_2 substrate in order to assist with the release part of the procedure once the PDMS has been pressed onto the TMD flake. The drawback of this slight angle is that one side of the PDMS touches the substrate first. With the PDMS being very flexible, this leads to the graphene flakes moving their location as the PDMS is lowered further. It is thought that this change in location only occured during the very final lowering of the PDMS just as the PDMS closest to the graphene flakes became compressed. By the time this shift in location of the graphene flakes was noticed, it was too late to adjust their position as a fast pull upwards of the PDMS would have risked damaging the TMD flake. The desired positions are shown in Figure 4.13 to demonstrate the lack of accuracy of the stacking station. It should also be noted that

the colour of the graphene flakes in Figure 4.13c is not homogeneous. The lighter areas of the graphene flakes are bubbles of air which have been trapped under the graphene layers.

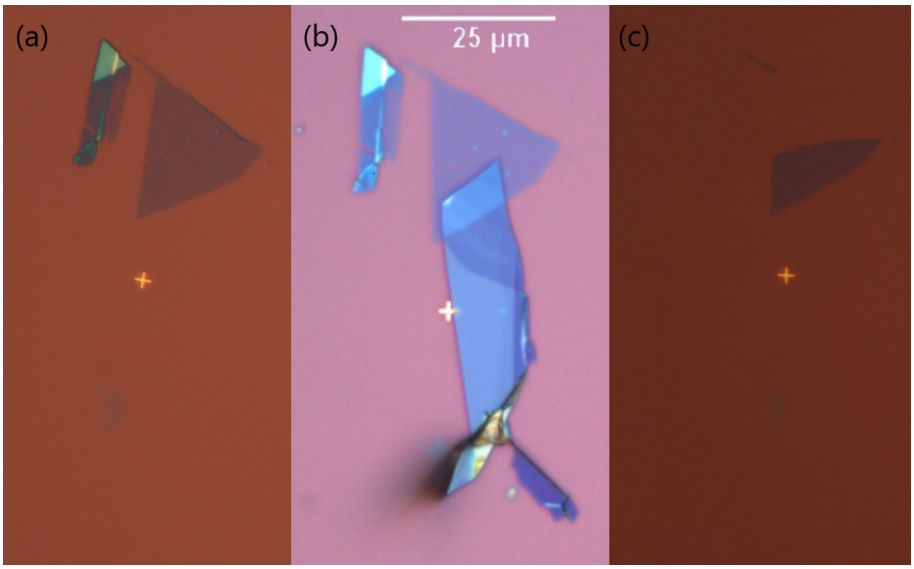

Figure 4.14: Optical micrograph of MoS_2 Flake S2 (a) before stacking, (b) after the first stack and (c) after the failed stack.

The second stacking technique employed was the consecutive stacking method: the first stack shown in Figure 4.14b was relatively successful with the graphene being placed in the desired position on the TMD flake. On deposition of the second flake onto the TMD flake, the TMD flake was ripped and removed sections of both the TMD and graphene flakes from the Si/SiO_2 substrate (Figure 4.14). This picking up of previously deposited flakes is a risk each stack attempt when using the dry transfer technique.

From these results of stacking graphene onto TMDs it can be shown that both methods have their own drawbacks: Stacking multiple flakes of graphene in one deposition step can be more difficult as the graphene flakes need to be located on the PDMS in the correct arrangement, whilst consecutively stacking the flakes in multiple deposition steps leads to a higher risk of damaging the sample. Very recently a new stacking station has been built at the University of Exeter, equipped including a proper microscope rather than just a camera attachment, meaning more precise and reactive

controls, meaning that stacking accuracy and precision should improve.

4.7 Summary

This chapter has covered the results of this work. The exfoliated graphene and TMD flakes were presented with their optical contrast, the change in optical contrast of WSe_2 over time was noted. This chapter discussed the Raman spectra used to characterise the graphene and TMD flakes before describing the PL spectrum gathered to further confirm the characterisation of the TMD flakes. Once the change in optical contrast was observed, another PL spectrum of WSe_2 was recorded which had a much lower intensity than the previous spectrum. Next, the graphene device fabricated for future strain measurements was presented, but no measurements were taken. This chapter proposed a new device design which may provide good ohmic contacts to WSe_2 and still leaves an exposed for a laser beam to access the TMD flake, making it appropriate for measurements of the SHE induced voltage. Lastly this chapter discussed the results of our attempts at stacking graphene flakes on TMD flakes.

Chapter 5

Conclusion and future work

5.1 Introduction

This chapter first summarises the progress made in this project. The latter half of this chapter suggests steps to be taken in future to measure the SHE in TMDs.

5.2 Progress

In this thesis, we have reported the progress made in creating TMD devices to measure the transverse spin voltage produced by the SHE under circularly polarised optical excitation. Although this has been measured previously in TMDs [21], the measured Hall voltage was attributed to the VHE instead of the SHE. Furthermore, the results attained by Mak *et al.* [21] have not been reproduced by other research groups and due to the large interest in creating ohmic contacts to TMDs, it seems that this hurdle needs to be overcome before further measurements of the SHE in TMDs can be undertaken.

Firstly, deciding which TMD would be the best candidate for measuring the SHE as opposed to the VHE, relied on a number of factors: The main variable determining the relative strength of the SHE compared to the VHE in TMDs is the position of the Fermi level [13]. When the Fermi level lies between the spin-split valence bands of the TMD at the Dirac point, the SHE is equal in magnitude to the VHE [13]. By

choosing the TMD with the largest spin splitting in the valence band, implies that it has the largest SOC and hence will exhibit the strongest SHE. Out of the TMDs stable in atmospheric conditions, WSe_2 has the largest spin splitting in the valence band (as shown in Table 2.1). In order that Fermi level lies in the valence band of the TMD it is advantageous if the TMD is naturally p-type doped in the first place. Again WSe_2 is the only TMD which fulfils this requirement out of all of the atmospherically-stable TMDs. In addition, the optically excitonic band gap of WSe_2 (1.64 eV [81]) matches the wavelength of the titanium sapphire laser, and as it has been shown that resonant excitation enhances charge-carrier spin polarisation [77] it is clear that WSe_2 is the best candidate for the SHE experiment.

From the results of the Raman spectra (discussed in Section 4.3), it appears that we have successfully exfoliated monolayer MoS_2 and WSe_2 flakes. By using PDMS as an intermediary substrate when exfoliating these TMDs, we attained a much higher yield of monolayer and few-layer flakes than when we deposited the flakes directly from the adhesive tape onto the Si/SiO_2 substrates. With Raman spectroscopy of the WSe_2 flakes we have been able to distinguish the monolayers from the few-layer flakes by detecting the presence or not of the Raman peak at around 310 cm^{-1} [66]. Characterising the MoS_2 flakes has proven to be more difficult as the energy separation of the A_{1g} and E^1_{2g} Raman peaks alone did not definitively distinguish between the monolayer and few-layer flakes. However, detecting the indirect-transition I PL peak which only occurs in the PL spectra of few-layer MoS_2 and WSe_2 flakes, it should be possible to distinguish a monolayer from a multilayer flake. One unexpected result was the diminishing optical contrast of the WSe_2 flakes over a matter of four weeks. WSe_2 has been thought to be environmentally stable under ambient atmospheric conditions, but our results seem to contradict this. We tentatively attribute this change in optical contrast and the apparently corresponding decrease in the excitonic PL intensity from these WSe_2 flakes to be due to oxidation. Finally, we have successfully exfoliated and characterised monolayer graphene on Si/SiO_2 substrates by both Raman spectroscopy

and optical contrast.

The next step was to create good electrical contacts to our TMD flakes by trying to minimise the Schottky barriers that arise between the metal contact and the TMD. There have been multiple attempts in the literature to optimise electrical contact to TMDs [22, 56, 82, 53], with some even reporting the attainment of very low Schottky barriers [58]. One of the main drawbacks of many of these approaches, is that the TMD flakes are either covered by a top gate [56] and/or the doping used to improve the contact resistance is only temporary [53]. Our contact design given in Figure 4.12 on the other hand utilises field-effect doping of graphene intermediary contacts whilst the device design also provides access by a laser beam to the centre of the TMD flake. This is the basis of the future work suggested below.

5.3 Future work

The future work will need to begin with a detailed investigation of our unexpected finding that WSe_2 is not after all environmentally stable under ambient atmospheric conditions. Optical contrast, Raman and PL measurements would need to be taken from exfoliated WSe_2 monolayer and few-layer flakes immediately after exfoliation and then once a day for at least four weeks to track how the suspected oxidation process progresses over time. If such oxidation repeats in every monolayer and few-layer WSe_2 sample then it may be necessary to encapsulate the WSe_2 flake between thin layers of h-BN to protect it from air. Such encapsulation would not hinder access to the flake by a circularly-polarised laser beam as the large band gap of h-BN means that it is transparent to light of photon energy close to the optical-excitonic band gap of WSe_2 (1.65 eV [81]).

Refining the technique of stacking flakes in order to reduce the chance of failure is another imperative, as depicted in Figure 4.14. With the new improved stacking station which has just been built in the University of Exeter, which incorporates a microscope, there is a good chance that a higher level of control will be achieved on

this new stacking station. The next step would be to have a stacking station which could operate in a vaccum to avoid trapping air between the layers. We propose to use palladium as the metallic part of the electrical contact to WSe_2 with graphene as the intermediary contact, see Figure 4.12. The device design will be similar to that of layout as Mak *et al.* [21], shown in Figure 2.11b. By aligning the Fermi level to between the spin-split valence bands of WSe_2 using a back gate and illuminating the flake with circularly-polarised laser light whilst passing a current through the flake, a resultant transverse voltage caused by the SHE and VHE should be measurable. By first measuring this transverse voltage with the Fermi level located between the spin-split valence bands of WSe_2 and then adjusting the Fermi level to be below the spin-split valence bands of WSe_2 and remeasuring the transverse voltage would be a clear test of Xiao *et al.'s* [13] theory of the relative strengths of the SHE and VHE. If successful then it may be possible to repeat the experiment on positively-doped MoS_2.

Following Sata *et al.'s* [58] recent findings suggesting that $NbSe_2$ as an intermediary contact in p-type electrical contacts to few-layer WSe_2, if graphene intermediary contacts still turn out to possess Schottky barriers then possibly the next step might be to use $NbSe_2$ intermediary contacts instead. In the work of Sata *et al.* they still used gold as the contact metal so a potential optimisation might be to replace the gold with palladium as the latter should give rise to a smaller Schottky barrier in the first place (0.9 eV compared to 0.35 eV, respectively [54]). However, as discussed in Section 2.9 $NbSe_2$ is unstable in air and so any device incorporating $NbSe_2$ intermediary contacts would have to be encapsulated in h-BN. In addition, Sata *et al.* made no attempt to tune the Fermi level in the $NbSe_2$ and it is therefore still an open question whether this is possible.

Finally, if all attempts to produce ohmic contacts to monolayer and few-layer WSe_2 prove unsuccessful then there is always the alternative approach of imaging the SHE and VHE in WSe_2 flakes using Kerr rotation microscopy as was shown by Lee *et al.* [20] in bilayer MoS_2 and originally by Kato *et al.* [42] in bulk n-type GaAs. However,

this would allow no means to extract a transverse spin voltage from the device.

References

1. P. R. Wallace, Phys. Rev. **71**, 622 (1947).

2. K. S. Novoselov, A. K. Geim, S. V. Morozov, D. Jiang, Y. Zhang, S. V. Dubonos, I. V. Grigorieva and A. A. Firsov, Science **306**, 666 (2004).

3. J. W. Jiang, Fontiers of Physics **10**, 106801 (2015).

4. C. Lee, X. Wei, J. W. Kysar and J. Hone, Science **321**, 385 (2008).

5. http://www.matweb.com/search/datasheet.aspx?matguid=210fcd12132049d0a3e0cabe7d091eef *(last accessed 23/11/2017).*

6. A. Geim and A. MacDonald, Phys. Today **60**, 35 (2007).

7. A. Geim and K. Novoselov, Nature Mater. **6**, 183 (2007).

8. X. Zhang, X. F. Qiao, W. Shi, J. B. Wu, D. S. Jiang and P. H. Tan, Chem. Soc. Rev. **44**, 2757 (2015).

9. K. I. Bolotin, K. J. Sikes, Z. Jiang, M. Klima, G. Fudenberg, J. Hone, P. Kim and H. L. Stormer, Solid State Comm. **146**, 351 (2008).

10. H. Schmidt, F. Giustiniano and G. Eda, Chem. Soc. Rev. **44**, 7715 (2015).

11. R. R. Schaller, IEEE Spectrum **34**, 52 (1997).

12. I. Zutic, J. Fabian and S. Das Sarma, Rev. Mod. Phys. **76**, 323 (2004).

13. D. Xiao, G. B. Liu, W. Feng, X. Xu and W. Yao, Phys. Rev. Lett. **108**, 196802 (2012).

14. H. Min, J. E. Hill, N. A. Sinitsyn, B. R. Sahu, Leonard Kleinman, and A. H. MacDonald, Phys. Rev. B. **74**, 165310 (2006).

15. D. D. Awschalom and M. E. Flatte, Nat. Phys. **3**, 153-159 (2007).

16. S. D. Ganichev, E. L. Ivchenko, S. N. Danilov, J. Eroms, W. Wegscheider, D. Weiss and W. Prettl, Phys. Rev. Lett. **86**, 4358 (2001).

17. H. Ohno, H. Munekata, T. Penney, S. von Molnar, and L. L. Chang, Phys. Rev. Lett. **68**, 2664 (1992).

18. D. A. Vasyukov, A. S. Plaut, M. Henini, L. N. Pfeiffer, K. W. West, C. A. Nicoll, I. Farrer and D. A. Ritchie, Phys. Rev. B **91**, 201406(R) (2015).

19. Y. K. Kato, R. C. Myers, A. C. Gossard, and D. D. Awschalom, Science **306**, 1910 (2004).

20. J. Lee, K. F. Mak and J. Shan, Nature Nanotechnol. **11**, 421 (2016).

21. K. Mak, K. Mcgill, J. Park and P. McEuen, Science **344**, 1489 (2014).

22. A. Allain, J. Kang, K. Banerjee and A. Kis, Nat. Mat **14**, 1195 (2015).

23. A. H. Castro Neto, F. Guinea, N. M. R. Peres, K. S. Novoselov and A. K. Geim, Rev. Mod. Phys. **81**, 109 (2009).

24. D.S.L. Abergel, V.Apalkov, J. Berashevich, K. Ziegler and T. Chakraborty, Advances in Physics **59**, 261 (2010).

25. M. I. Katnelson, *Graphene: Carbon in Two Dimensions*, [Cambridge University Press, New York, 2012].

26. M. A. Omar, *Elementary solid state physics* [Addison-Wesley, 1975].

27. N. W. Ashcroft and N. D. Mermin, *Solid State Physics*, [Cenage Learning, 2013].

28. P.R. Wallace, Phys. Rev. **71**, 622 (1947).

29. A. Bostwick, T. Ohta, Th. Seyller, K. Horn, and E. Rotenberg, Nature Physics **3**, 36 (2007).

30. J. W. Jiang, Front. Phys. **10** 106801 (2015).

31. N. Peres, J. Phys.: Condensed Matter **21**, 323201 (2009).

32. H. Zeng, J. Dai, W. Yao, D. Xiao and X. Cui, Nature Nano. **7**, 490 (2012).

33. A. Kuc, N. Zibouche and T. Heine, Phys. Rev. B êxtbf83 245213 (2011).

34. Q. H. Wang, K. Kalantar-Zadeh, A. Kis, J. N. Coleman and M. S. Strano, Nature Nanotechnol. **7**, 699 (2012).

35. K. Mak. C. Lee, J. Hone, J. Shan and T. Heinz, Phys. Rev. Let. **105**, 136805 (2010).

36. G. Spavieri and M. Masuripur, Phys. Scr. **90** 085501 (2015).

37. G. Dresselhaus, Phys. Rev. **100**, 580 (1955).

38. E. I. Rashba, Physica E **34**, 31 (2006).

39. E. H. Hall, Am. J. Math. **2**, 287 (1879).

40. M. I. Dyakonov and V. I. Perel, Phys. Lett. A **35**, 459 (1971).

41. E. H. Hall, Phil. Mag. J. **10**, 301 (1880).

42. Y. K. Kato, R. C. Myers, A. C. Gossard and D. D. Awschalom, Science **306**, 1910 (2004).

43. J. Sinova, D. Culcer, Q. Niu, N. A. Sinitsyn, T. Jungwirth and A. H. MacDonald, Phys. Rev. Lett. **92** 126603 (2004).

44. W. Shan, H. Z. Lu and D. Xiao, Phys. Rev. B**88**, 125301 (2013).

45. J. P. Echeverry, B. Urbaszek, T. Amand, X. Marie and I. C. Gerber Phys. Rev. B. **93**, 121107 (2016).

46. E. Poem, Y. Kodriano, C. Tradonsky, N. H. Lindner, B. D. Gerardot, P. M. Petroff and D. Gershoni, Nature Phys. **6**, 993 (2010).

47. M. Baranowski, A. Surrente, D. K. Maude, M. Ballottin, A. A. Mitioglu, P. C. M. Christianen, Y. C. Kung, D. Dumcence, A. Kis and P. Plochoka, 2D Mater. **4**, 025016 (2017).

48. R. Roldan, J. A. Silva-Guillén, M. P. López-Sancho, F. Guinea, E. Cappelluti and P. Ordejón, Ann. Phys. textbf526, 347 (2014).

49. H. Zeng, G. B Liu, J. Dai, Y. Yan, B. Zhu, R. He, L. Xie, S. Xu, X. Chen, W. Yao and X. Cui, Sci. Rep. **3**, 1608 (2013).

50. B. Chen, H. Sahin, A. Suslu, L. Ding, M. I. Bertoni, F. M. Peeters and S. Tongay, ACS Nano **9**, 5326 (2015).

51. W. Liu, J. Kang, D. Sarkar, Y. Khatami, D Jena and K. Banerjee, Nano. Lett. **13**, 1983 (2013).

52. K. Byun, H. Chung, J. Lee, H. Yang, H. J. Song, J. Heo, D. H. Seo, S. Park, S. W. Hwang, I. Yoo and K. Kim, Nano. Lett. **13**, 4001 (2013).

53. H. Fang, S. Chuang, T. C. Chang, K. Takai, T. Takasashi and A. Javey, Nano Lett. **12**, 3788 (2012).

54. J. Kang, W. Liu, D. Sarkar, D. Jena and K. Banerjee, Phys. Rev. X, **4**, 031005 (2014).

55. K. Kim, S. Larentis, B. Fallahazad, K. Lee, J. Xue, D. C. Dillen, C. M. Corbet and E. Tutuc, ACS Nano **4**, 4527 (2015).

56. H. Chuang, X. Tan, N. J. Ghimire, M. M. Perera, B. Chamlagain, M. M. Cheng, J. Yan, D. Mandrus, D. Tomanék and Z. Zhou, Nano. Lett. **14**, 3594 (2014).

57. L. Ju, J. Velasco Jr, E. Huang, S. Kahn, C. Nosiglia, Hsin-Zon Tsai, W. Yang, T. Taniguchi, K. Watanabe, Y. Zhang, G. Zhang, M. Crommie, A. Zettl and F. Wang, Nat. Nano. **9**, 348 (2014).

58. Y. Sata, R. Moriya, S. Masubuchi, T. Taniguchi and T. Machida, Jpn. J. of Appl. Phys. **56**, 04CK09 (2017).

59. P. G. Gucciardi, S. Trusso, C. Vasi, S. Patanè, M. Allegrini 2007 *Near-Field Raman Spectroscopy and Imaging*. in: "Applied Scanning Probe Methods V: NanoScience and Technology". [Eds: B. Bhushan, S. Kawata and H. Fuchs, Springer, 2007].

60. A. C. Ferrari, J. C. Mayer, V. Scardaci, C. Casiraghi, M. Lazzeri, F. Mauri, S. Piscanec, D. Jiang, K. S. Novoselov, S. Roth and A. K. Geim, Phys. Rev. Lett **97**, 187401 (2006).

61. L. Malard, M. Pimenta, G. Dresselhaus and M. S. Dresselhaus, Physics Reports **473**, 51 (2009).

62. R. Beams, L. G. Cancado and L. Novotny J. Phys.: Condens. Matter **27**, 083002 (2015).

63. H. Li, Q. Zhang, C. C. R. Yap, B. K. Tay, T. H. T. Edwin, A. Olivier and D. Baillargeat, Adv. Funct. Mater. **22**, 1385 (2012).

64. N. Scheuschner, O. Ochedowski, M. Schleberger and J. Maultzsch, Phys. Status. Solidi B **249**, 12 2644 (2012).

65. C. Lee, H. Yan, L. E. Brus, T. F. Heinz, J. Hone, and S. Ryu, ACS Nano **4**, 2695 (2010).

66. W. Zhao, Z. Ghorannevis, K. K. Amara, J. R. Pang, M. Toh, X. Zhang, C. Kloc, P. H. Tan and G. Eda, Nanoscale **5**, 9677 (2013).

67. W. Zhao, Z. Ghorannevis, L. Chu, M. Toh, C. Kloc, P. H. Tan and G. Eda, ACS Nano. **7** 791 (2013).

68. M. Huang, H. Yan, C. Chen, D. Song, T. F. Heinz and J. Hone, PNAS **106**, 7304 (2009).

69. D. Yoon, Y. W. Son and H. Cheong, Nano. Lett. **11**, 3227 (2011).

70. P. Blake, E. W. Hill, A. H. Castro Neto, K. S. Novoselov, D. Jiang, R. Yang, T. J. Booth and A. K. Geim, Appl. Phys. Lett. **91**, 063124 (2007).

71. Z. H. Ni, H. M. Wang, J. Kasim, H. M. Fan, T. Yu, Y. H. Wu, Y. P. Feng and Z. X. Shen, Nano. Lett. **7**, 2758 (2007).

72. M. M . Benameur, B. Radisavlgevic, J. S. Héron, S. Sahoo, H. Berger and A. Kis, Nano. Tech. **22**, (2011).

73. H. Li, J. Wu, X. Huang, G. Lu, J. Yang, X. Lu, Q. Xiong and H. Zhang, ACS **7**, 10344 (2013).

74. S. Tongay, J. Suh, C. Ataca, W. Fan, A. Luce, J. S. Kang, J. Liu, C. Ko, R. Raghunathanan, J. Zhou, F. Ogletree, J. Li, J. C. Grossman and J. Wu, Sci. Rep. **3**, 2657 (2013).

75. C. S. Wu, Y. Makuichi and C. D. Chen, "High-Energy Electron Beam Lithography for Nanoscale Fabrication" in "Lithography" [Ed. M. Wang, InTech, 2010].

76. A. Castellanos-Gomez, M. Buscema, R. Molenaar, V. Singh, L. Janssen, H. S J van der Zant and G. A. Steele, 2D Mater. **1**, 011002 (2014).

77. G. Kioseoglou, A. T. Hanbicki, A. L. Friedman, D. Gunlycke and B. T. Jonker, Appl. Phys. Lett. **101** 221907 (2012).

78. H. Zeng, B. Zhu, K. Liu, J. Fan, X. Cui and Q.M. Zhang, Phys. Rev. B **86**, 241301(R) (2012).

79. A. Steinhoff, J. H. Kim, F. Jahnke, M. Rosner, D. S. Kim, C. Lee, G. H. Hans, M. S. Jeong, T. O. Wehlin and C. Gies, Nano. Lett. **15** 6841 (2015)

80. M. Yamamoto, S. Dutta, S. Aikawa, S. Nakaharai, K. Wakabayashi, M. S. Fuhrer, K. Ueno and K. Tsukagoshi, Nano. Lett. **15**, 2067 (2015).

81. H. Sahin, S. Tongay, S. Horzum, W. Fan, J. Zhou, J. Li, J. Wu and F. M. Peeters, Phys. Rev. B **87**, 165409 (2013).

82. K. Wang, T. Taniguichi, K. Watanabe and P. Kim (arXiv:1610.2929) (2016).